Doctoral Dissertation
博士論文

Observational characterization of protoplanetary disks, exo-rings, and Earth-twins in exoplanetary systems
(太陽系外惑星系における原始惑星系円盤、系外惑星リング、第二の地球の観測的特徴づけ)

A Dissertation Submitted for the Degree of Doctor of Philosophy
December 2019
令和元年 12 月 博士（理学）申請

Department of Physics, Graduate School of Science
The University of Tokyo
東京大学大学院理学系研究科物理学専攻

Masataka Aizawa
逢澤 正嵩

Abstract

Since the discovery of the first exoplanet around a Sun-like star in 1995, our understanding of planetary formation has drastically advanced, and, currently, there have been over 4000 discovered exoplanets. Most of the discovered planetary systems are significantly different from the planets in the Solar System implying the diversity of the extrasolar world as well as current observational limitations.

In this thesis, we attempt to tackle three specific themes related to the planetary formation and evolution; systematic search for exorings, observational quest for alignment among proto-planetary disks, and global mapping of an Earth analog.

In the first theme, we perform a systematic search for exoplanetary rings using the Kepler data. Signatures of transiting ringed planets are slightly different from ringless planets, and the difference between them can be exploited to search for planetary rings. Using a fast and precise algorithm for a transiting ringed planet, we search for exoplanetary rings among 168 Kepler planets, whose light curves possibly allow the detection of Saturn-like rings with the size of twice the planetary radius. We apply ringed and ringless models to phase folded light curves and compare the fitting outcomes to identify the signatures of rings. Firstly, we find 29 tentative systems, where fitting by ringed models is statistically favored compared with the ringless models. Although we examine these possible signatures in detail, we are not able to find convincing evidence of rings. In turn, we put constraints on possible planetary rings using the null results. Most of our targets have close-in orbits, so the planes of planetary rings are likely to be on the orbital planes of planets due to the tidal alignment. Based on this assumption, we conclude that the occurrence rate of rings larger than twice the planetary radius is less than 15 %. Although the majority of targets in this study are short-period planets, the null detection puts the quantitative constraint on origins, formation and evolution of planetary rings.

The second theme is to search for alignment among proto-planetary disks in nearby five star-forming regions using interferometric observations by ALMA. We analyze the directions of disks in five star-forming regions, and we find that the disk orientations projected in the sky are likely to be random in four regions out of five, which is consistent with a theory that angular momentum is generated by turbulent motions in molecular clouds. At the same time, we find the possible alignment in the Lupus III at the statistical significance of 2σ, and it might imply other mechanisms beyond turbulent motions for generating angular momentum. For the robust discussion in the Lupus region, we compare different observations and methods including sparse modeling for estimating disk's axes, and we find that all of them show consistent estimations of disk orientations. On the other hand, we find the alignment in Orion Nebula Cluster, but it turns out to be more likely a false positive, which is produced by systematic noises during an observation.

Finally, we present a new methodology for global mapping of an Earth analog in future direct imaging missions. In the study, we introduce new regularization terms of L1-norm and Total Squared Variation to recover the two dimensional map from scattered light curves of directly imaged planets. For quantifying the potential improvement by the new method, we compare the recovered maps with the ground truth map of the Earth by varying regularization parameters. Using both simulated and real data of scattered light of the Earth for 1 or 2 years, we find that particular sets of the regularization parameters in the new method give more correct 2d map than the conventional method. In addition, we also explore the feasibility of global mapping by considering limited observational duration and noise associated with directly imaging observations for an Earth analog at distance of 10 pc. We find that observations for only the first day of the month in 2 years can roughly recover the surface distribution of the Earth. Our study shows the importance of choices of regularization terms in global mapping, and demonstrates the feasibility of recovering the surface inhomogeneity of an Earth analog in future direct imaging missions such as HabEx and LUVOIR.

In this thesis, we present methods for characterizing exoplanetary counterparts of objects in the Solar System, Saturn and Earth analogs. We also explore the applicability of sparse modeling by exploiting interferometric data and light curves of directly imaged planets. These studies open new possibility of the sparse method in astronomy, and the further investigation is rewarding. In addition, we also attempt to provide unconventional ways to unveil the architecture of planetary systems; we present the potential methods for constraining planetary spins, and explore global alignment among proto-planetary disks beyond one particular planetary system. These works would contribute to understanding the origins and formation of planetary systems including the Solar System, and the methodologies presented in this thesis can be naturally applied to the current and future observations.

Contents

Chapter 1

Introduction

Since the first discovery of the exoplanet in 1995, a bunch of detection of exoplanets have been identified, and our understanding of planetary formation has been drastically improved. Having said so, the whole exoplanetary architectures are still unexplored due to the observational limitations of current technology, and the detection of Solar-System-like systems is still observationally challenging. Additionally, it is still difficult to characterize counterparts of detailed structures in the Solar Systems, which include rings, moons, comets, and life. Their detection is challenging but indispensable for building the inclusive planetary formation theory, which still largely depends on observational facts of the Solar System.

Since all of giant planets commonly possess planetary rings, we naturally expect them to exist in exoplanetary systems. Previously, Barnes & Fortney (2004) demonstrated that signatures of exoplanetary rings are detectable around exoplanets by the current instrument e.g. Kepler satellite, which has successfully discovered a lot of transiting planets. Later, Aizawa et al. (2017) presented a systematic search for rings around long-period Kepler planets and candidates, which potentially hold icy rings like Saturn, and they discovered one possible candidate of the ring. However, the majority of the Kepler planets have been still unexplored despite the capability of the Kepler satellite. Therefore, we further search for possible exoplanetary rings around the Kepler planets in Chapter 3.

Planet formation is the consequence of the star formation. Since molecular clouds have angular momentum, their collapse inevitable leads to formation of rotationally supported structures including proto-planetary disks, and they eventually evolve to planetary systems. Henceforth, the understanding of the star formation is also important for revealing the nature of the planet formation. One of the key concepts in the planetary formation is the angular momentum of planets, and their origin date back to the cores and molecular clouds at very early phases of star formation. Generally, the turbulent motion within clouds is recognized as the source of angular momentums (e.g. Goodman et al., 1993), and this hypothesis naturally predicts the random orientations of directions of angular momentums of cores, disks, and stars. There are a few attempts to find the alignment among stellar spins (e.g. Corsaro et al., 2017), and the further exploration of the alignment among stellar angular momentum is very encouraging.

Stellar spins can be significantly perturbed during the course of the stellar evolution, and their measurement is also technically challenging. On the other hand, the proto-planetary disks reside in the middle of star and planet formation, and they are likely to preserve the information on angular momentum transfer. Currently, there are several systematic campaigns for detecting planetary disks in nearby star-forming regions by the Atacama Large Millimeter/submillimeter Array (ALMA) (Ansdell et al., 2016; Barenfeld et al., 2016; Eisner et al., 2018; Cieza et al., 2019), so we can exploit their geometry to discuss the alignment. We explore this possibility in Chapter 4.

On the other hand, faced with the big data (e.g. ALMA, Kepler), the data analysis methods and their applications to the astronomy have been developed rapidly, and one of such techniques is the sparse modeling (e.g. Honma et al., 2014; Ikeda et al., 2016; Akiyama et al., 2017b,a; Kuramochi et al., 2018; Event Horizon Telescope Collaboration et al., 2019). This technique can be used to search for optimal solutions, and it is significantly useful especially when the possible solutions have a lot of zero values, i.e. sparsity. The practical example of this technique is an image reconstruction of a shadow of a black hole from interferometric observations in global networks (Event Horizon Telescope Collaboration et al., 2019).

Since the application of the sparse modeling in astronomy has just started, we investigate the possibility of the method further. Firstly, we exploit the technique to obtain the highly resolved images of proto-planetary disks to check whether it gives the precise estimations on the disk's axes. We find that the sparse modeling does not change the significance of the alignment as discussed in Chapter 4. To investigate the possibility of the sparse modeling further, we also apply the technique to inverse modeling of global mapping of an Earth analog in the future direct imaging observations. In this problem, the surface inhomogeneity of planetary surfaces is retrieved from their reflected light curves (Ford et al., 2001), and the reconstruction is generally ill-posed, so it would require the regularization terms (Kawahara & Fujii, 2011). Instead of adopting the conventional regularization, we introduce the sparse modeling for global mapping by exploiting the particular feature that the ocean has almost zero albedo. In this way, we demonstrate the potential of the sparse modeling for global mapping in Chapter 5.

Throughout the thesis, we also attempt to shed new light on the architecture of exoplanetary systems. In the Solar System, the Sun's rotation axis is well aligned with the planetary orbital axes, but this is not the case for exoplanetary systems, some of which show large misalignment between them. Such misalignment can be unique information on the dynamical evolution of the planetary systems, and it has been extensively studied. Complementary to the misalignment between stellar axes and planetary orbital axes, one can also exploit a obliquity of planetary spin and its correlation with other angles. Although the detection of the planetary spin is currently challenging, it can be measured through the characterization of planetary rings as presented in Chapter 3 and reflectional light in direct imaging in Chapter 5. Beyond the alignment within one particular system, global correlations among planetary systems would also give unique information on the overall picture of the stellar and planetary formation. Such correlations can be indirectly studied by investigating the disk-disk alignment, which has close a relation to the alignment among planetary systems, and it is discussed in Chapter 4.

This thesis addresses observational characterizations of stellar and planetary systems in unconventional approaches. We explore the possibility of the sparse modeling in Chapter 4 and Chapter 5 by considering interferometric observations of proto-planetary disks and direct imaging of exoplanets. We also give methodologies for identifying Solar-System counterparts, specifically exorings in Chapter 3 and exoplanetary surfaces in Chapter 5. Furthermore, the methodologies presented in this thesis are potentially useful for constraining planetary spins and global correlations among planetary systems, and they are complementary to previous studies in the context of discussion on the architecture of planetary systems.

The rest of this thesis is organized as follows. In Chapter 2, we summarize the current observational knowledge on exoplanetary systems, and give the foundation for the studies in this thesis. In Chapter 3, we present the intensive search for exoplanetary rings using the Kepler data, and give the constraint on ring formation in exoplanetary systems. In Chapter 4, we discuss the disk-disk alignment using interferometric observations by ALMA, and, in doing so, we also attempt to exploit the sparse modeling in measuring the disk's axes. In Chapter 5, we develop the new methodology to retrieve two dimensional surface map of Earth analogs, and discusses the feasibility of global mapping in the future direct imaging observations. Finally, in Chapter 6, we summarize the thesis and give the future prospects.

Chapter 2

Review on Observational Characterization of Exoplanetary Systems

Since the discovery of the first exoplanetary system, our understanding of planetary formation has been drastically changed. The majority of observed exoplanets are clearly different from the Solar System, implying that previous theories of planetary systems need to be revised. Indeed, there have been intensive studies to build up consistent scenarios for the planet formation. Beyond the mere detection, the characterization of planetary systems is a key for the further understanding of the planet formation: constraints on density, chemical compositions, and atmosphere of exoplanets. Furthermore, identifications of exoplanetary structures including rings, moons, and even planetary surface structures (e.g. land, ocean) are complementary to the detection of planets themselves, providing clues toward the consistent picture of the planet formation.

The exoplanetary systems are supposed to be formed out of molecular clouds, and understanding of the star formation processes in the clouds is very important for the planet formation as well. However, it is still challenging to connect the clouds to the planetary scales due to the complexity in physical processes involved gravity, fragmentation, rotation, magnetic fields, cooling or heating, radiation, and turbulent motion. One of the key concepts, which link the small- and the large-scale of star formation, is alignment among stellar angular momentum. Recent observations (e.g. Kepler, ALMA) allow the quantitative discussion of the alignment, so the further exploration is rewarding.

This chapter briefly reviews our current understanding of exoplanetary systems, and is organized as follows. Section 2.1 summarizes the current understanding of exoplanetary systems from observations. Section 2.2 discusses observational characterizations of moons, rings, and planetary surfaces in exoplanetary systems. Section 2.3 summarizes angular momentum evolution of stellar systems, and possible implications of stellar alignment for origins of stellar angular momentum. In the last section, we present the summary of this chapter.

2.1 Observed properties of Exoplanetary Systems

The first exoplanetary system was discovered in 1992 by pulsar-timing method, which indirectly identifies the planetary signatures via precise measurements of pulsar signals (Wolszczan & Frail, 1992). The host star in this system is a pulsar PSR B1257+12, and the discovery poses a question to the formation mechanism. Later, the first exoplanetary system around a main-sequence star, 51 Pegasi, was discovered by Mayor & Queloz (1995) via the radial velocity method, which probes the small wobble of stellar motions exploiting the Doppler shift. The planetary mass was estimated to be comparable to Jupiter mass, and its orbital period is 4.23 days. This Jupiter sized planet with the extremely short orbital period is dubbed as a “Hot Jupiter”, and it challenges the planetary formation theory, which assumed that giant planets form only far away form from the central star.

The subsequent observations have inflated the number of detected exoplanetary systems, and there have been the detection of over 4000 confirmed planets as of December in 2019 (http://www.exoplanet.eu/catalog/). Most of the planets have been detected via radial velocity and transit methods, which are complementary to each other. The former method probes the modified planetary mass $M_\mathrm{p}\sin i$, where M_p is the planetary mass, and i is the orbital inclination that is defined as the line-sight angle of the orbital axis. The latter transit method indirectly identifies planets using the dimming of a central due to a planet, and it presents a relative size of the planets to stars.

In addition to the transit and radial velocity methods, there are several different methods for detecting planets. Direct-imaging method is one of techniques for detecting the planetary light itself by suppressing the stellar light. Due to the nature of the technique, the method is potentially sensitive to distant planets compared with the other methods. The current technology (e.g. Gemini Planet Imager, Macintosh et al. (2014)) is still beyond the reach of cold planets in the Solar System because of the very low contrast of flux expected for such planets; 10^{-9} for Jupiter and 10^{-10} for Earth. Therefore, only young, massive and hot exoplanets have been detected by the method, and these planets give direct information on how planets formed at the first place.

Astrometry searches for a slight displacement of a stellar position, which is caused by an orbital motion of a planetary system. The method is sensitive to distant planets, which give large stellar displacements in the observations. However, the distant planets have long orbital periods, so it requires the large baseline for the observation. Currently, there are not so many planets detected by dastrometry, but the Gaia mission, which is observing the full sky for five years, is expected to yield tens of thousands planets in the future (Perryman et al., 2014).

Microlensing observations are also sensitive to distant planets. It exploits the planetary microlensing, which causes the brighting with the relatively short time-scale from hours to days. The sensitivity of microlensing is independent on planetary temperature, so it can yield the detection of cold planets typically around the snow lines. Suzuki et al. (2016) statistically analyzed the MOA-II microlensing survey for fix years, and they found that the function for mass-ratio q is not described by a single power law, but it has a break at $q \simeq 10^{-4}$, which corresponds to $20 M_\oplus$ for the median stellar mass of $0.6 M_\odot$ in the survey. The results show that the cold-Neptune like planets are possibly most common type of planets beyond the snowline. This technique is unique because it is sensitive to free-floating planets, which are unbounded to any stellar objects. The estimated frequency of Jupiter-sized free-floating or wide-orbit planets was estimated to be ~ 1 per one pre-main sequence star (Sumi et al., 2011), and later revised as ~ 0.25 (Mróz et al., 2017). Free-floating planets are considered to be formed by the ejection from planetary systems via dynamical scattering.

As a result of the numerous observations, we are gradually understanding the planetary architectures in a statistical manner. Figure 2.1 shows planetary orbital periods and planetary masses, and Figure 2.2 shows planetary radii. The blue points in the figures represent the Solar System, which is distant from majority of observed systems. This demonstrates the diversity in extrasolar worlds as well as the observational limitation of the current technology.

There are several distinct types of planets in the exoplanetary systems. One notable class is "Hot Jupiter" that has the Jupiter-sized radius or mass orbiting in a few to tens of days. The existence of Hot Jupiters directly requires the improvement in theories, because standard planet formation scenarios including core accretion and gravitational instability naturally expect the formation of cold planets. They are also dynamically important for the stability of planetary systems when they migrate from outer part of orbits. Currently, the origins of Hot Jupiters are still unknown. Possible scenarios include the in-situ formation, gas disks migration from outer orbit, high-eccentricity tidal migration with Lidov-Kozai mechanisms, and/or planet-planet scattering (Dawson & Johnson (2018) and references therein). These formation path can be tested by using the observational features, including eccentricity distribution, obliquity of planetary orbit, radius inflation, semi-major axis distribution, the relation between stellar age and planetary parameters, and planetary atmosphere. Each of evidence can be explained by at least one path, but the single origin cannot account for every observational evidence (Dawson & Johnson, 2018).

Another new class of planets is close-in "Super-Earth" or "Mini Neptune", which are slightly larger than the Earth and slightly smaller than the Neptune, respectively. The Kepler satellite revealed the large population of such planets, and Zhu et al. (2018) estimated that the one third of the main-sequence stars are considered to harbor planetary systems composed of 3 planets with $R_{\mathrm{p}} \geq R_{\oplus}$ and orbital periods $P > 400$ days. Their observed orbital periods are relatively short, and this indicates that the viable paths for the formation are associated with migrations (e.g. Cossou et al., 2014) or in-situ formation (e.g. Raymond & Cossou, 2014). In the in-situ formation, Super-Earths can be considered as failed Hot Jupiters without sufficient gas accretion, which is caused by the late formation of cores due to low density of disks (Lee et al., 2014). The density of Super-Earth are diverse from ~ 0.1 g/cc (Masuda, 2014) to 7.46 g/cc (Carter et al., 2012) and the very low dense Super Earths are generally called "super-puffs", which would be mainly composed of gas rather than rock. Their formation mechanisms are uncertain, but hot or warm super-puffs do not form in gas-rich environments in in-situ formation, so they might be migrated to the current positions from outer orbits with sufficient gas supply (e.g. Lee & Chiang, 2016).

On the other hand, "Warm Jupiter" resides in between hot and cold Jupiters, and their

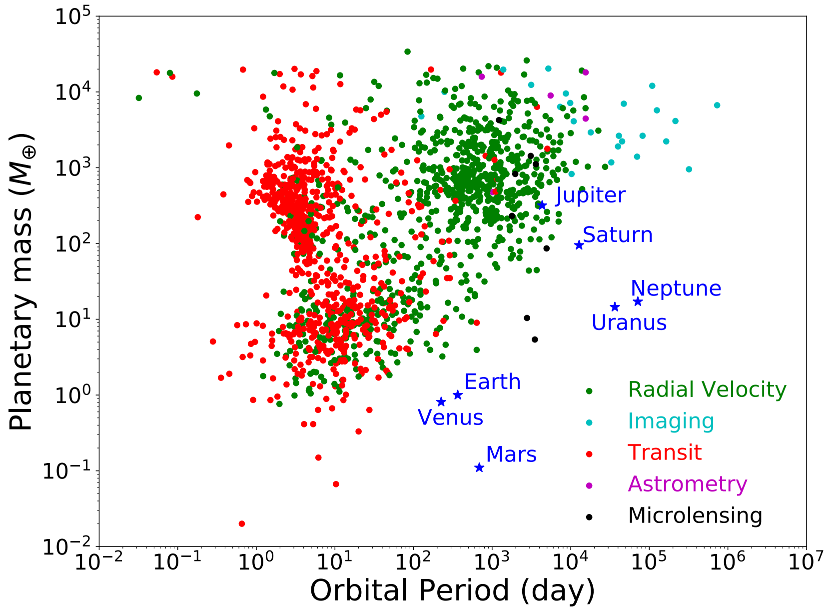

Figure 2.1 Orbital periods and planetary mass of exoplanets from the Extrasolar Planets Encyclopaedia (http://www.exoplanet.eu/catalog/). Colors express detection methods, and blue points correspond to planets in the Solar System.

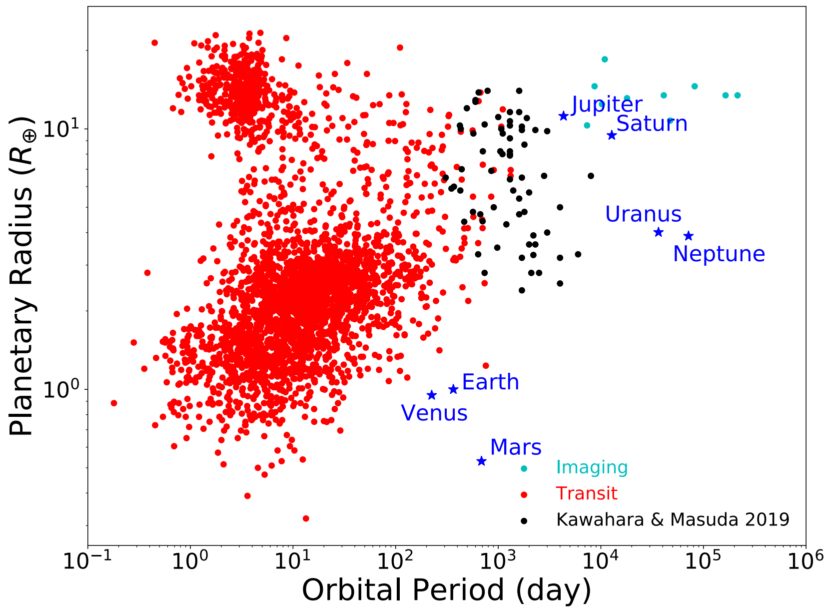

Figure 2.2 Orbital periods and planetary radii of exoplanets from the Extrasolar Planets Encyclopaedia (http://www.exoplanet.eu/catalog/). Black points are long-period transiting planets and their candidates detected by the Kepler (Kawahara & Masuda, 2019).

orbital periods are typically a few tens of days. They might be currently evolving from cold planets to close-in planets via some migration mechanisms, so their properties might be related to the connection between cold and hot Jupiters. However, their eccentricities are not so large to be largely migrated (e.g. Dawson et al., 2015), and their origin of has been still discussed (e.g. Dawson & Chiang, 2014).

Now, we turn to discuss exoplanets that resemble those in the Solar System. Basically, Solar-System analogs have small radii and/or long orbital periods, so their detection is observationally challenging even with the current technology. One exceptional class is "Cold Jupiter" with Jupiter radii and long orbital periods, most of which are probed by radial velocity surveys in decades (see Figure 2.1). The frequency of Jupiter-like planets is estimated to be 3%-10% (e.g. $6.2^{2.8}_{-1.6}$% for giant planets with $M_{\rm p} \sin i > M_{\rm J}$ and 3 au $< a <$ 10 au (Wittenmyer et al., 2016), implying that the the Solar System-like systems might not be common structure among planetary systems.

The transit method can be exploited for identifying the long-period planets beyond the snowline. The concept is that double or even single transits could be caused by planets with orbital periods comparable or beyond the observational duration, which is at most 4 years in the Kepler satellite. The findings of such planets with the Kepler data are made by the citizen scientist Wang et al. (2015), visual inspection (Uehara et al., 2016), and automated pipeline (Foreman-Mackey et al., 2016; Osborn et al., 2016; Schmitt et al., 2017)). Black dots in Figue 2.2 show the summary of possible long-period planets found by the Kepler satellite from Kawahara & Masuda (2019)

More distant giant planets like Saturn, Neptune, and Uranus are still difficult to detect because of their long periods ($\simeq$ 100 years), which are beyond the current observational duration for transit and radial velocity methods. On the other hand, the microlensing method is fairly sensitive to such distant planets. Gaudi et al. (2008) discovered a Jupiter+Saturn analog system around a $0.5 M_{\odot}$-mass star. the star. In addition, Sumi et al. (2016) also found the first possible candidate of a Neptune analog, which might orbit a low mass M-dwarf with the mass of $0.19 M_{\odot}$, albeit it could be min-Neptune or Super Earth around a brown dwarf.

Earth-like planets around Solar-type stars have also been technically challenging to detect and characterize. The transit method gives the tightest constraint on the occurrence rate, but as of today, there is no rocky planet with periods of $237 - 500$ days and planetary radii of $0.75 - 1.5 R_{\oplus}$ around FGK star in the Kepler sample (Hsu et al., 2019). This result sets the upper limit on the occurrence rate to be 0.27 at 1σ level. Among the planets, Kepler-452 is the most Earth-like planet around a solar type star (Jenkins et al., 2015), although its radius $1.5^{+0.32}_{-0.22} R_{\oplus}$ is still slightly larger than the Earth. Since their statistical signature is very weak, their detection could be false positive (Mullally et al., 2018).

Since the first discovery of exoplanetary systems, our knowledge and technology have been dramatically advanced. Although the current observations still allow the detection of planets with large radii and/or not too long orbital periods, the future ground and space missions (e.g. Gaia) will open a new window to the unexplored landscape, and finally, the occurrence rates of Solar System-like systems will be quantitatively evaluated.

2.2 Solar System analogs beyond planets: exomoons, exoplanetary rings, and exoplanetary surface

The detection of exoplanets is just the beginning of a long story for unveiling the histories of formation and evolution of planets. The next key step is observational characterizations of exoplanets, ranging from the basic orbital and physical parameters including orbital periods, radii, masses, and eccentricities to planetary compositions, atmosphere, habitability, magnetic fields, surface inhomogeneities, and even signatures of life. Another natural approach will be identifications of analogs of moons, planetary rings, continents, ocean. asteroids, comets, trans-Neptunian objects, Kuiper belts. They can be different from what we know in the Solar System, and they will tell us a new perspective of the planetary formation.

In this section, we discuss the detection of exomoons, exoplanetary rings, and surface inhomogeneities, all of which are main representatives of the planetary structures. For the latter two themes, we present methodologies to identify them in this thesis.

2.2.1 Exomoons

The detection of exomoons is still at the forefront of the current observations, and there is no solid confirmation of the systems. One of promising methods is the transit techinque, which probes the potential transits of exomoons and/or slight wobble of the planets through transit timing and duration variations (Kipping, 2009a,b). Kipping et al. (2012) initiated a serious search for exomoons using the Kepler data, and they finally obtained the statistical constraint and a hint for the single-moon populations (Teachey et al., 2018). Surprisingly, they also claimed the detection of the possible planet-moon system Kepler-1625 b. Their follow-up observations with the Hubble Space Telescope (HST) still favor the exomoon hypotheses, and the system is considered to be composed of Jupiter masse planet with ∼1 year orbit and the Neptune-sized exomoon (Teachey & Kipping, 2018). Although some groups cast doubt on the detection by pointing out the systematical errors in the analyses (Heller et al., 2019; Kreidberg et al., 2019), their claim is very encouraging for the further studies on this field.

The microlensing method is another approach to detect exomoons via detailed modeling of the light curvess. Bennett et al. (2014) discovered an event of microlensing that can be interpreted as motion of the Sub-Earth sized exomoon candidate orbiting around the planet with 4 Jupiter mass. The method allows the other solutions without the moons, but the future observations with WFIRST would be promising for the further studies.

Direct imaging technique is another possible path to find exomoons in the future, but their reflectional light is seriously contaminated by planetary light. Agol et al. (2015) proposed the methodology for detecting moon by exploiting positional displacements of the center of light called "spectroastrometry". The relative ratios of reflectional light of planets and moons depend on wavelength, so the difference can be used to estimate the orbital motions of the moon, the planetary mass, or even the separate spectrum of two bodies.

The detection of exomoons is still challenging, but attracting the interests at the same time. The transit and microlensing methods are already attempted to the searches, and the direct imaging technique is also promising in the future observations.

2.2.2 Exoplanetary rings

Since giant planets in the Solar System are commonly accompanied by planetary rings, we naturally expect that rings should also exist around exoplanets. However, due to the observational difficulty in detecting them, there has not been any confirmed candidate.

Saturnian rings, which are mainly composed of icy particles, have large optical depth implying the large amount of scattering, reflection, and blocking. One of approaches is the direct imaging of reflectional light from ringed planets. Arnold & Schneider (2004) and Dyudina et al. (2005) found that a ringed planet gives a significantly asymmetric phase curve with varying in amplitude several times during one period, and the phase curve of a ringed planet could be discriminated from that of a ringless planet. The current direct-imaging technique does not have sufficient sensitivity for that, but the future observation for the long duration is promising to find the solid evidence of the ring.

Although the direct imaging of a ring is not realistic in the current technology, the transit method is effective for the detection of a ring even with the current precision. Specifically, it was demonstrated that the Kepler satellite has the sensitivity to identify exoplanetary (Barnes & Fortney, 2004). Once the signatures are detected, the spectroscopic observation during the transit gives another complimentary evidence (Ohta et al., 2009). The serious search for exoplanetary rings using the Kepler data was rewarding but not conducted. In section 2.2.2.1, we summarize the formulation of the transit method for detecting a ringed planet, and, in section 2.2.2.2, we present the previous attempts to search for planetary rings.

2.2.2.1 Transit Photometry and Its Application to Ring Search

Transit is an astronomical event when a small celestial object blocks light from a larger body by passing between the observer and the source. During the transit, the stellar flux apparently decreases by blocking, and it could be the indirect evidence of a planet in exoplanetary sciences. The signatures of the transit depend on orbital configurations and sizes of both a planet and star.

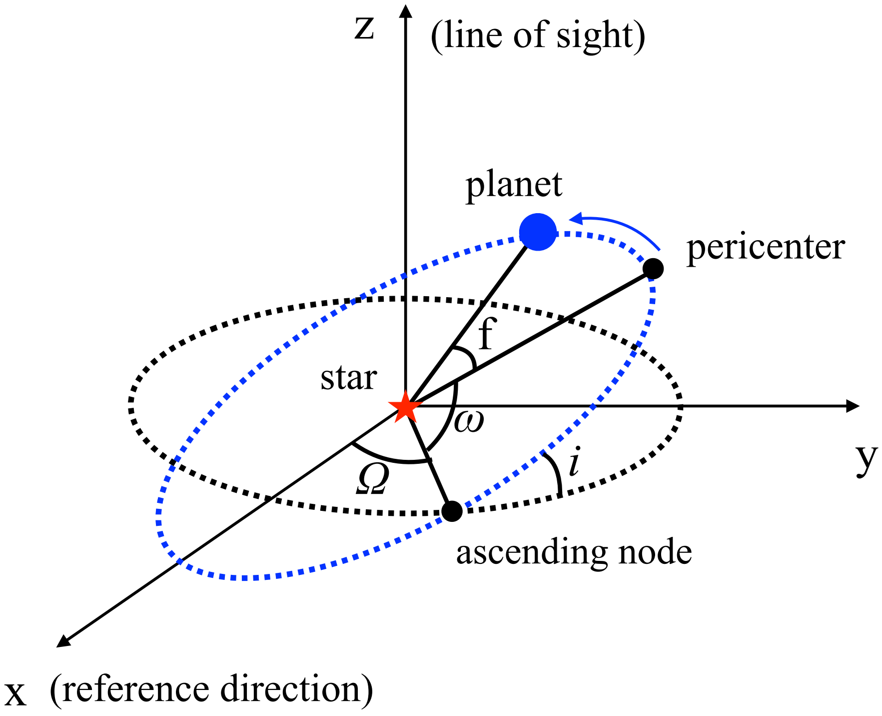

Figure 2.3 Orbital configuration of a planet and star, and their geometrical parameters. The z axis is taken to be the direction of a line of sight, and x and y axes are taken to be orthogonal to z axis.

Figure 2.3 depicts a planetary orbital configuration and geometrical parameters. Assuming the Keplerian motion, the relative position from a star to a planet is written as:

$$x = r(\cos\Omega\cos(\omega+f) - \sin\Omega\sin(\omega+f)\cos i), \tag{2.1}$$

$$y = r(\sin\Omega\cos(\omega+f) + \cos\Omega\sin(\omega+f)\cos i), \tag{2.2}$$

$$z = r\sin(\omega+f)\sin i, \tag{2.3}$$

where r is the distance from the planet to the star, Ω is the longitude of ascending node, i is the orbital inclination, ω is the argument of pericenter, and f is the true anomaly. Here, the true anomaly f describes the time evolution of the system, and it is determined by the orbital equations (e.g. the Kepler equation).

We take the z axis to be the line of sight, and the total relative flux can be rewritten as

$$F = 1 - \frac{\int I(x,y)D(x,y,t)dS}{I_{all}}, \tag{2.4}$$

where $I(x,y)$ is the stellar intensity map, and $D(x,y,t)$ describes the fraction of light that is blocked by the planet at (x,y,t). Assuming the limb-darkening law, $I(x,y)$ is described as

$$I(x,y) = I(r) = I_0(1 - 2q_2\sqrt{q_1}(1-\mu) - \sqrt{q_1}(1-2q_2)(1-\mu)^2), \tag{2.5}$$

where (q_1, q_2) are limb-darkening parameters with $0 < q_1 < 1, 0 < q_2 < 1$ (Kipping, 2013), I_0 is the intensity at the stellar center, and $\mu = \sqrt{1-(r/R_\star)^2}$ with the stellar radius $R_\star$. The calculation of Eq (2.4) requires the integration, which depends on the exact shape of the planet. We can consider a single planet, a ringed planet, or even a planet with an moon. The calculation itself can be done by pixel-by-pixel integration on the stellar surface, but the efficient and accurate algorithms have been proposed. As for the ringless planet, Mandel & Agol (2002) presented exact analytic expression for the eclipse of a star assuming the stellar intensity maps including quadratic limb darkening. On the other hand, there had been no proposed analytic method to calculate the integration in case of the ringed planet.

In general, rings are described by five parameters as summarized in Figure 2.4: inner radius of a ring $R_{\rm in}$, outer radius $R_{\rm out}$, the shading parameter T, and ring geometry (θ, ϕ). The shading parameter determines the form of $D(x,y,t)$ as:

$$D(x,y,t) = \begin{cases} 1 & \text{: if } (x,y) \text{ is within the planetary disk} \\ T & \text{: if } (x,y) \text{ is within the ring disk, but out of the planetary disk} \\ 0 & \text{: otherwise.} \end{cases} \tag{2.6}$$

Instead of using $(R_{\rm in}, R_{\rm out})$, we adopt dimensionless parameters for efficient fitting:

$$r_{\rm in/p} \equiv \frac{R_{\rm in}}{R_{\rm p}}, \qquad r_{\rm out/in} \equiv \frac{R_{\rm out}}{R_{\rm in}}. \tag{2.7}$$

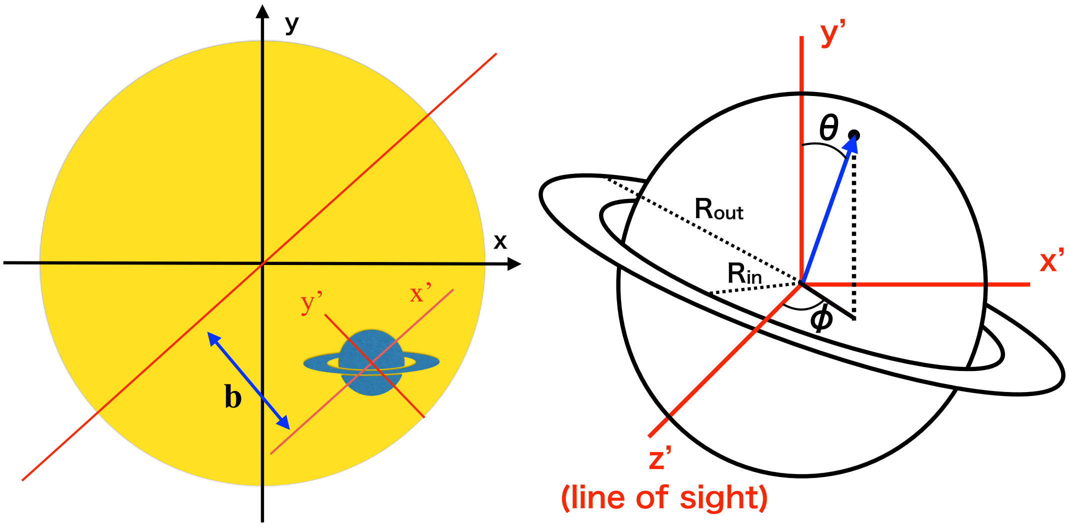

Figure 2.4 Schematic picture of transiting ringed planet. (a) Transiting ringed planet on a stellar disk. The x' axis is taken to be parallel to the transit chord, whose displacement from the stellar center is described by $b = a\cos i/R_\star$. (b) Geometrical parameters for ringed planet. (θ, ϕ) specify the direction of the ring axis, R_{in} shows the inner ring radius, and R_{out} shows the outer ring radius.

Aizawa et al. (2017) presented a formulation for the fast and accurate numerical integration of Eq (2.4) for a transiting ringed planet. They adopted a cylindrical coordinates (r, θ). Then, with r fixed, we can calculate intersections between a circle with radius of r and a ringed planet, and, on the circle, the value of $D(x, y, t)$ can change only at these boundaries.

$$\int I(x,y)D(x,y,t)dS = \sum_l D_l \int (\theta_{l+1}(r) - \theta_l(r)) I(\sqrt{1-(r/R_\star)^2}) r dr, \tag{2.8}$$

where $D(x, y, t)$ takes a constant value between $\theta_l(r) < \theta < \theta_{l+1}(r)$. The expressions for $\theta_l(r)$ are reduced to quartic equations, and there are at most 10 possible solutions for θ. The number of possible solutions depends on r, and the boundary values are also obtained by solving quartic equations. The specific derivations for $\theta_l(r)$ are given in Aizawa et al. (2017).

Using the above model, they tested the precision and computational time assuming a transit of Saturn-like plane with $R_{\text{p}}/R_\star = 0.083667$, $R_{\text{in/p}} = 1.5$, $R_{\text{out/p}} = 2.0$, $\theta = \pi/3$, $\phi = \pi/3$, $T = 1.0$. For orbital parameters and stellar parameters, they took $P = 10759.3$ days, $a/R_\star = 2049.89$, $b = 0.5$, $q_1 = 0.49$, and $q_2 = 0.34$. For comparison, they also considered the pixel-by-pixel integration around the planetary center (Ohta et al. 2009). They found that the current ring model at least gives the precision of 10^{-7}, and the computational speed is faster than the pixel integration when we require the precision beyond 10^{-5}. This comparison confirmed the robustness and speed of this computational scheme.

2.2.2.2 Previous Attempt to Search for Rings

Previously, there are several attempts to search for exoplanetary rings. Brown et al. (2001) for the first time set constraint on the ring size using the HST observation of a transiting planet HD209458, and they excluded the opaque ring with the radius of 1.8 times the planetary radius. Santos et al. (2015) also investigated the possibility that the presence of a ring account for the large reflectional light and rotational velocity of Peg 51 b, but the required configuration is inconsistent with the orbital stability. Therefore, they excluded the ring hypothesis for Peg 51 b. Lecavelier des Etangs et al. (2017) also tried to identify the ring around CoRoT-9b using the Spitzer photometry, and they did not find any signature of the ring.

In the meantime, a few searches for rings using the Kepler have been also conducted. Heising et al. (2015) searched for rings around 21 Kepler planets with 1 day $< P <$ 51 days, but they found no plausible candidate. On the other hand, Aizawa et al. (2017) attempted to identify exoplanetary rings among 89 long-period planets ($P >$ 200 days for most systems) with at most three transits in order to search for Saturn-like icy rings. They detected one possible candidate around KIC 10403228, whose light curve is consistent with single transit caused by a planet with a Saturnian sized ring. Due to the nature of the single event, the data are also consistent with a binary planet model and a circumstellar disk around a red giant star. After the publication of the paper, we inspected the parallax data presented by the gaia DR2, and find that the the host star is unlikely to be a giant star. As the orbital period is uncertain for this system, the further discrimination of the scenarios is challenging unless follow-up photometric observations including TESS give the additional transit.

Although Aizawa et al. (2017) explored cold planets, the majority of Kepler planets have not been still investigated. Saturnian rings are composed of icy particles, but it is not strange that the rocky rings are common around exoplanets. Therefore, the search for the exoplanetary rocky rings using the Kepler data is awaited, and we explore this possibility in Chapter 3.

2.2.3 Global Mapping of Earth Analogs

The surface of the Earth is diverse, and it is composed of land, ocean, clouds, vegetation, and snow. These features would also be common on exoplanets, and the identification of such surface information is rewarding to understand the exoplanetary environments. In addition, the surface information includes the vegetation, so it can be the evidence of a biosignature of the planet life. However, the characterization of the exoplanetary surfaces is not straightforward because it is basically impossible to directly resolve the planet. Given this difficulty, Ford et al. (2001) showed that the light curves scattered by a planet vary in intensity due to the apparent motions of surface inhomogeneities caused by planetary spins. By computing reflectional light curves in the multi-band observations, they showed that the light curves can be used to reconstruct the surface properties including land, ice, and even plant life. Based on this concept, the techniques of the inverse modeling have been developed by subsequent studies. In this section, we summarize the formulation of global mapping technique.

2.2.3.1 Forward Modeling of Reflectional Light from Exoplanet

We briefly describe the forward modeling of the global mapping following Fujii & Kawahara (2012). Figure 2.5 summarizes the geometric configuration and parameters. The scattering property of planetary surface depends on positions, and it is descried by the bidirectional reflectance distribution function (BRDF) $f(\theta_0, \theta_1, \varphi)$, where θ_0 is the incident zenith angle, θ_1 is the scattering zenith angle, and φ is the azimuthal angle between the direction of the incident and scattering light. Then, the scattering intensity at each pixel on the planetary surface is given by

$$\frac{dI}{d\omega} = F_\star R_\mathrm{p}^2 f(\theta_0, \theta_1, \varphi) \cos\theta_0 \cos\theta_1, \tag{2.9}$$

where $F_\star$ is the stellar flux, R_p is the planetary radius.

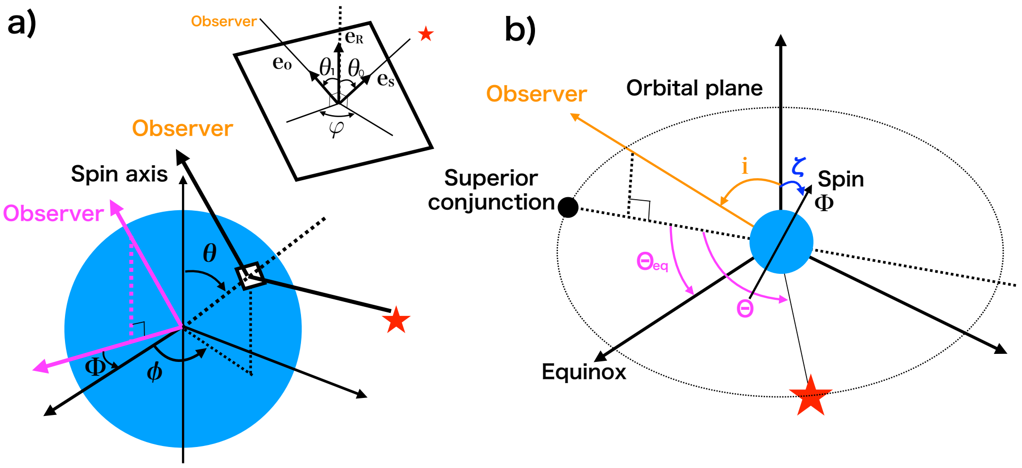

Figure 2.5 (a) Schematic picture of planetary reflection from a star to an observer. The planetary surface is described by (θ, ϕ), and the spin motion is descried by Φ. The close view of the surface is shown in the upper right. (b) Orbital configuration of planetary system with reflection. In the figure, ζ describes the planetary obliquity, Θ is the ecliptic longitude, and Θ_eq is the ecliptic longitude of the equinox.

The simplest expression for BRDF is the Lambertian reflection

$$f(\theta_0, \theta_1, \varphi) = \frac{m(\theta, \phi)}{\pi}, \tag{2.10}$$

where $m(\theta, \phi)$ is a surface albedo on (θ, ϕ). However, this is the approximation for the uniform reflection, and in reality, the functional form of $f(\theta_0, \theta_1, \varphi)$ depends on surface types (e.g. Fujii et al., 2010). The scattering for land is generally characterized by the

Rossi-Li model, which incorporates the isotropic scattering, the effect of thickness of the land, and the effect of the shadow (Eq (14) in Fujii et al. (2010)). The scattering for the ocean is descried by the characteristic BRDF function with the specular reflection when $\theta_0 = \theta_1$. The specular reflection could be exploited to directly discover the evidence of the ocean from light curves (Robinson et al., 2010).

The incident light is scattered by not only the surface but the planetary atmosphere (e.g. Fujii et al., 2010). In this case, the BRDF function is modified as

$$f(\theta_0, \theta_1, \varphi)_{\mathrm{atm},k} = f_{\mathrm{atm}}(\theta_0, \theta_1, \varphi) + C_{\mathrm{atm}}(\theta_0, \theta_1, \varphi) \times f_{\mathrm{surf},k}(\theta_0, \theta_1, \varphi), \tag{2.11}$$

where $f_{\mathrm{atm}}(\theta_0, \theta_1, \phi)$ describes the BRDF function for the atmosphere, and $C_{\mathrm{atm}}(\theta_0, \theta_1, \phi)$ describes the attenuation due to the atmosphere.

Assuming the Lambert reflection in Eq (2.10), the total reflectional light on the surface is given by

$$I = \int_s F_\star R_\mathrm{p}^2 f(\theta_0, \theta_1, \varphi) \cos\theta_0 \cos\theta_1 d\Omega, \tag{2.12}$$

$$= F_\star R_\mathrm{p}^2 \int_s \frac{m(\theta, \phi)}{\pi} \cos\theta_0 \cos\theta_1 d\Omega, \tag{2.13}$$

where (θ, ϕ) is the spherical coordinate system, s is the area that is visible both from an observer and a star. Total reflectance depends on wavelength, and Figure 2.6 shows the specific reflectance depending on surface types. Albedo of the land generally is large for the long wavelength. The albedo of the vegetation has the sharp rise around $\lambda = 0.7 \mu m$, and this called red edge (e.g. Robinson et al., 2010). The snow albedo is very close to 1, and the water albedo is close to zero.

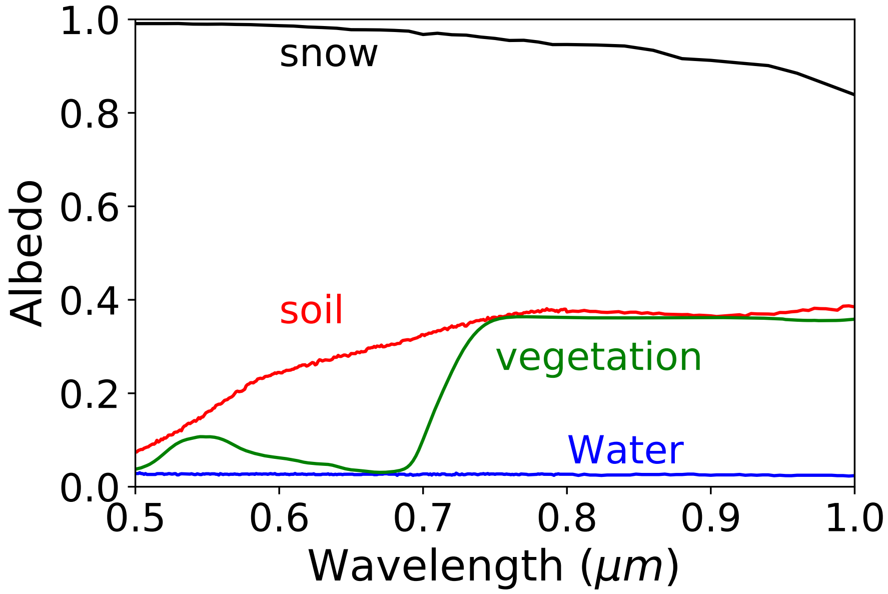

Figure 2.6 Effective albedo and its dependency on wavelength for various components taken from the ECOSTRESS spectral library (https://speclib.jpl.nasa.gov). We assume that snow is "Fine Snow", vegetation is "Uvularia sessifolia", water is "Tap Water", and soil is "Dark yellowish brown micaceous loam" in the library.

The integration in Eq (2.13) requires the expressions for geometrical positions including a planet and a star, and Figure 2.5 summarizes geometric parameters. The spin motion is specified by $\Phi(t) = \omega_{\rm spin} t + \Phi_{\rm offset}$, where $\omega_{\rm spin}$ is the angular velocity of the planetary spin and $\Phi_{\rm offset}$ is the constant offset for $\Phi(t)$. The ecliptic longitude is descried by Θ, whose origin is taken as the superior conjunction. The orbital inclination that is the angle between the line of sight and orbital axis is defined as i. Finally, the spin axis is specified by the obliquity ζ and the ecliptic longitude of the vernal equinox $\Theta_{\rm eq}$.

The ecliptic longitude Θ and the spin motion $\Phi(t)$ determine time evolution of the geometrical evolution among planet, star, and a observer. We define the unit vector from the planetary surface (θ, ϕ) to the host star as $e_{\rm S}$, the unit vector from the surface to the observer as $e_{\rm O}$, and the vector normal to the surface as $e_{\rm R}$. We introduce the coordinate system (x, y, z), where x axis is the direction of equinox, and the z axis is taken to the orbital axis. In addition, the y axis is taken to construct rectangular coordinate system. Then, the components of vectors $e_{\rm S}$, $e_{\rm O}$, and $e_{\rm R}$ are given as:

$$\begin{aligned}
e_{\rm S} &= (\cos(\Theta - \Theta_{\rm eq}), \sin(\Theta - \Theta_{\rm eq}), 0) \\
e_{\rm O} &= (\sin i \cos \Theta_{\rm eq}, -\sin i \sin \Theta_{\rm eq}, \cos i) \\
e_{\rm R} &= (\cos(\phi + \Phi) \sin\theta), \cos\zeta \sin(\theta + \Phi) \sin\theta + \sin\zeta \cos\theta, \\
&\quad - \sin\zeta \sin(\phi + \Phi) \sin\theta + \cos\zeta \cos\theta).
\end{aligned}$$

Using these expressions, we can compute $\cos\theta_0$ and $\cos\theta_1$ as well as I in the following manner:

$$I = \frac{F_\star R_\mathrm{p}^2}{\pi} \int m(\theta, \phi) W(\theta, \phi; \Theta, \Phi) d\Omega, \tag{2.14}$$

where we define the weight functions for the illuminated $W_I(\theta, \phi; \Theta, \Phi)$, visible area $W_V(\theta, \phi; \Phi)$, and their multiplication $W(\theta, \phi; \Theta, \Phi)$ as:

$$W_I(\theta, \phi; \Theta, \Phi) = \max\{e_S \cdot e_R, 0\}, \tag{2.15}$$

$$W_V(\theta, \phi; \Phi) = \max\{e_O \cdot e_R, 0\}, \tag{2.16}$$

$$W(\theta, \phi; \Theta, \Phi) = W_I(\theta, \phi; \Theta, \Phi) \times W_V(\theta, \phi; \Phi). \tag{2.17}$$

$$\tag{2.18}$$

2.2.3.2 Inverse modeling of mapping

The previous section deals with the forward modeling, and we can conversely exploit Eq (2.14) to estimate the planetary surface from the light curves. We adopt the linearized expression of Eq (2.14) using the discretized planetary surface with N_pixel pixels:

$$I = \frac{F_\star R_\mathrm{p}^2}{\pi} \sum_j^{N_\mathrm{pixel}} m(\theta_j, \phi_j) W(\theta_j, \phi_j; \Theta, \Phi) \Delta\omega_j, \tag{2.19}$$

where we assume the small pixels with the solid angle $\Delta\omega_j$. Then, by normalizing I, we obtain

$$d_i = \sum_j^{N_\mathrm{pixel}} G_{i,j} m(\theta_j, \phi_j) + \epsilon_i, \tag{2.20}$$

$$G_{i,j} = W(\theta_j, \phi_j; \Theta(t_i), \Phi(t_i)) \Delta\omega_j, \tag{2.21}$$

where d_i is the i-th normalized data, t_i is the time for i-th data, and ϵ_i is the observational error associated with d_i. Generally, the above problem is ill-posed, and there is no unique solution for a given d. To give the unique solution, Kawahara & Fujii (2011) introduced the Tikhonov regularization, which balances between the observational noise and the spatial resolution of the surface. The cost function for minimization is given by

$$Q_\lambda \equiv \sum_{i=1}^{N_\mathrm{data}} \frac{|d(t_i) - \sum_j^{N_\mathrm{pixel}} G_{i,j} m_j|^2}{\sigma_i^2} + \lambda^2 |m - \hat{m}|^2, \tag{2.22}$$

where σ_i is the standard deviation of the observational error for d_i, and $\hat{m} = \langle d \rangle$ is taken to be the mean of the data as a prior for the model. If the geometry is known, the minimization for Q_λ can be analytically solved:

$$m_{\mathrm{est},\lambda} = V \Sigma_\lambda U^T (\tilde{d} - \tilde{G}\hat{m}) + \hat{m}, \tag{2.23}$$

$$(\Sigma_\lambda)_{i,j} \equiv \frac{\kappa_i}{\kappa_i^2 + \lambda^2} \delta_{i,j}, \tag{2.24}$$

where we introduce $\tilde{d_i} \equiv d_i\sigma_i$, , $\tilde{G_{i,j}} = G_{i,j}/\sigma_i$, and Σ_λ is the diagonal matrix. The matrix G is decomposed as $G = U\Lambda V^T$, where U and V are orthogonal matrices, using the singular value decomposition. The i-th eigenvalue of G is κ_i, which is the i-th component of Σ. In order to determine the optimal λ, Kawahara & Fujii (2011) adopted L-curve criterion, which searches for λ with the maximum curvature point of the model norm $|m_{\mathrm{est},\lambda} - \hat{m}|$ versus residual $|d - Gm_{\mathrm{est},\lambda}|$ plot (Hansen, 2010). We note that the Tikhonov regularization does not build on physical foundation, so there still remain freedoms to choose the appropriate terms for the mapping.

When deriving the analytical solution in Eq (2.24), we implicitly assume the spin parameter $(\zeta, \Theta_{\mathrm{eq}})$, but they should be also estimated from the data as well. One can exploit Eq (2.22) to infer $(\zeta, \Theta_{\mathrm{eq}})$ by minimizing the cost function using some algorithms (e.g. Nelder-Mead method; Kawahara & Fujii (2011)). We can also directly read off the geometry from light curves by analyzing frequency modulations in the data, which are caused by the spin motions (Kawahara, 2016). The proposed method does not require the mapping method, so it is complementary to other methods that use the amplitude modulations.

The above formulations implicitly assume one band observation, but they can be naturally extended to multi-band observations in the real observation. Fujii et al. (2011) reconstructed the colored longitudinal map of the Earth using the real observation by assuming the specific surface types including oceans and soil.

In real observations, the clouds significantly contribute to the light variations, and the mitigation of their effect is one of important themes in this field. The effective albedo of clouds is basically flat in wavelength, so it can be mitigated by subtracting one color from another. On the other hand, the subtraction does no erase the reflection of the land, whose albedo varies in wavelength (see Figure 2.6). On the basis of this concept, Kawahara & Fujii (2011) employed the difference in the light curves between red and blue bands, and they successfully recovered the overall land distribution of the Earth from the light curve.

Beyond the simple subtraction, one can also adopt the principal component analysis (PCA), which is one of methods for reducing the dimensionality of the data by calculating orthogonal eigenvectors for sets of vectors. Assuming the n data of m elements X, the covariant matrix of the data is given by X^TX. The covariant matrix is symmetric matrix, so it can be diagonalized as $X^TX = U\Lambda U^T$, where Λ is a diagonal matrix, and U is an unitary matrix composed of eigenvectors u_k with m elements. The eigenvalues of Λ represent the variance of the eigenvectors, which describe the contribution of the k-th component u_k to the full variation of the light curves.

Cowan et al. (2009) firstly introduced PCA to extract the surface information from 2-days observations of the Earth in seven different bands in the EPOXI observation. They claimed that the derived eigencolors represent the relative color subtracted by the Earth mean color that is mostly explained by a cloud spectrum with atmospheric scattering. Among seven colors, the two strongest colors turns out to account for the 98 % variance of the data, and the first eigencolor is significantly sensitive to variations in longer wavelength corresponding to cloud-free continents. The second one corresponds to the shorter wavelength corresponding to cloud-free ocean. On the other hand, Fan et al. (2019) introduced the same technique to extract surface information using 2-years observations of the Earth. In this case, they found that the strongest component describe the variations caused by cloud reflection, and the second strongest one is closely correlated, specifically linearly, with the land fraction of the Earth the coefficient of determination r^2 is 0.91. The difference between the results of PCA and their interpretation would be ascribed to the difference in the observation duration.

PCA does not require the prior information on the surface types, so it can be applied to not only the Earth but also the exoplanets. However, PCA does not resolve the surface types (land, plant, snow), so the further improved methods, which enable the determinations of the surface types and distributions simultaneously, would be required to recover a "color" map of an exoplanet.

One possible improvement in the method is the appropriate adoption of the regularization term in Eq (2.22), because the Tikhonov regularization does not build on physical validity. In addition, previous studies assumed observational duration of a few years, but this will not be realistic to occupy satellites in a such long duration only for the global mapping. We explore these issues further in Chapter 5.

2.3 Angular Momentum Evolution in Star Formation and Emergent Constraint on Star Formation from Alignment

Exoplanetary systems are originally formed from molecular clouds, and the filling the gap between them is important to unveil the evolutional histories of exoplanets. Especially, proto-planetary disks can be considered to be the initial conditions of planet formation, so revealing their origins is crucially important for studying the subsequent evolution of exoplanetary systems (e.g. Simbulan et al., 2017).

One of key concepts in the star formation is the angular momentum evolution of stellar systems. Let us consider a cloud core with mass of M, radius of $R_{\rm init}$, and angular velocity of $\Omega_{\rm init}$. Then, the total angular momentum can be roughly approximated as $MR_{\rm init}^2\Omega_{\rm init}$. If this cloud core contracts to the object with the size of $R_{\rm end}$, the angular velocity is given by:

$$\Omega_{\rm end} = \frac{R_{\rm init}^2}{R_{\rm end}^2}\Omega_{\rm init}, \tag{2.25}$$

where we assume the angular momentum preservation. Let us adopt $\Omega_{\rm init} \simeq 10^{-6}$ yr^{-1} and $R_{\rm init} = 0.1$ pc for the cloud core (Goodman et al., 1993). Then, the stellar angular velocity is roughly 10^7 yr^{-1} if we adopt the sun radius of $R_{\rm end} = 2\times10^{-8}$ pc. This angular velocity is 3 orders of magnitude larger than the break-up angular velocity of the Sun, $\Omega_{\rm break} \simeq \sqrt{GM_\odot/R_\odot^3} \simeq 2\times10^4$ yr^{-1}, so this value is not allowed in the real situation, and this is called "angular momentum problem". If we equate the Kepler angular velocity with Eq (2.25), we find $R_{\rm end} \simeq 5000$ au implying that there should be the rotationally supported structures at this scale, and these correspond to stellar envelopes. This simple discussion demonstrates the requirement of the physical processes for extracting the initial angular momentums during the course of stellar evolution to finally make the star.

Figure 2.7 summarizes the evolution of the specific angular momentum from cloud to stellar scales. The rotations of the systems are basically probed by velocity gradients through the measurement of the Doppler shift of line emissions, mostly on the assumption of a solid rotation. Before going into the detail, we briefly comment on a few caveats in Figure 2.7. Firstly, the angular momentum is derived from the assumption that the velocity gradients trace the rotations of the systems, but this might not be true due to the complexity in kinematics including turbulent and infalling motions (e.g. Dib et al., 2010). Secondly, the figure only summarizes the specific angular momentum for independent objects rather than collecting the radial structure for particular systems, in other words, spatial dependence. In the similar manner, the figure only considers snapshots of the individual systems, so it does not correctly trace the evolution of the star formation from cloud to smaller scales. Having said so, the figure well describes the evolution of the angular momenta, and it is useful for grasping the overall picture of the evolution

The angular momentum evolution is mainly divided into three regimes. In the first regime with the length scale $\simeq 0.1$ pc, the specific angular momentum roughly follows $R^{1.5}$. Historically, Fleck & Clark (1981) compiled measurements of rotations for 12 clouds using molecular lines, and they found the relation $\Omega \propto R^{-2/3}$. For the smaller region, Goodman et al. (1993) also studied the rotations of 43 cores by measuring the velocity gradients, and found that the specific angular momenta are roughly scaled with $R^{1.5}$ consistently with Fleck & Clark (1981). These results were also confirmed by subsequent studies down to sub parsec scales (Caselli et al., 2002; Pirogov et al., 2003; Chen et al., 2007; Tobin et al., 2011; Tatematsu et al., 2016; Chen et al., 2019). Recently, Pineda et al. (2019) also studied the spatial distributions of specific angular momentum for cores, and they found that the relation $j_{\rm fit}(r) \propto r^{-1.80}$ from 800 to 10000 au. This might indicate the transition from the turbulent region $j \propto R^{1.5}$ to the solid rotation regime $j \propto R^{2.0}$ of the cores.

In the second regime beyond the scale of 0.1 pc for cores, the cores start to collapse gravitationally, and the specific angular momentum keeps constant until the rotationally supported structures are formed. Ohashi et al. (1997) compiled the interferometric observations of 7 young stars with rotationally supported disks and infalling envelopes in the Taurus molecular cloud, and compared the specific angular momenta with those of dense cores. They found that the specific angular momenta of envelopes are basically constant, $\simeq 10^{-3}$ km s^{-1} pc, consistently with the angular momentum preservation. In the third regime of proto-planetary disks, the specific angular momentum follows the Keplerian motion $\propto \sqrt{GMr}$, where G is the gravitational constant, M is the stellar mass. The specific angular momentum of proto-planetary disks are typically within the range of $\log_{10} j$ cm^{2}s^{-1} $= 19.4 \sim 20.9$ (Simon et al., 2000; Isella et al., 2009; Andrews et al., 2010; Williams & Cieza, 2011). Proto-planetary disks and envelope are accreted onto the protostars by losing their own angular momentums, and angular momentums transportation in proto-planetary disks would be driven by viscosity or other mechanisms (e.g, spiral density waves or disk winds) (e.g. Rafikov, 2017).

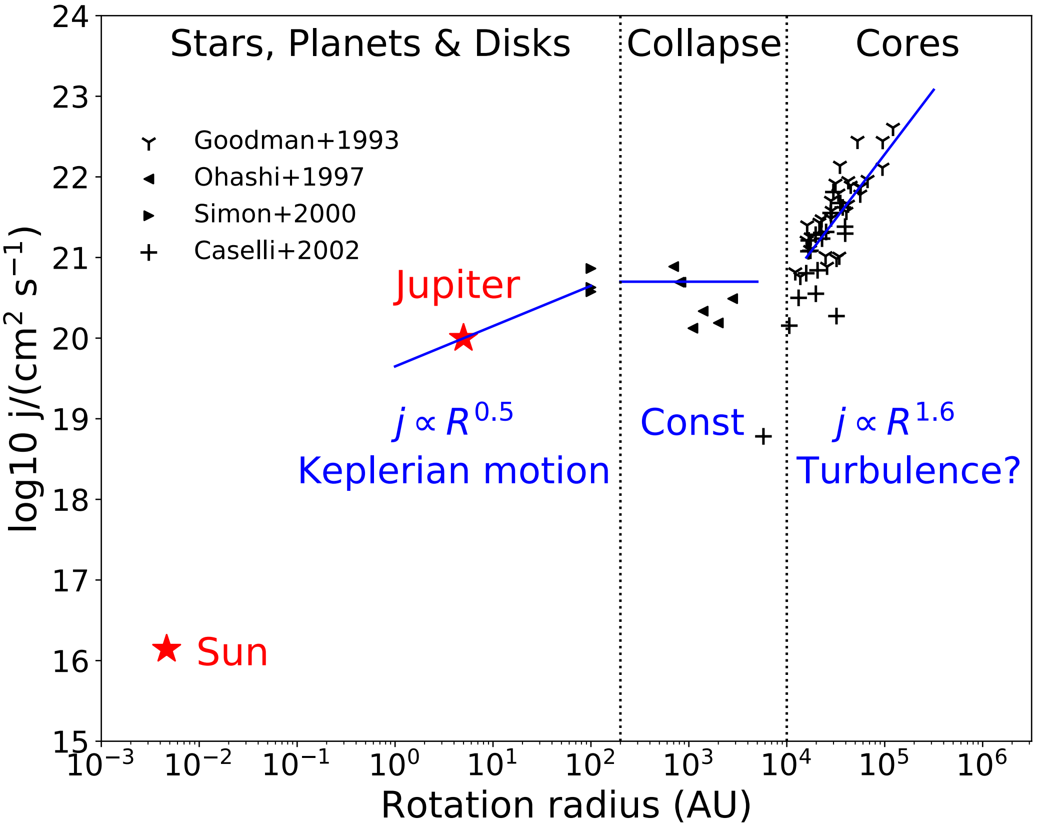

Figure 2.7 Specific angular momentum evolution in stellar systems from core scales to Sun (modified version of Figure 8 in Belloche (2013)). The values of specific angular momentum are taken from several literature (Goodman et al., 1993; Ohashi et al., 1997; Simon et al., 2000; Caselli et al., 2002). In the first regime, the specific angular momentum follows the relation $j \propto R^{1.5-1.6}$. In the second regime during the gravitational collapse, the angular momentum is preserved, and in the third regime, the rotation is described as the Keplerian motion $j \propto R^{0.5}$.

One of possible origins for the rotation is the velocity distribution, which follows the power law relation $\sigma_u(R) \sim R^{\beta}$ in molecular clouds (Larson, 1981). The values of β was estimated to be 0.38 in Larson (1981) and β of 0.5 in subsequent studies (e.g. Heyer & Brunt, 2004). The origin of $\sigma_u(R) \sim R^{\beta}$ is considered to be turbulent motions, which predict $\beta = 0.33$ in case of the Kolomogorov turbulence (Kolmogorov, 1941a,b). From the relation $\sigma_u(R) \sim R^{0.5}$, the dimension analysis of j predicts the relation $j \propto Rv \propto R^{1.5}$, and this is consistent with the empirical relation from measurement of core's rotations $j \propto R^{1.5-1.6}$ (e.g. Goodman et al., 1993) (also see Figure 2.7). Apart from the above dimensional analysis, the observed relation $j \propto R^{1.5}$ is also reproduced in 3d MHD simulations of core formation, which incorporate the turbulence as well as magnetic fields (e.g. Li et al., 2004; Chen & Ostriker, 2015, 2018). These facts support the hypothesis that the angular momentum is originated from or, furthermore, "generated" by the turbulent motions in molecular clouds.

There are also other possible paths for explaining the origins of angular momentum. Corsaro et al. (2017) presented three-dimensional hydrodynamical simulations of protocluster formation by changing the initial rotations of the molecular clouds. When the initial rotation is very large, they found that the directions of angular momentums are preferentially directed toward that of the injected rotation, suggesting that the angular momentum is originated from the global rotation of clouds. On the other hand, Kuznetsova et al. (2019) presented a suit of simulations of protocore formation in a collapsing molecular clouds with a global rotation in a similar manner to Corsaro et al. (2017), and they found that the direction of the initial global rotation does not affect those of angular momentums of resultant cores. They claimed that the angular momentums are generated mainly by the torques between dense parts in the gas rather than the global rotation, and this is consistent with their result that the enhancement in the density of gas particles increases the specific angular momentums as well.

In the above, we briefly overview the evolution of angular momentum and their origins, which are still uncertain even faced with large and diverse observations. The difficulty in revealing the star formation partly comes from the that the observations only give snapshot of specific systems at specific timings rather than the entire history of star formation. Simulations can resolve this problem partly, but they simultaneously bring new additional uncertainties including the initial conditions and the controlling parameters, and these make the robust comparison challenging. Therefore, any small piece of observational findings is precious to fully understand the picture of the star formation, which also advances our understanding of the planetary formation as well.

If the stellar angular momentum is originated from turbulent motions in molecular gas, the directions of rotations of stellar systems are expected to be randomly distributed. Conversely, if the orientations of stellar angular momentum are not random, the angular momentums are not simply generated by the random turbulent motion but by other physics or their combinations. For example, as studied in Corsaro et al. (2017), the global rotation of clouds possibly accounts for the angular momentum of each stellar component, and if so, the directions of rotations would be preferentially directed toward the initial rotation. In this way, the spatial correlations among stellar angular momentums can constrain the nature of the stellar rotations, which would be originally determined by the complex balance among turbulent motions, rotation, gravity, pressure, radiation, and magnetic fields.

The strong tool for investigating the relation is the distribution of stellar inclinations. The values can be obtained by exploiting the spectroscopic projected stellar rotational velocity $v_\star \sin i_\mathrm{s}$, the stellar rotation period P_rot, and the stellar radius $R_\star$. Using this concept, however, Jackson & Jeffries (2010) found no statistical trend of the alignment of stellar spins in Pleiades and Alpha Per clusters. Jackson et al. (2018) also reconfirmed that there is no strong evidence of the alignment among stars in Pleiades. On the other hand, Corsaro et al. (2017) measured the stellar inclination i_s of 48 red giants in two open clusters, and they claimed that both of fields show the evidence of the strong alignment. Furthermore, Kovacs (2018) reported the evidence for alignment of stellar spins in the open cluster, Praesepe.

Bimodality of the alignment or non-alignment possibly arises from the difference in the physical properties of parent clouds, but the apparent alginment might be caused by the systematics inherent in the methods for the analyses. Mosser et al. (2018) revisited the previous analyses of red giants including all stars in Corsaro et al. (2017), and they did not reproduce excess of low stellar inclinations in NGC 6819 and 6791 reported in Corsaro et al. (2017). They ascribed this discrepancy to the very narrow ranges of priors for the Bayesian analysis adopted in Corsaro et al. (2017), and the estimated values unexpectedly favors solutions with the low stellar inclinations leading to the apparent alignment. On the other hand, Kamiaka et al. (2018) suggested that the spectroscopic measurements of $v_\star \sin i_\mathrm{s}$ can be overestimated by macroturbulence typically being ignored in the analyses, and these systematics might account for the alignment with large stellar inclinations claimed in Kovacs (2018).

Although their finding and methodologies turned out to be unreliable or at least should be revisited (Mosser et al., 2018; Kamiaka et al., 2018), their results encouraged for the further studies to understand the origins of alignment. Corsaro et al. (2017) attributed it to the initial rotation of the parent clouds of open clusters. Specifically, using hydrodynamical simulations, they showed that if the more than half of the kinetic energy is rotational energy, the observational alignment is reproduced. In the similar manner, Rey-Raposo & Read (2018) simulated the hydrodynamical evolution of molecular clouds extracted from galactic simulations down to a scale of 0.1 pc, and they found the strong alignment among protocores in the clouds. These results show that the alignment among stellar spins might be related to the initial rotation of the clouds. In reality, however, the competition among the global rotation, turbulence and magnetic field in star-forming regions would be largely complex, and it is not trivial to connect the simulations to the observations.

One possible extension of search for alignment is search for alignment in difference scales. Proto-planetary disks reside in between stars and molecular clouds, so it might contain the direct information of the star formation rather than stars. In addition, observational properties of star-forming regions (e.g. magnetic fields, velocity fields, density) can be used to interpret the origins of possible alignment among disks in the regions. Fortunately, there are several intensive surveys for proto-planetary disks by ALMA, so we can exploit the observations to study the alignment further.

In summary, the alignment among stellar rotations give us a unique probe to connect the global molecular clouds to each stellar components. The alignment, if exists, is apparently inconsistent with the turbulent origins of angular momentum, and it poses a question to the current understanding of the angular momentum evolution, so the further investigation is rewarding. In Chapter 4, we attempt to search for alignment using proto-planetary disks.

2.4 Summary

In this section, we overview the current observational knowledge of the exoplanetary systems, most of which do not exist in the Solar System implying the diversity in extrasolar world as well as the observational limitations of the current instrument. These striking observational findings also enforce the modification of planetary formation, which previously did not care about the new types of planets (e.g. Hot Jupiter). Until now, there have been over detected 4000 exoplanets, and the next step would be the observational characterization of the systems via measurements of planetary density, populations, and atmospheres. In addition, search for analogs of rings, moons, and Earth in the exoplanetary systems would be indispensable for consistently explaining the planetary formation.

On the other hand, the planetary systems are originated from the molecular clouds, so correct understanding and knowledge of the star formation directly gives the foundations of planetary formation as well. One of the key concepts in physics is the angular momentum conservation, but this law apparently prohibits the formation of the stars unless we consider the significant extraction of the angular momentum. One possible origin of angular momentum is the turbulent motions, which predict the random orientations of the stellar rotations, and this hypothesis can be tested by investigating the spatial correlations among stellar angular momentum. Previous studies claimed the detection of alignment, but the significance is still controversial.

Any piece of observational evidence is vitally important to correctly understand the real physics to finally tackle the problem of unveiling the planetary formation from beginning to end. Given this in mind, we specifically focus on three specific topics on the observational characterization of the systems: the systematic search for exoplaneary rings using the Kepler light curves, formulating the methodology for global mapping of an Earth analog, and quest for alignment among disk orientations using the ALMA observation. These themes look independent and irrelevant to each other, but they will commonly contribute to an unified understanding of the planetary formation.

Chapter 3

Systematic Search for Rings around *Kepler* Planet Candidates: Constraints on Ring Size and Occurrence Rate

A bunch of exoplanets have been discovered, and one of the next steps will be the detection of an exoplanetary ring. Indeed, the photometric accuracy of the Kepler satellite potentially allows for the detection of rings around transiting planets, but there has been no report of the confirmed ringed planet in spite of several attempts (e.g. Barnes & Fortney, 2004; Ohta et al., 2009; Heising et al., 2015; Aizawa et al., 2017; Lecavelier des Etangs et al., 2017). The important lesson learned from early attempts, however, is the encouraging fact that the detection of rings around exo-planets, if any, is close to within reach even though not yet easy obviously. Therefore we decide to extend our previous search to all *Kepler* transiting planets with sufficiently high photometric accuracy in their short-cadence data.

More specifically, we select 168 *Kepler* planet candidates with high signal-to-noise ratios using the short-cadence data, so that we are able to probe tiny and short-duration characteristic signatures of rings. Because of those selection criteria, majority of our targets turned out to be short-period planets. Thus our survey is preferentially designed for rocky, instead of icy, rings in practice, but we can test the robustness of possible ring signatures at separate transit epochs. From this point of view, the present work is very complementary to our previous work (Aizawa et al., 2017), and regarded as a significant extension of Heising et al. (2015).

While we believe that some fraction of exoplanets should accompany rings, the required condition and the nature of those rings are largely unknown both theoretically and observationally. Even though we have not identified any candidate for a ringed planet in the analysis of the present chapter, we found several cases that mimic signature of rings, which are useful examples of false-positives for future ring searches. Also we are able to constrain the ring parameters from our null results for the targets. Our statistical and observational constraints would add insights into the origin and evolution of rings in a completely different environment than those in our Solar system. The approach of our current methodology will eventually answer the question to what extent our Solar system is a typical (or atypical) planetary system in the Galaxy, hopefully affirmatively.

The rest of the chapter is organized as follows. Section 3.1 describes our selection of target planets. Section 3.2 explains the data reduction and analyses of lightcurves with transiting ringless or ringed planets in detail. Section 3.3 presents the results and implications of our analysis. Finally, Section 3.4 concludes and discusses the future prospects for exoplanetary ring search.

3.1 Target selection

Since signatures of planetary rings are tiny, we have to carefully select target systems with sufficient signal-to-noise ratios for detailed analysis before performing a time-consuming individual analysis. We adopt the signal-to-noise ratio (S/N) of transiting systems as a measure of a rough potential detectability of their rings:

$$(S/N) = \sqrt{\frac{T_{\rm obs}}{P_{\rm orb}}}\frac{\delta_{\rm TD}}{\sigma_{\rm TD}}. \tag{3.1}$$

In the above equation, $T_{\rm obs}$ is the total duration of the observed lightcurve in the short-cadence data (1 month $\leq T_{\rm obs} \leq$ 4 years), $P_{\rm orb}$ and $\delta_{\rm TD}$ denote the the orbital period and transit depth, and finally $\sigma_{\rm TD}$ is the effective uncertainty of the data on the transit depth. To estimate $\sigma_{\rm TD}$, we interpolate or extrapolate the photometric uncertainty corresponding to the transit duration $\tau_{\rm TD}$ using values of the robust root-mean square (RMS) combined differential photometric precision (CDPP) in the *Kepler* Stellar Table.

In the present chapter, we focus on the *Kepler* short-cadence (1 min) data alone. The long-cadence data (29.4 mins) are not suitable for searching for signatures of rings, which are identifiable only for short timescales around the egress and ingress of the transit. We first retrieve parameters from the Q1–Q17 Data Release 25 catalog of all *Kepler* Objects of Interests (KOIs) (Thompson et al., 2018), and calculate (S/N) of those KOI planets that have short-cadence data. We exclude the systems whose dispositions are “FALSE POSITIVE” in the catalog.

The total duration $T_{\rm obs}$ corresponds to the observed duration of the system in the *Kepler* short-cadence data. Roughly speaking, $(S/N) = 1$ corresponds to the 1σ-detection of the transit of a planet, not of a planetary ring. Since a typical amplitude of the photometric anomaly due to a Saturnian ring is less than 1 percent of the planetary transit depth, we select all *Kepler* planet candidates with $(S/N) > 100$ as our targets.

Orbital periods and planetary radii of all 4029 KOIs with short-cadence data are shown in Figure 3.1. The majority of the KOI planets have insufficient (S/N) to detect possible rings, and 168 KOI planets satisfy $(S/N) > 100$ (plotted in red circles). We note that our targets include all systems in Heising et al. (2015) except for KOI-398.02 with $(S/N) = 97.1$ (20 out of 21).

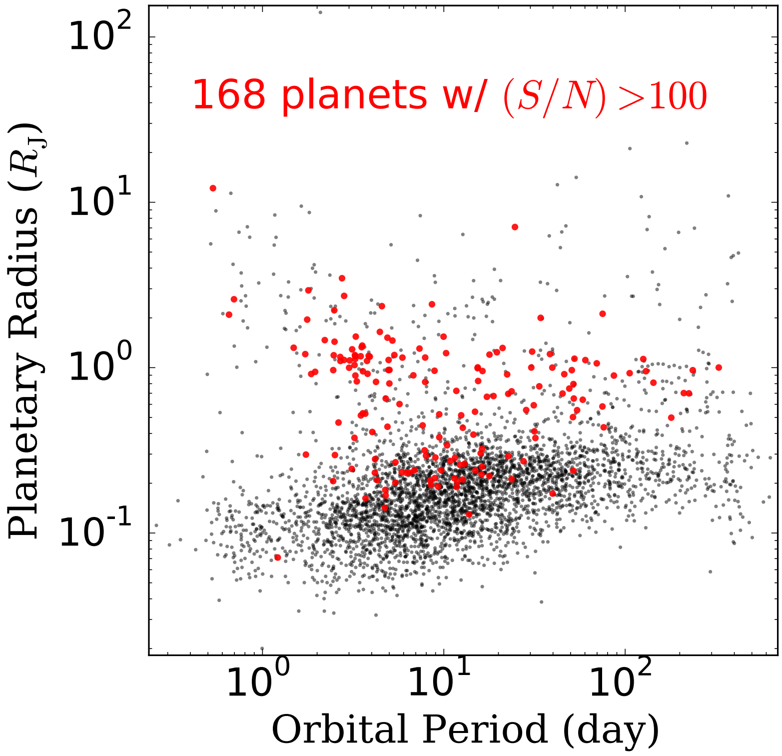

Figure 3.1 Planetary radii of 4029 KOIs against their orbital periods. Red points indicate the 168 targets with $(S/N) > 100$ that are examined closely in the present chapter.

3.2 Ring survey method: data reduction and fits of ringless and ringed planet models

This section describes our analysis method of ring survey, including lightcurve data reduction and fit to the parametrized templates of a planet with and without a planetary ring. The method is largely based on our previous paper Aizawa et al. (2017), and the brief description is summarized in Section 2.2.2.1. We adopt the stellar intensity profile with quadratic limb-darkening in Eq (2.5). Throughout the present analysis, we adopt the circular orbit of all the planets for simplicity, and we our ringless planet model is specified by seven parameters: the planet to star radius ratio $R_\mathrm{p}/R_\star$, the impact parameter b, the semi-major axis normalized by the stellar radius $a/R_\star$, the time of a transit center t_0, limb-darkening parameters q_1 and q_2, and the normalizing factor of the light curve c.

Our ring model is specified by additional five parameters; inner ring radius R_in, outer ring radius R_out, shading rate T, and orientation angles for ring axes θ and ϕ. If $T = 1$, a ring is fully opaque, and if $T = 0$, the ring is completely transparent. To increase the efficiency of numerical fitting, we employ $r_\mathrm{out/in} = R_\mathrm{out}/R_\mathrm{in}$ and $r_\mathrm{in/p} = R_\mathrm{in}/R_\mathrm{p}$, instead of R_out and R_in. Thus our ringed planet model is specified by 12 parameters in total. Further details of the model are found in Section 2.2.2.1 and Aizawa et al. (2017).

3.2.1 Making phase-folded lightcurves

If a transiting planet has a ring, the ring signature should be imprinted equally in each lightcurve at different transit epochs. Since, the ring parameters, in particular the orientation angles of the ring, are supposed not to vary for the timescale of T_obs, the signal-to-noise ratio of the signature should increase by stacking all the lightcurves properly. To produce such precise phase-folded lightcurves requires an accurate determination of both the transit center and baseline of each lightcurve at different transit epochs.

We use the short-cadence Pre-search Data Conditioned Simple Aperture Photometry (PDC-SAP) fluxes of the target objects from the Mikulski Archive for Space Telescopes (MAST). We adopt the transit model $F(t)$ implemented by the Pytransit package (Parviainen, 2015) for transiting ringless planets, which generates the lightcurve based on the model of Mandel & Agol (2002) with the quadratic limb darkening law.

We first apply the ringless model separately to each transit by varying the transit centers and baseline functions alone. Here, we take the fourth-order polynomials as the baseline functions, and we retrieve the transit duration and the other parameters of transiting planets from the MAST pipeline with the help of the Python interface *kplr* (http://dan.iel.fm/kplr/). We extract the lightcurve during the epoch of ±2 times the transit duration with respect to each transit center for the subsequent analysis.

After fitting, we exclude outliers exceeding 5σ amplitude in the flux so as to determine the baseline of the lightcurve accurately. We repeat the fitting procedure and removal of outliers until no outliers are left. Then we visually check each transit in order to exclude inappropriate transits that may be strongly affected by instrumental systematics.

Several transits exhibit large transit timing variations, which our pipeline cannot automatically deal with. In such cases, we appropriately choose the initial transit centers before fitting so as to correctly identify the transits. Finally, we obtain the best baseline using the out-of-transit (outside ±0.6× transit duration around the transit center) data alone, and normalize the lightcurve with the fitted baseline. Our fit to the transit model lightcurve is performed with the public code *mpfit* (Markwardt, 2009) that is based on the Levenberg-Marquardt (LM) algorithm.

We stack the obtained normalized lightcurve at each transit, and make the phase-folded lightcurve. We derive the transit duration by applying the ringless model to the phase-folded lightcurve. With the updated transit duration, we repeat the above procedure to obtain the final phase-folded lightcurve.

We extract the phase-fold lightcurve during an epoch within ±1 transit duration around the transit center. To finish the fitting procedures in realistic time, the lightcurve is divided into 500 bins with an equal time interval. Here, we require one bin to accommodate at least 10 points to guarantee the appropriate binning. So, for systems with the number of the phase-folded data less than 5000, we choose the bin width for one bin to have 10 data points.

Finally, we have phase-folded lightcurves for 168 planets, which are analyzed for ring search in the next subsection.

3.2.2 Separate fitting to planetary solutions with and without a ring

Our search for ring signatures is based on the comparison between the separate best solutions for a planet with and without a ring for all our targets.

In order to find the best solution in the 7 parameter space for a ringless planet model, we randomly generate 1000 different initial sets of parameters from the homogeneous distribution in a finite range. Then, we use the LM method to find the local minima starting from each of initial values, and we choose the best solution among the solutions. In fitting, we use the binned data that are produced in Section 3.2.1. We confirm that generally 100 initial sets of parameters are sufficient to find the minimum for our purpose.

Finally, we calculate the chi-squared value:

$$\chi^2_{\mathrm{ringless}} = \sum_{\mathrm{i}} ([d(t_{\mathrm{i}}) - m(t_{\mathrm{i}})]/\Delta d(t_{\mathrm{i}}))^2 \tag{3.2}$$

from the binned data. Here, $d(t_{\mathrm{i}})$, $m(t_{\mathrm{i}})$, and $\Delta d(t_{\mathrm{i}})$ are the observed flux, the expected flux of the model, and the uncertainty in observed flux at $t = t_{\mathrm{i}}$, respectively. We assume $\Delta d(t_{\mathrm{i}})$ to be a standard deviation of the normalized flux of each lightcurve estimated from its out-of-transit epoch.

The same procedure is performed for a ringed planet model. In this case, we have 12 free parameters t_0, b, R_{p}, $r_{\mathrm{out/in}}$, $r_{\mathrm{in/p}}$, θ, ϕ, T, $a/R_\star$, c, q_1 and q_2. We calculate the chi-squared value χ^2_{ring}, which has the definition similar to $\chi^2_{\mathrm{ringless}}$.

One fit of the ringed model takes about a few minutes in a lap-top, and the fits to the entire datasets were carried out with PC clusters in The Center for Computational Astrophysics (CfCA) in National Astronomical Observatory, Japan.

3.2.3 Searching for ring signatures via comparison between ringless and ringed planet models

Our next procedure is to create a list of tentative ringed-planet candidates from the comparison between the best-fit values for the two models, $\chi^2_{\text{ringless, min}}$ and $\chi^2_{\text{ring, min}}$. Specifically for this purpose, we adopt a F-test with F statics (e.g. Lissauer et al., 2011), and define

$$F_{\text{obs}} = \frac{(\chi^2_{\text{ringless, min}} - \chi^2_{\text{ring, min}})/(N_{\text{ring}} - N_{\text{ringless}})}{\chi^2_{\text{ring, min}}/(N_{\text{bin}} - N_{\text{ring}} - 1)}, \tag{3.3}$$

where N_{bin} is the number of in-transit bins of the phase-folded lightcurve (typically 500), and $N_{\text{ring}} = 12$ and $N_{\text{ringless}} = 7$ are the number of free parameters in the planetary models with and without a ring, respectively.

The numerator of the right-hand side of Eq. (3.3) corresponds to the improvement in χ^2 of the ring model divided by the number of the additional degrees of freedom characterizing a ring. The denominator is the χ^2 per degree of freedom for the ringed model. Thus, F_{obs} represents a measure of relative improvement of the fit by introducing the ring. The large F_{obs} prefers the ringed planet model. Note, however, that F_{obs} is defined simply through the ratio of the minimum values of χ^2 for the two models. Therefore it is nothing to do with the goodness of the fit for either model, which needs to be checked separately.

According to the F-test, the measure of the the null hypothesis that our ringed model does not improve the fit relative to the ringless model is given by the p-value defined as

$$p = 1 - \int_0^{F_{\text{obs}}} F(f|N_{\text{bin}} - N_{\text{ring}} - 1, N_{\text{ring}} - N_{\text{ringless}})\mathrm{d}f, \tag{3.4}$$

where $F(f|N_{\text{bin}} - N_{\text{ring}} - 1, N_{\text{ring}} - N_{\text{ringless}})$ is the F-distribution with the degrees of freedom $(N_{\text{bin}} - N_{\text{ring}} - 1, N_{\text{ring}} - N_{\text{ringless}})$.

The larger value of F_{obs}, therefore the smaller value of p disfavors the null assumption, i.e., the ringed model better fits the data than the ringless model. In this chapter, we adopt the condition of $p < 0.05$ for the rejection of the null hypothesis. For those tentative candidates of ringed planets, we attempt to understand the origins of anomalies by examining individual lightcurves and statistics (e.g. $\chi^2_{\text{ring, min}}$) further.

We also test the robustness of possible ring signatures by dividing the multiple transits into those at even and odd transit numbers, creating the phase-folded lightcurves separately, and computing the p-values $(p_{\text{even}}, p_{\text{odd}})$. Unlike the other analyses, we use the non-binned data here in order to evade the additional uncertainties in the lightcurves due to the extra binning step, especially for systems with the low number of the data. For the calculation of (p_{even}, p_{odd}), we approximate the best-fit model of the binned data as that of the non-binned data, and then we calculate F_{obs} in Eq (3.3) for non-binned data. If rings mainly account for signals in lightcurves, we expect $p_{\rm even}$ to be close to $p_{\rm odd}$ because of the consistency of the signals.

Finally, we comment on the validity of applying the F-test to our ring search. The F-test needs to satisfy two conditions (e.g. Protassov et al., 2002). One is that the two models are nested in a sense that the more complicated model reduces to the simpler one if the additional parameters in the former model are removed. This is trivially satisfied in the present case. The other condition is that the simpler model should not be located at the edge of the parameter space of the more complicated model. Strictly speaking, this condition may not hold because our ring model reduces to the ringless model in the limit of $R_{\rm out} \to R_{\rm p}$. Nevertheless, F-test gives us a practically useful criterion, and we decide to use it in selecting tentative candidates for further analysis.

3.2.4 Obtaining upper limits on the outer radius of a ring

Even for planetary systems without any detectable signatures of a ring, we may constrain the property of a possible ring within the observational detection limit. To proceed realistically, we need to reduce the number of free parameters charactering the ring. Thus we fix the inner radius of the ring as $R_{\rm in} = R_{\rm p}$, and set the opacity of the ring as $T = 1$ just for simplicity. Furthermore, we focus on two cases for the orientation angles of the ring as we describe in the next subsections. Thus we are left with a single parameter, the outer radius of the ring $R_{\rm out}$. In practice, we place upper limits on the ratio $R_{\rm out}/R_{\rm p}$ from the fit to the lightcurves.

3.2.4.1 Timescale for tidal alignment of planetary ring

The deviation of the lightcurve due to a ring relative to a ringless planet model prediction crucially depends on the size, opacity and orientions of the ring. In turn, a useful constraint on the size of the ring is placed only if the orientation of the ring is well specified. The ring axis is most likely aligned with the planetary spin axis. In the case of close-in planets as we mainly consider in the present chapter, the planetary spin axis is expected to be tidally aligned with that of the planetary orbit. Therefore the ring axis in such tidally aligned systems can be specified physically.

The damping timescale, which is comparable to the spin-orbit synchronization timescale, is given by

$$t_{\rm damp} \simeq \frac{2CQ_{\rm p}}{3k_{\rm p}} \left(\frac{M_{\rm p}}{M_\star}\right) \left(\frac{a}{R_{\rm p}}\right)^3 \left(\frac{P_{\rm orb}}{2\pi}\right), \tag{3.5}$$

(e.g. Schlichting & Chang, 2011). In the above equation, a is the semi-major axis of the planetary orbit, $R_{\rm p}$ is the planetary radius, $P_{\rm orb}$ is the planetary orbital period, $M_{\rm p}$ is the planetary mass, $M_\star$ is the stellar mass, C is the dimensionless moment of inertia of the planet (i.e., divided by $M_{\rm p}R_{\rm p,eq}^2$ with $R_{\rm p,eq}$ being the equatorial radius of the planet), $Q_{\rm p}$ is the tidal dissipation function of the planet, and $k_{\rm p}$ is the Love number.

We estimate $t_{\rm damp}$ for our target systems using the parameters from the Q1–Q17 Data Release 25 catalog of KOIs (Thompson et al., 2018), and list the values in Tables 3.1 to

3.3. In doing so, we adopt typical values of $Q_{\rm p} = 10^{6.5}$, $C = 0.25$, and $k_{\rm p} = 1.5$. The adopted value of $Q_{\rm p}$ is supposed to be typical for gas giants, but that for rocky planets would be substantially smaller. Thus the values listed in Tables 3.1 to 3.3 would be significantly over-estimated for rocky planets.

For the majority of systems, the planetary mass $M_{\rm p}$ is not directly measured. Thus we adopt Eq. (8) of Weiss et al. (2013), and rewrite it as

$$\frac{M_{\rm p}}{M_\oplus} = 0.337 \left(\frac{R_{\rm p}}{R_\oplus}\right)^{1/0.53} \left(\frac{F}{{\rm ergs^{-1}cm^{-2}}}\right)^{0.03/0.53}, \tag{3.6}$$

where $M_\oplus$ and $R_\oplus$ are the mass and radius of Earth, and F is the incident flux of the host star received at the location of the planet:

$$F = \frac{\sigma_{\rm SB} T_{\rm eff}^4 R_\star^2}{4\pi a^2}, \tag{3.7}$$

with $\sigma_{\rm SB}$ is the Stefan-Boltzmann constant. For example, if we consider the Hot Jupiter (a=0.05 AU) around the Sun, we obtain $F = 5.46 \times 10^8$ ${\rm ergs^{-1}cm^{-2}}$.

We compute $M_{\rm p}$ from $R_{\rm p}$ in the Kepler catalog for 155 systems. According to Eq. (3.6), the remaining 13 systems have $M_{\rm p} > M_{\rm J}$ and we set $M_{\rm p} = M_{\rm J}$ for such systems, since Eq. (8) of Weiss et al. (2013) cannot be applied for that range. Because we use the values of $M_{\rm p}$ only in computing their $t_{\rm damp}$, that simple estimate does not change our result.

3.2.4.2 Aligned with the planetary orbit

Under the strong tidal interaction with the star, the ring becomes aligned to the orbital plane of the planet. Indeed Brown et al. (2001) gave the upper limit on the ring size of a Hot Jupiter, HD 209458 b, as $1.7R_{\rm p}$ assuming the alignment.

In a similar manner, we place upper limits on the ring size assuming the tidal alignment. The tidal alignment leads to the orientation of $\theta = \arcsin(b/(a/R_\star))$ and $\phi = 0$. In addition, the small value of θ enhances the effective optical depth viewed from the observer, relative to that from the top-view. Thus, we assume $T = 1$ even though rings can be very thin like Jupiter's rings.

In summary, we fix $\phi = 0°$, $\theta = \arcsin(bR_\star/a)$, $T = 1$, and $R_{\rm in} = R_{\rm p}$ for fitting. Assuming these conditions, we fit the ringed model to the data using at least 100 sets of randomly chosen initial parameters, and we pick up the best solution among the local optimum solutions.

After obtaining the best solutions with fixed values of $R_{\rm out}/R_{\rm p}$, we define the 3σ limit $(R_{\rm out}/R_{\rm p})_{\rm upp}$ where

$$\Delta\chi^2(R_{\rm out}/R_{\rm p}) \equiv (\chi^2_{\rm ring,\ min}(R_{\rm out}/R_{\rm p}) - \chi^2_{\rm ringless,\ min})/(\chi^2_{\rm ringless,\ min}/{\rm dof}) \tag{3.8}$$

becomes 9. In practice, we compute $\Delta\chi^2(R_{\rm out}/R_{\rm p})$ at 11 values of $R_{\rm out}/R_{\rm p}$: 1.1, 1.3, 1.5, 2.0, 2.5, 3.0, 4.0, 5.0, 6.0, 8.0, and 10.0. Then we interpolate them to find $(R_{\rm out}/R_{\rm p})_{\rm upp}$.

Our procedure to setting the upper limit is illustrated in Figure 3.2 for KOI–97.01. In this example, the interpolated curve crosses the $\Delta\chi^2 = 9$ threshold at $R_{\rm out}/R_{\rm p} = 1.55$. Thus we obtain $(R_{\rm out}/R_{\rm p})_{\rm upp,\ Aligned} = 1.55$ for KOI–97.01. Figure 3.3 plots three corresponding fitting curves with $R_{\rm out}/R_{\rm p} = 1.5$, 2.0, and 2.5 along with the curve of the ringless model.

If $\Delta\chi^2 < 9$ for $R_{\rm out}/R_{\rm p} = 10.0$, we do not place upper limits $(R_{\rm out}/R_{\rm p})_{\rm upp}$. These cases are marked as $-$ in Tables 3.1 to 3.3 below.

The alignment condition is determined by the tidal dissipation function $Q_{\rm p}$ and the Love number $k_{\rm p}$, the planet/star mass ratio, the dimensional moment of the inertia of the planet C, the orbital period $P_{\rm orb}$, and the normalized semi-major axis $a/R_\star$. As discussed in Appendix A, 154 out of the 168 planetary systems are supposed to become aligned within a timescale of 1Gyr, if we adopt a fiducial values, $Q_{\rm p} = 10^{6.5}$, $k_{\rm p} = 1.5$, $C = 0.25$, and the mass-radius relation (Eq (8) in Weiss et al. (2013)). We compute the upper limit on $R_{\rm out}/R_{\rm p}$ for all 168 systems in any case even if their alignment timescale is long.

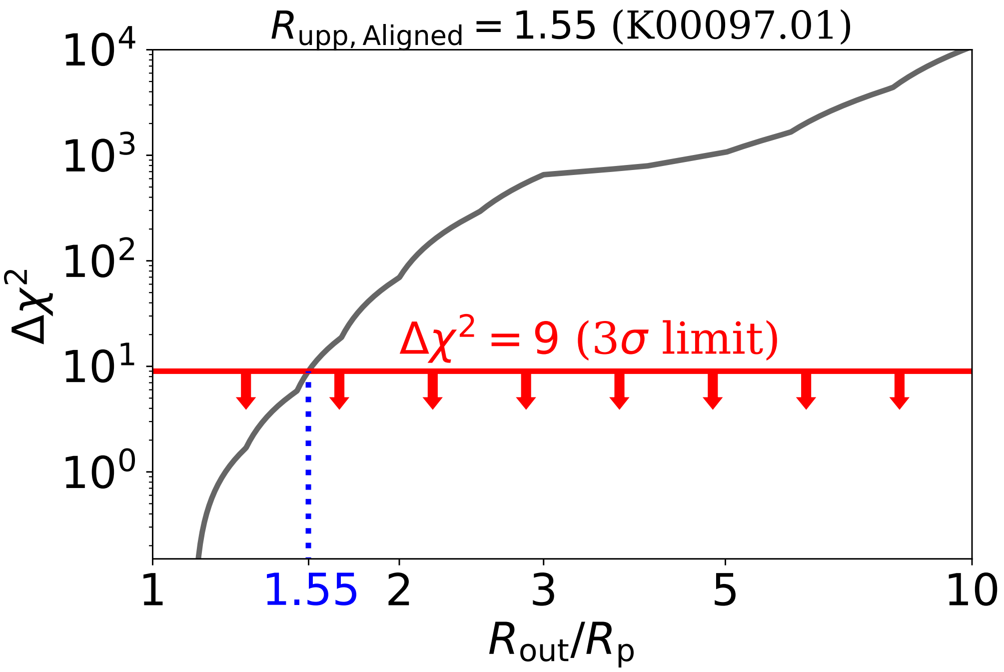

Figure 3.2 An example illustrating how to set an upper limit on $R_{\rm out}/R_{\rm p}$. Black curve shows $\Delta\chi^2$, eq.(6), of an aligned ring model for KOI-97.01. The value of $R_{\rm out}/R_{\rm p} = 1.55$ where $\Delta\chi^2 = 9$ is defined as our $(R_{\rm out}/R_{\rm p})_{\rm upp,\ Aligned}$.

3.2.4.3 Orientation of the Saturnian ring

As another model for the ring orientation, we simply adopt the Saturnian case $\phi = 0°$ and $\theta = 26.7°$, in addition to $T = 1$ and $R_{\rm in} = R_{\rm p}$ as before. Although the values of T and $R_{\rm in}$ are adopted just for simplicity, the derived upper limits are mainly sensitive to

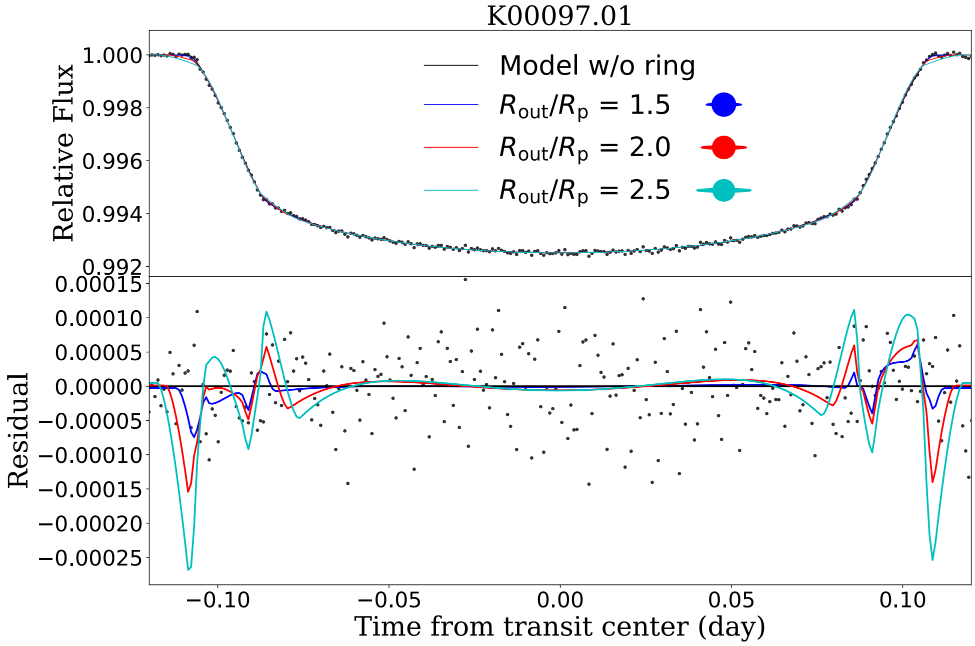

Figure 3.3 Lightcurves for KOI-97.01. Gray points are the binned data of KOI-97.01. Blue, red, and cyan curves correspond to the best-fits of the ringed model with $R_{\rm out}/R_{\rm p} =$ 1.5, 2.0, and 2.5, respectively. The lower panels indicate the residuals with respect to the best-fit of the ringless model.

$R_{\rm out}$, and can be scaled with the different values of T. An additional small signal due to an inner gap may be extracted if $R_{\rm in} > R_{\rm p}$, while it is not important in the present analysis (e.g Barnes & Fortney, 2004; Akinsanmi et al., 2018).

With fixed values of $R_{\rm out}/R_{\rm p}$, we search for the optimal solutions by varying other parameters in the similar manner as in Sec 3.2.4.2. In the analysis, we vary $R_{\rm out}/R_{\rm p}$ up to $1/\sin(26.7°) \simeq 2.22$, above which a shape of an assumed ring is not distinguishable from an oblate planet with the same oblateness. Practically, we use 8 fixed values of $R_{\rm out}/R_{\rm p}$: 1.1, 1.2, 1.3, 1.4, 1.6, 1.8, 2.0, and 2.22. Then, we obtain the 3σ limit $(R_{\rm out}/R_{\rm p})_{\rm upp,\,Saturn}$ by interpolating the values of $\{R_{\rm out}/R_{\rm p},\, \Delta\chi^2(R_{\rm out}/R_{\rm p})\}$. If $\Delta\chi^2 < 9$ for $R_{\rm out}/R_{\rm p} = 2.22$, we do not give the upper limits $(R_{\rm out}/R_{\rm p})_{\rm upp,\,Saturn}$.

In addition to the limits on $R_{\rm out}/R_{\rm p}$, we also place upper limits on the ratio of the outer radius of the ring and the stellar radius, $(R_{\rm out}/R_\star)_{\rm upp}$. Qualitatively this is simply given by $(R_{\rm out}/R_{\rm p})_{\rm upp} \times (R_{\rm p}/R_\star)_{\rm ringless}$, but not exactly because the best-fit planet radius may be different if the ring model is assumed instead. To evaluate $(R_{\rm out}/R_\star)_{\rm upp}$ correctly, we estimate $R_{\rm p}/R_\star$ corresponding to $(R_{\rm out}/R_{\rm p})_{\rm upp,\,Saturn}$ by interpolating the values of $\{R_{\rm p}/R_\star,\, (R_{\rm out}/R_{\rm p})_{\rm upp,\,Saturn}\}$. Then, we obtain $(R_{\rm out}/R_\star)_{\rm Saturn,upp} = (R_{\rm out}/R_{\rm p})_{\rm upp,\,Saturn} \times$ $(R_{\rm p}/R_\star)$ using the interpolated values. For simplicity, we only give $(R_{\rm out}/R_\star)_{\rm upp}$ for systems with $(R_{\rm out}/R_{\rm p})_{\rm upp,\,Saturn}$.

Incidentally the damping timescales of the 13 systems with $p < 0.001$ turned out to be significantly less than 1 Gyr except for KOI-868. Thus the possible rings for the 12 systems are likely to be aligned with the planetary orbital plane. Thus we do not compute

$(R_{\rm out}/R_{\rm p})_{\rm upp,\,Saturn}$ for all the systems with $p < 0.001$.

3.3 Result of the ring survey

3.3.1 No Convincing Candidate for a Ringed Planet

We have performed a ring search following the method described in Section 3.2. The result for all the 168 Kepler objects is summarized in Tables 3.1 to 3.3.

We identify 29 candidate objects with p-values less than the threshold value of 0.05. For most of these systems, the ring model yields $\chi^2_{\rm ring}/{\rm dof} \sim 1$ (Figure 3.4). However, after inspecting individual lightcurves of these systems, we conclude that none of them is a viable candidate for a ringed planet. The 11 of the 29 candidates do not exhibit any convincing ring-like signatures in the lightcurves, and so are excluded. The other 18 systems do show anomalous features in the lightcurves, but they are most likely ascribed to other mechanisms: gravity darkening (2 systems), spot-crossing (9 systems), disintegration of a planet (1 system), artifacts generated during the folding process (3 systems), and stellar activity (3 systems) as discussed in the following.

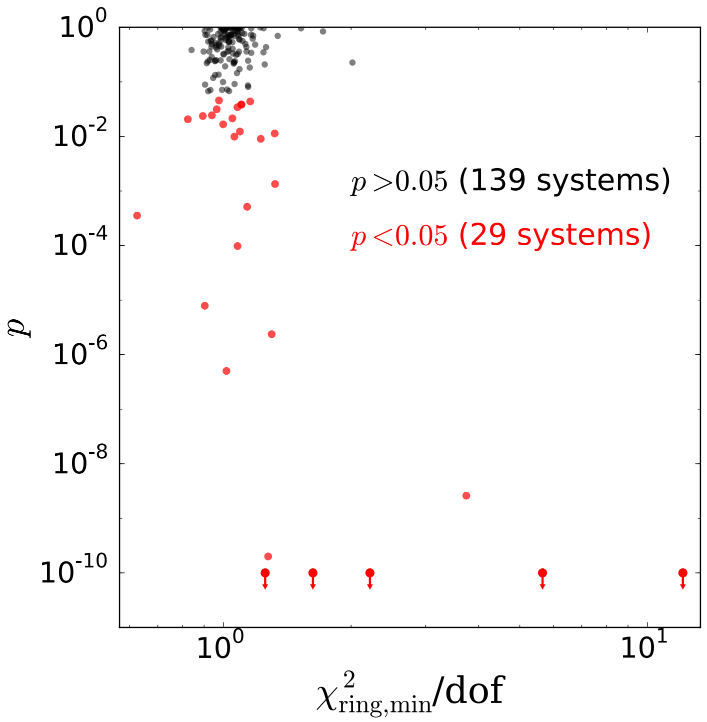

Figure 3.4 The p-values against χ^2/dof for our 168 targets.

3.3.2 Closer consideration of individual systems with $p < 0.05$

The analysis described in Section 3.3 leaves 29 systems with $p < 0.05$. Their lightcurves are carefully examined and compared with the expected ring signature. It turned out that they are not caused by the presence of a ring. We describe the origin of those anomalies individually here. They are interesting objects themselves, and also provide useful examples of possible false-positives for future ring searches.

3.3.2.1 Gravity darkening: KOI-2.01 and 13.01

Fast rotating stars have higher (lower) effective surface temperature in the polar (equatorial) regions because of the stronger centrifugal force along the equatorial plane. Thus the transit lightcurve becomes asymmetric with respect to the central transit time depending on the path of the planet. The anomaly due gravity darkening is not confined preferrentially around the ingress or egress phases unlike the ring signature (see Fig. 3.3 for example), and can be distingushed easily by eye.

Figure 3.5 shows a lightcurve of our tentative candidate KOI-13.01 (Kepler-13 b), which cannot be well fitted anyway even by adding a ring. This system was analysed first by Barnes et al. (2011), who found that the lightcurve is very well explained by gravity darkening. Masuda (2015) presented a further elaborated analysis of KOI-13 (Kepler-13), as well as another gravity darkened system, KOI-2, in our targets.

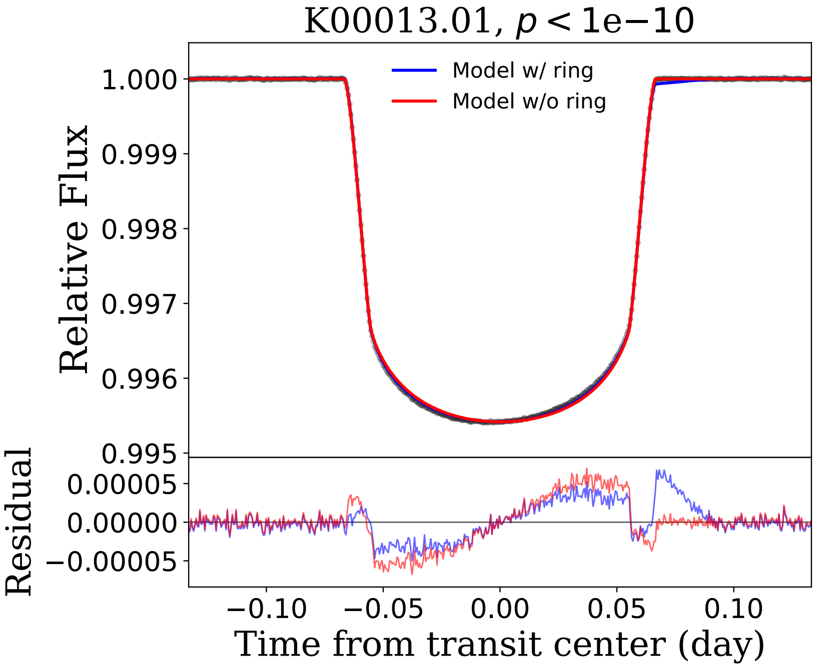

Figure 3.5 Lightcurve of a gravity darkened system, KOI-13.01 (Kepler 13 b).

3.3.2.2 Evaporation of atmosphere: KOI-3794.01

Another tentative candidate, KOI-3794.01 (KIC 12557548, *Kepler*-1520 b), is known as an evaporating planet (e.g. Rappaport et al., 2012), whose lightcurve is shown in Figure 3.6. Indeed, the transit depth of the lightcurves at different epochs (before phase-folded) exhibits significant time-variation, which is inconsistent with the ring hypothesis.

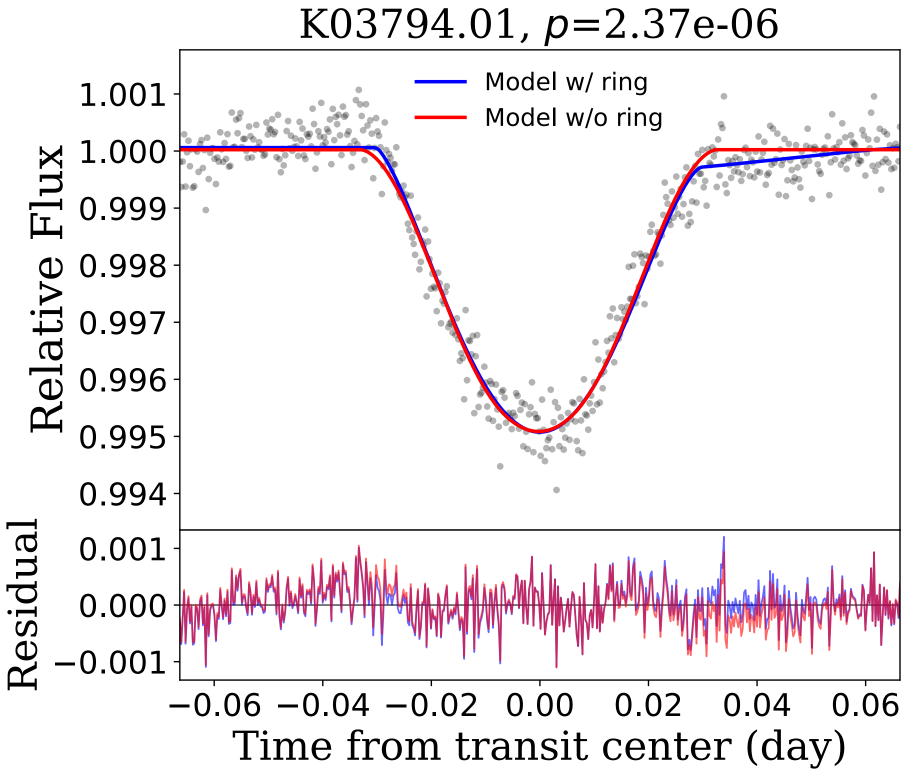

Figure 3.6 Lightcurve of an evaporating planet KOI-3794.01 (Kepler-1520 b)

3.3.2.3 Spot crossing during transit: KOI-3.01, 63.01, 676.01, 1353.01, 1416.01, 1539.01, 1714.01, 1729.01, and 6016.01

Stellar spots add non-negligible anomalous features in the transit lightcurves. Among the 29 tentative candidates with $p < 0.05$, we find that 9 systems are likely explained by spot-crossing events, not by a ring. As a significant example, we show the phase-folded lightcurve of KOI-1714.01 in Figure 3.7, where the entire flux is strongly affected by by spot-crossing events.

Spot-crossing features have been already reported for four systems out of 9 systems; KOI-3.01 (*Kepler*-3b) show frequent spot-crossing anomalies at fairly similar phases, and its planetary orbit is estimated to be misaligned relative to the stellar spin (Sanchis-Ojeda & Winn, 2011). Combining the spot anomalies and the Rossiter-McLaughlin effect of KOI-63.01 (*Kepler*-63 b), Sanchis-Ojeda et al. (2013) concluded that the system has a large spin-orbit misalignment of $\Psi = 104°$. Also the variability of lightcurves due to spot-crossing events have been reported for KOI-676.01 (*Kepler*-210 c) by Sanchis-Ojeda et al. (2013), and for KOI-1353.01 (*Kepler*-289 c) by Schmitt et al. (2014).

The other five systems KOI-1416.01(*Kepler*-850 b), 1539.01, 1714.01, 1729.01, and 6016.01 are classified as possible false positives in *Kepler* CFOP webpages, and we confirmed that there are no ring-like signatures.

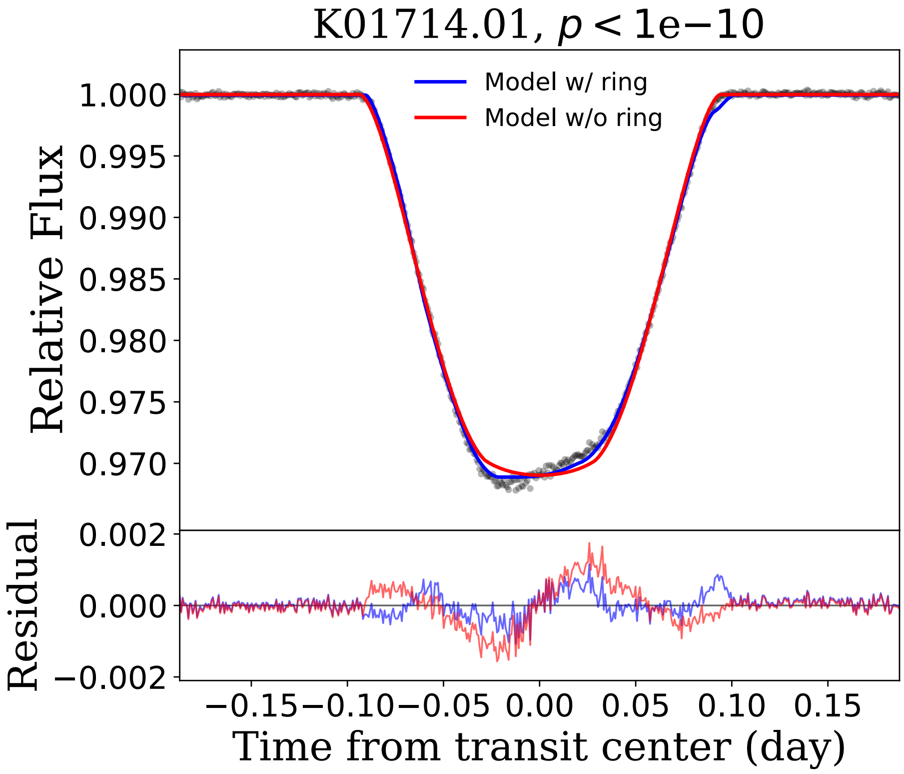

Figure 3.7 Lightcurve of a spot-crossing event, KOI-1714.01.

3.3.2.4 False anomalies due to an inaccurate choice of a transit center: KOI-70.02, 102.01, and 148.01

Phase-folded lightcurves of KOI-70.02, 102.01, and 148.01 show anomalous features around egress and ingress phases. The transit depth of those three systems is very small, and we suspect that the anomalies are simply caused by inaccurate central transit epochs in phase-folding.

Figure 3.8 shows an example for KOI-148.01. In the left panel, we show the lightcurve, which is folded as described in §3.1. As shown in the left panel, the anomalous features appear around the egress and ingress. Then, to find out the origin of the anomaly, we create a phase-folded lightcurve using a linear ephemeris. Specifically, when we fit the individual transit, we fix each transit center to $t_{\mathrm{cen,i}} = t_{\mathrm{cen,0}} + \mathrm{i}P_{\mathrm{orb}}$, where $t_{\mathrm{cen,i}}$ is the transit center at the i-th transit. Here, we retrieve $t_{\mathrm{cen,0}}$ and P_{orb} from the *Kepler* catalog.

The refolded lightcurve is plotted in the right panel, which show that the anomalous features disappear. We made sure that this is also the case for the other two systems, KOI 70.02 and 102.01.

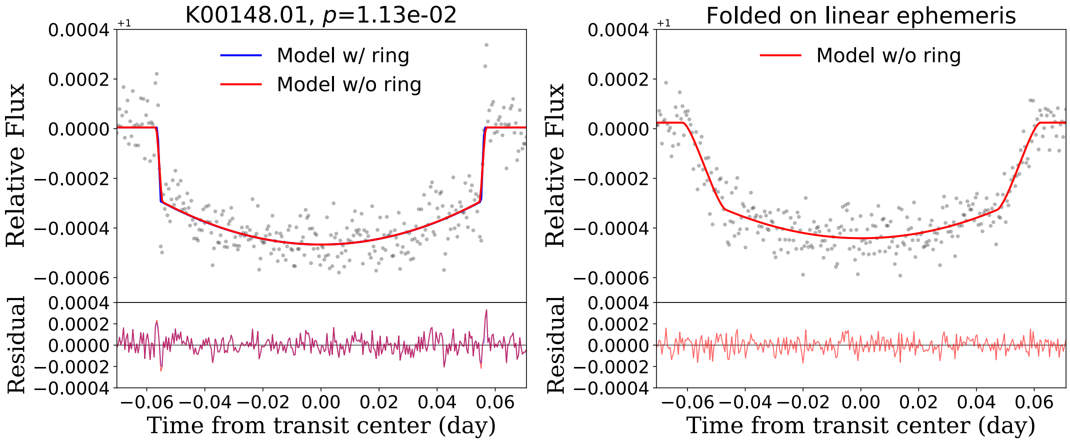

Figure 3.8 Two different phase-folded lightcurves of KOI-148.01.

3.3.2.5 Systems without statistical significance: KOI-4.01, 5.01, 212.01, 214.01, 257.01, 423.01, 433.02, 531.01, 686.01, 872.01, and 1131.01

Out of the 168 targets, we find 11 systems that marginally favor the ring model at $2-3\sigma$ levels: KOI-4.01, 5.01, 212.01, 214.01, 257.01, 423.01, 433.02, 531.01, 686.01, 872.01, and 1131.01. Figure 3.9 shows their lightcurves as well as the best-fit model with and without a ring (in blue and red lines, respectively)).

To examine their significance, we divide their individual transit lightcurves into two groups as described in subsection 3.2.3. If the anomaly is really caused by a ring, both p_{even} and p_{odd} should remain small.

We find that 9 systems have both of p_{even} and p_{odd} larger than 0.32 (i.e., 1σ), and two systems have both p_{even} and p_{odd} with merely 1σ significance: $(0.11, 0.12)$ for KOI-4.01 and (0.029, 0.037) for KOI-257.01. Even though the two systems are likely to be statistical flukes, we examined the lightcurve visually in any case. The lightcurve of KOI-4.01 seems marginally consistent with the ring signature, but the amplitude is so tiny and can be easily produced by random noise. The features of KOI-257.01 are likely to produced by the folding procedure as we discussed in Sec 3.3.2.4 because the transit depth is so small.

We note that the rejection of the null hypothesis of a ring with the level of $p = 0.05$ implies that $168 \times 0.05 = 8.4$ systems are expected to show 2σ signals even if there is no ring at all. Thus 11 marginal systems even if there is no ring system are fairly consistent with our choice of the threshold.

Figure 3.9 Lightcurves of 11 systems without statistical significance listed in B.5

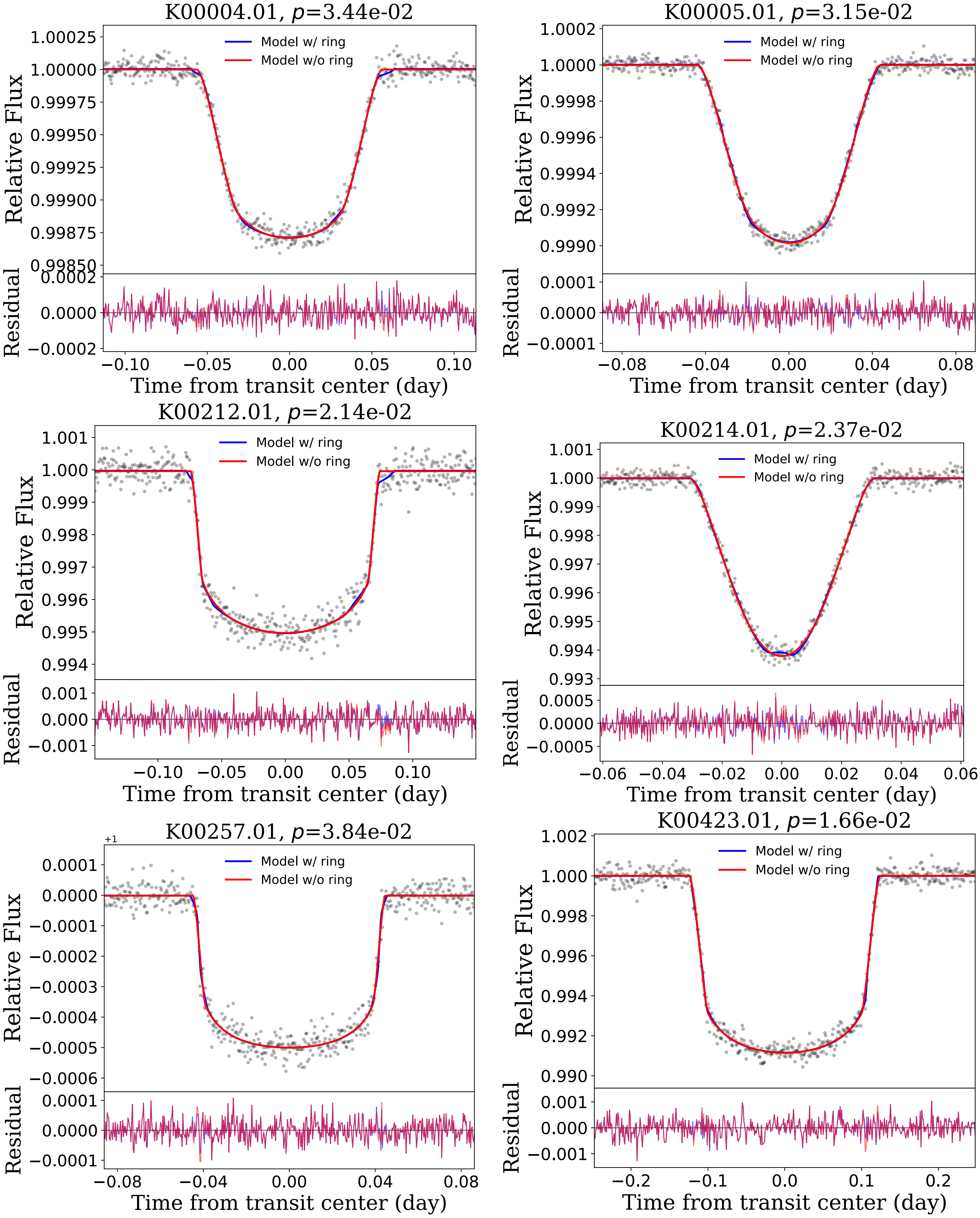

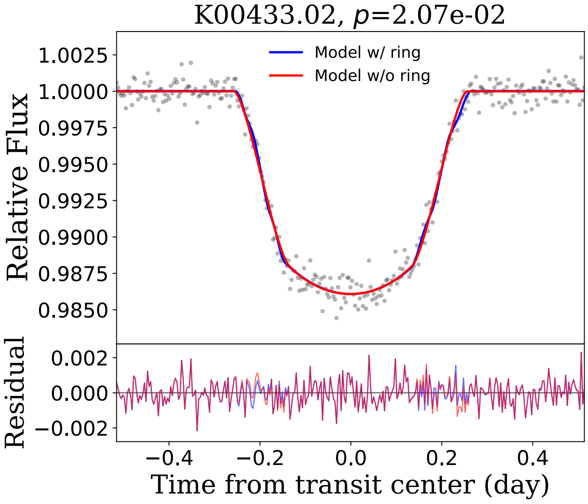
K00433.02, p=2.07e-02

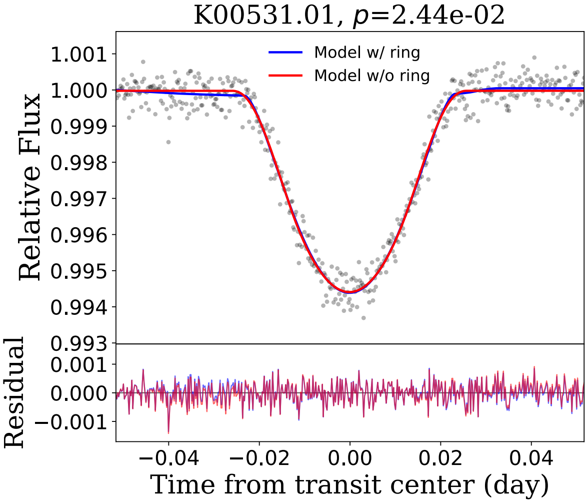
K00531.01, p=2.44e-02

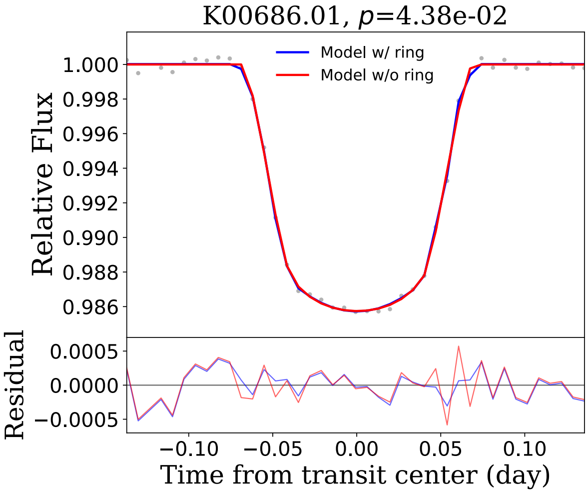
K00686.01, p=4.38e-02

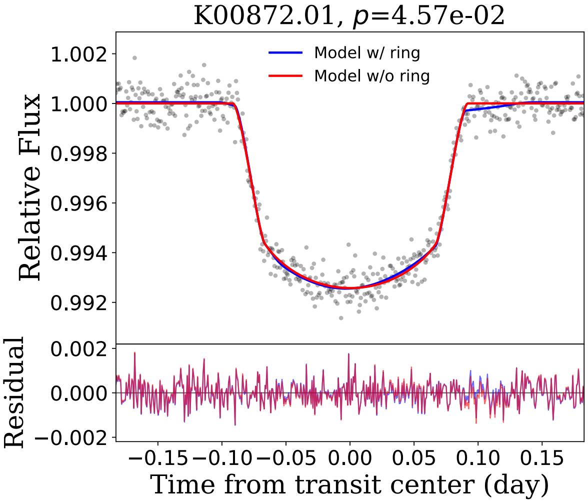
K00872.01, p=4.57e-02

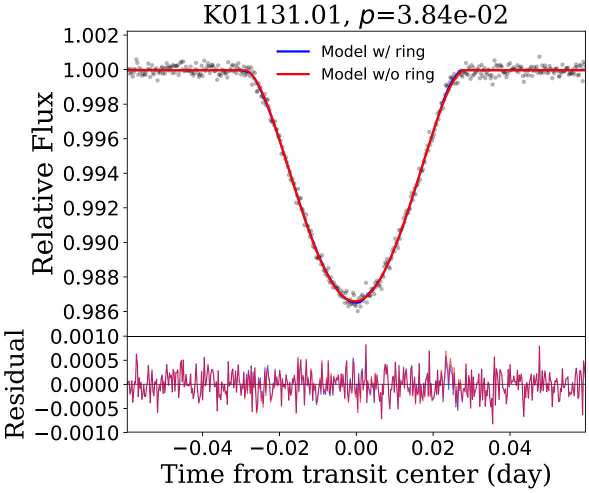
K01131.01, p=3.84e-02

3.3.2.6 The remaining systems: KOI-12.01, 868.01, and 971.01

Finally, we consider the remaining three systems that have not been discussed.

The lightcurve of KOI-12.01 (*Kepler*-448 b) shows anomalous features during the transit, which are significant during -0.03 days to 0.1 days with respect to the central transit epoch. We find that such large pulse-like signals appear also during out-of-transit. Thus they are likely due to stellar activities.

The lightcurves of KOI-971.01 (KIC 11180361) show strong stellar activities, which are typical for multiple star systems (Niemczura et al., 2015), and CFOP webpages also identify this system as false positive. Thus, the planetary rings are not origins of the signals.

The lightcurve of KOI-868.01 shows an anomaly during the egress, which is shown in the left panel of Figure 3.10 along with the best-fit models. The fit yields $\chi^2_{\text{ringless, min}}/\text{dof} = 202.0/190$, $\chi^2_{\text{ring, min}}/\text{dof} = 171.6/195$, and $p = 7.88 \times 10^{-6}$. The analysis based on the binned data supports a Neptune-sized ringed planet of an orbital period of 236 days. The best-fit ring model gives $\theta = 25.5 \pm 10.0^\circ$, $\phi = 12.4 \pm 3.7^\circ$, $T = 0.46 \pm 0.18$, $r_{\text{in/p}} = 1.88 \pm 0.36$, and $r_{\text{out/in}} = 1.63 \pm 0.43$. The radius ratio $R_{\text{p}}/R_\star = 0.099 \pm 0.012$ gives $R_{\text{p}}/R_{\text{J}} = 0.63 \pm 0.08$ assuming the stellar radius $R_\star = 0.657^{+0.022}_{-0.032}\, R_\odot$. The non-vanishing obliquity is consistent with the long alignment timescale $t_{\text{damp}} = 2.95$ Gyr.

In order to check the consistency of signals, we calculate the p-values for the two transits in the short-cadence data separately. As a result, we find $p = 0.76$ and 7.4e-07 for the first and second transits, respectively. Indeed as indicated in the right panel of Figure 3.10, the lightcurves at the first and second transits are systematically different. Therefore KOI-868.01 is unlikely to be a ringed planet. We do not understand the origin of the anomalies because there are only two transits, but suspect that temporal stellar activities or spot-crossing events are responsible.

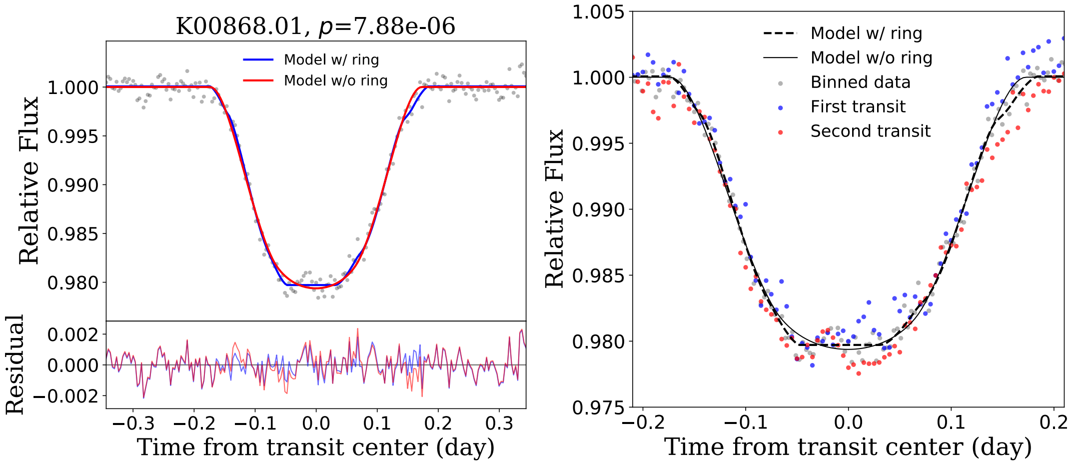

Figure 3.10 Lightcurves of KOI-868.01. Left panel indicates binned lightcurve (black circles) along wih the best-fits of the ringed and ringless models. Right panels shows the comparison for two different transits.

3.3.3 Upper Limits on the Ring Size

3.3.3.1 Result

Given the null detection, we derive upper limits on the outer radius of the possible ring following the method described in Sec 3.2.4. The resulting upper limits, $(R_{\mathrm{out}}/R_{\mathrm{p}})_{\mathrm{upp,\ Aligned}}$, $(R_{\mathrm{out}}/R_{\mathrm{p}})_{\mathrm{upp,\ Saturn}}$, and $(R_{\mathrm{out}}/R_{\star})_{\mathrm{upp}}$, are listed in Table 3.1 to 3.3. If we cannot obtain upper limits due to poor signal-to-noise ratios, we leave those values blank in the tables. The following discussions exclude 18 systems for $(R_{\mathrm{out}}/R_{\mathrm{p}})_{\mathrm{upp,\ Aligned}}$ and 7 systems for $(R_{\mathrm{out}}/R_{\mathrm{p}})_{\mathrm{upp,\ Saturn}}$ that are identified as possible false positives in the *Kepler* Community Follow-up Program (CFOP) webpage.[1]

Figure 3.11 compares upper limits $(R_{\mathrm{out}}/R_{\mathrm{p}})_{\mathrm{upp}}$ for the aligned and Saturn-like configurations against the physical planetary radii. The latter values are computed as $(R_{\mathrm{p}}/R_{\star})_{\mathrm{ringless}} \times R_{\star}$, where the values of $(R_{\mathrm{p}}/R_{\star})_{\mathrm{ringless}}$ are obtained from the ringless model and the stellar radii are taken from the Kepler catalog. Even assuming the ring aligned with the orbital plane, we find fairly tight limits on the ring size (several times R_{p}) for a few tens of systems.

Figure 3.12 is a similar plot to Figure 3.11, but against the equilibrium temperatures T_{eq} of the planets. The exhibited pattern does not reflect the physical dependence of $(R_{\mathrm{out}}/R_{\mathrm{p}})_{\mathrm{upp}}$ on T_{eq}, but simply comes from the fact that the hotter planets have shorter orbital periods, and hence larger signal-to-noise ratios of the phase-folded lightcurve. With sufficient signal-to-noise ratios for future data, however, such plots would provide interesting constraints on the physical properties of rings as a function of melting temperature of different compositions.

As mentioned in Section 3.3.1, the lightcurves of some of the 29 systems with $p < 0.05$ include contributions from the effects other than rings, such as gravity darkening and spot crossing. Nevertheless, we neglect them in deriving the upper limits on $R_{\mathrm{out}}/R_{\mathrm{p}}$. If we fit and remove those effects from the lightcurve, the upper limits may become more stringent. In this sense, the upper limits on $R_{\mathrm{out}}/R_{\mathrm{p}}$ listed in Tables 3.1 and 3.2 would be a bit conservative.

---

[1] https://exofop.ipac.caltech.edu/cfop.php

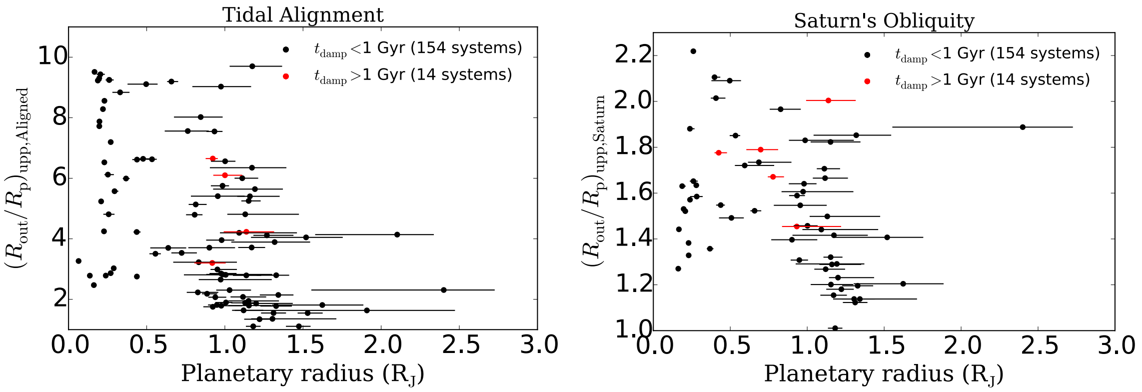

Figure 3.11 Upper limits on $R_{\rm out}/R_{\rm p}$ as a function of $R_{\rm p}$. Left and right panels correspond to the tidally aligned ring, and a ring with Saturn's obliquity, respectively. Black points ($t_{\rm damp} < 1$ Gyr) are likely candidates for the aligned systems. The numbers of systems in panels count all targets with and without limits.

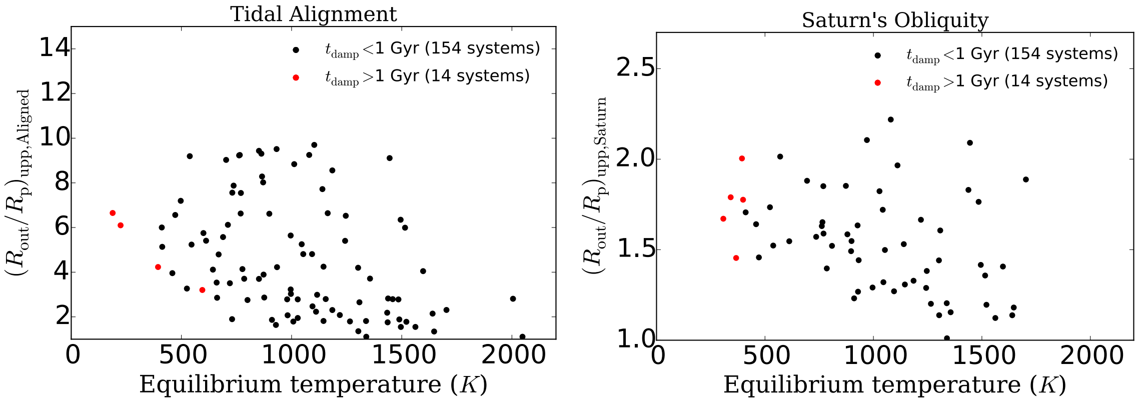

Figure 3.12 Same as Fig. 3.11, but plotted against the equilibrium temperature of the planets.

3.3.3.2 Comparison of Roche radius and upper limits

To understand implications of the upper limits physically, we compare the limits $(R_{\rm out}/R_{\rm p})_{\rm upp}$ with the Roche radii. If we consider ring formation by tidal destruction of incoming objects (e.g. satellites), the outer radius of the ring may be set by the Roche radius:

$$R_{\rm out} \sim 2.45\, R_{\rm p} \left(\frac{\rho_{\rm p}}{\rho_{\rm s}}\right)^{1/3} = 1.6\, R_{\rm p} \left(\frac{\rho_{\rm p}/1\,{\rm g\,cm^{-3}}}{\rho_{\rm s}/3.5\,{\rm g\,cm^{-3}}}\right)^{1/3}, \tag{3.9}$$

where $\rho_{\rm p}$ is the planetary density and $\rho_{\rm s}$ is that of the incoming object. Here we scale the result using $\rho_{\rm p} = 1$ gcm^{-3} and $\rho_{\rm s} = 3.5$ gcm^{-3}, which are the typical values for rocky components in the Solar System.

This implies that, if the inferred upper limit on the ring size $R_{\rm out}/R_{\rm p}$ is much smaller than 1.6, the ring is unlikely to exist even inside that limit — unless $\rho_{\rm s}$ is unreasonably large. In our sample, six systems satisfy $t_{\rm damp} < 1$Gyr and $(R_{\rm out}/R_{\rm p})_{\rm upp,\, Aligned} < 1.6$, and one satisfies $t_{\rm damp} > 1$Gyr and $(R_{\rm out}/R_{\rm p})_{\rm upp,\, Saturn} < 1.6$. We may exclude possible rings around these systems.

3.3.4 Upper Limits on the Ring Occurrence

The above limits on $R_{\rm out}/R_{\rm p}$ translate into the the upper limit on the occurrence rate of rings $q[> x]$ as a function of $x \equiv R_{\rm out}/R_{\rm p}$. Here $q[> x]$ is the probability that a planet has a ring larger than x times the planetary radius. For example, $q[> x = 1]$ is simply the occurrence rate of rings, and $q[> x = 2]$ is that of rings larger than twice the planetary radii.

We attempt to estimate the upper limit on $q[> x]$ as follows. For a given value of x, consider n samples extracted from systems with $q[> x]$, for which the rings with $R_{\rm out}/R_{\rm p} > x$ should have been readily detectable — so this may be chosen to be $N[< x]$, the number of systems with $(R_{\rm out}/R_{\rm p})_{\rm upp} < x$. Then the probability that we detect $n_{\rm obs}$ rings with $R_{\rm out}/R_{\rm p} \geq x$ out of the n samples is given simply by the binominal distribution:

$$\mathrm{Prob}(n_{\rm obs}|q[> x], n) =_n C_{n_{\rm obs}}\, q[> x]^{n_{\rm obs}}\, (1 - q[> x])^{n-n_{\rm obs}}. \tag{3.10}$$

Without any prior knowledge of $q[> x]$ nor $n_{\rm obs}$, we assume the uniform distribution for $\mathrm{Prob}(q[> x])$ and $\mathrm{Prob}(n_{\rm obs})$ with proper normalizations:

$$\int_0^1 \mathrm{Prob}\,(q[> x]|n)\, dq[> x] = 1 \to \quad \mathrm{Prob}\,(q[> x]|n) = 1 \tag{3.11}$$

$$\sum_{n_{\rm obs}=0}^{n} \mathrm{Prob}(n_{\rm obs}|n) = 1 \to \mathrm{Prob}(n_{\rm obs}|n) = 1/(n+1) \tag{3.12}$$

According to Bayes' theorem, we obtain

$$\begin{aligned}\mathrm{Prob}(q[> x]|n_{\rm obs} = 0, n) &= \frac{\mathrm{Prob}(q[> x]|n)\mathrm{Prob}(n_{\rm obs} = 0|q[> x], n)}{\mathrm{Prob}(n_{\rm obs} = 0|n)} \\ &= (n + 1)(1 - q[> x])^n \end{aligned} \tag{3.13}$$

The corresponding cumulative distribution function for $q[> x]$ is given by:

$$\mathrm{CDF}(q[> x]) = 1 - (1 - q[> x])^{n+1}. \tag{3.14}$$

Here, we would like to obtain the 95% upper limits of $q[> x]$. Thus, the above equation gives

$$q[> x]_{\rm upp} = 1 - (0.05)^{\frac{1}{n+1}}. \tag{3.15}$$

Now, we substitute the values of $N[< x]$ plotted in Fig 3.12 into n, and obtain the upper limits of $q[> x]$ as a function of x.

Figure 3.13 shows $q[> x]_{\rm upp}$ using $N[< (R_{\rm out}/R_{\rm p})_{\rm upp,\, Aligned}]$, and $N[< (R_{\rm out}/R_{\rm p})_{\rm upp,\, Saturn}]$. Physically speaking, the limit $(R_{\rm out}/R_{\rm p})_{\rm upp,\, Aligned}$ is appropriate only for systems with small values of $t_{\rm damp}$, which have likely achieved tidal alignment. On the other hand, $(R_{\rm out}/R_{\rm p})_{\rm upp,\,Saturn}$ may be more relevant for those with large values of $t_{\rm damp}$. Therefore, we distinguish the systems with $t_{\rm damp} < 1\,{\rm Gyr}$ and $t_{\rm damp} > 1\,{\rm Gyr}$ in the plot. The more relevant subset is shown with thick lines in each panel.

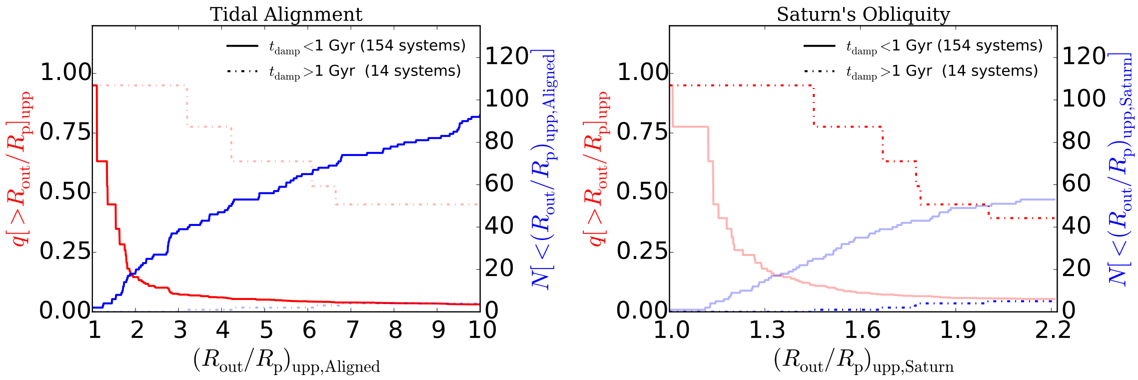

Figure 3.13 Cumulative frequency of upper limits $N[<(R_{\rm out}/R_{\rm p})_{\rm upp}]$ and upper imits on the occurence rate of rings $q[>x]_{\rm upp}$ in Eq (3.15). The left panel assumes the tidal alignment, while the right panel assumes the Saturn's obliquity. Thick lines in the left panel correspond to 154 systems with $t_{\rm damp} < 1{\rm Gyr}$, while those in the right panel to 14 systems with $t_{\rm damp} > 1{\rm Gyr}$.

3.4 Summary

We have performed a systematic and intensive search for exo-rings among the 168 *Kepler* planet candidates. The targets are homogeneously selected from all the KOIs that have the signal-to-noise ratio of the phase-folded lightcurves exceeding 100. As a result, a majority of our targets are short-period planets. This sample is complementary to that of long-period planets analyzed by Aizawa et al. (2017), and significantly larger than the 21 short-period planet samples by Heising et al. (2015).

For all the targets, we obtained the best-fit ringless and ringed model parameters from their individual phase-folded lightcurves following Aizawa et al. (2017). Then, we compare the two best-fits, and we select 29 systems as tentative candidates for which the ringed-model fit better explained the data than the ringless-model fit.

Those 29 systems are further examined individually and visually, and we conclude that none of them exhibits clear signature of a planetary ring. Instead, we derive upper limits on the ratio of the outer radius of the possible ring and the planetary radius assuming two different configurations; the tidally aligned ring and the Saturn's ring. The derived upper limits for individual systems are summarized in Tables 3.1 to 3.3.

The distribution of those upper limits can be used to derive the statistical upper limits on the occurrence rate of planetary rings as a function of $R_{\rm out}/R_{\rm p}$. We found that ${\rm Prob}(R_{\rm out}/R_{\rm p} > 2)$ should be less than 15 percent for tidally aligned ring systems.

Given that our targets are mainly in close-in orbits, the null detection of rings may not be so surprising (e.g. Schlichting & Chang, 2011). This is also consistent with the fact that dense planetary rings in our Solar System are discovered exclusively at temperatures close to 70 K (Hedman, 2015).

Nevertheless, our current result clearly indicates that the existing *Kepler* data are already accurate and precise enough to probe the planetary rings of a comparable size to the planet itself. This is quite encouraging, and the future effort towards the discovery of ring would likely be rewarding as we have witnessed numerous unexpected surprises in the history of astronomy, and especially exoplanetary science.

We also believe that the current methodology and examples of false-positives would be very useful in such future searches for planetary rings with improved datasets.

Having said so, it is important to emphasize other independent approaches to the ring survey. For instance, Zuluaga et al. (2015) pointed out that KOIs flagged as “FALSE POSITIVES”, which we intentionally exclude from our current targets, may be promising because they could include possible ringed planets that are misinterpreted as anomalously large planets. Also a precession of planetary rings may induce a detectable level of transit depth variation (e.g. Carter & Winn, 2010; Heising et al., 2015). In addition, scattering and diffraction of the star light by the ring particles may be observable depending on the size of ring particles, especially through multi-band photometry in space.

Therefore, we expect that the upcoming observations with TESS and PLATO will substantially improve the observational searches for and understanding of the exoplanetary rings combined with the current result of the *Kepler* data.

Table 3.1: Parameters and statistics of 13 systems with $p < 0.001$

KOI	*Kepler*	P_{orb}[1] (day)	t_{damp} (Gyr)	$(R_{\mathrm{out}}/R_{\mathrm{p}})_{\mathrm{upp,\ Aligned}}$	$(R_{\mathrm{p}}/R_{\star})_{\mathrm{ringless}}$	p	$(\chi^2_{\mathrm{ringless,min}}, \chi^2_{\mathrm{ring,min}}, N_{\mathrm{bin}})$	(S/N)	Comment[2]
2.01	2 b	2.20	2.60e-05	1.11	0.07755 ± 2e-05	5.02e-07	(534.22, 494.94, 500)	4357.03	GD
3.01	3 b	4.89	8.76e-04	2.75	0.05886 ± 3e-05	2.60e-09	(2011.23, 1820.95, 500)	2403.33	Spot
13.01	13 b	1.76	7.92e-06	1.63	0.064683 ± 4e-06	<1e-10	(8830.73, 5904.78, 500)	6359.84	GD
63.01	63 b	9.43	5.18e-03	2.44	0.06481 ± 4e-05	<1e-10	(1222.04, 1078.89, 500)	732.29	Spot
102.01	-	1.74	7.01e-05	5.51	0.02810 ± 6e-05	9.78e-05	(554.11, 525.66, 500)	432.74	Bad Fold
676.01	210 c	7.97	5.35e-03	7.20	0.0520 ± 5e-04	2.00e-10	(693.78, 620.69, 500)	302.61	Spot
868.01	-	236.00	2.95e+01	6.65	0.144 ± 1e-03	7.88e-06	(202.04, 171.63, 203)	182.23	Others
971.01	-	0.53	9.00e-10	8.13	0.1 ± 1e+00	3.54e-04	(319.16, 304.58, 500)	257.01	FP & Others
1416.01	840 b	2.50	3.55e-05	1.74	0.1459 ± 2e-04	5.14e-04	(579.31, 553.80, 500)	919.15	FP & Spot
1539.01	-	2.82	1.20e-05	1.10	0.2568 ± 2e-04	<1e-10	(982.31, 791.58, 500)	1364.17	FP & Spot
1714.01	-	2.74	5.29e-06	1.10	0.17618 ± 2e-05	<1e-10	(6978.85, 2755.22, 500)	688.33	FP & Spot
1729.01	-	5.20	2.88e-04	1.80	0.1764 ± 3e-04	<1e-10	(688.30, 610.78, 500)	816.17	FP & Spot
3794.01	1520 b	0.65	3.27e-07	-	0.101 ± 3e-03	2.37e-06	(678.22, 632.70, 500)	265.86	Evap

---

[1] Values from *Kepler* Object of Interest (KOI) Catalog Q1-Q17 DR 25(https://exoplanetarchive.ipac.caltech.edu/)

[2] FP=Possible False Positive (https://exofop.ipac.caltech.edu/cfop.php); GD = Gravity Darkening (B.1); Evap = Evaporating planet (B.2); Spot=Spot Crossing (B.3); Bad Fold = incorrect data folding (B.4); Small = non-significant signal (B.5); Others = B.6;

Table 3.2: Parameters and statistics of 16 systems with $0.001 < p < 0.05$

KOI	*Kepler*	P_{orb}[1] (day)	t_{damp} (Gyr)	$(R_{\mathrm{out}}/R_{\mathrm{p}})_{\mathrm{upp,\,Aligned}}$	$(R_{\mathrm{out}}/R_{\mathrm{p}})_{\mathrm{upp,\,Saturn}}$	$(R_{\mathrm{out}}/R_{\star})_{\mathrm{upp}}$	$(R_{\mathrm{p}}/R_{\star})_{\mathrm{ringless}}$	p	$(\chi^2_{\mathrm{ringless,min}}, \chi^2_{\mathrm{ring,min}}, N_{\mathrm{bin}})$	(S/N)	Comment[2]
4.01	-	3.85	1.76e-04	-	-	-	0.0394 ± 3e-04	3.44e-02	(538.39, 525.32, 500)	148.29	FP & Small
5.01	-	4.78	6.05e-04	-	-	-	0.04 ± 1e-02	3.15e-02	(481.35, 469.45, 500)	455.35	FP & Small
12.01	448 b	17.86	1.44e-02	1.86	1.23	0.107	0.09018 ± 5e-05	1.23e-02	(548.57, 532.47, 500)	792.22	Others
70.02	20 b	3.70	1.23e-03	2.47	1.27	0.022	0.01799 ± 9e-05	1.34e-03	(671.05, 644.41, 500)	128.93	Bad Fold
148.01	48 b	4.78	2.46e-03	9.51	1.44	0.026	0.0196 ± 1e-04	1.13e-02	(663.02, 643.29, 500)	102.75	Bad Fold
212.01	-	5.70	1.04e-03	-	1.72	0.093	0.0649 ± 3e-04	2.14e-02	(525.10, 511.11, 500)	159.08	Small
214.01	424 b	3.31	1.46e-04	2.99	-	-	0.104 ± 3e-03	2.37e-02	(446.95, 435.27, 500)	448.51	Small
257.01	506 b	6.88	5.14e-03	9.25	2.22	0.033	0.0224 ± 2e-04	3.84e-02	(550.10, 537.05, 500)	161.18	Small
423.01	39 b	21.09	2.12e-02	3.89	1.85	0.129	0.0890 ± 6e-04	1.66e-02	(500.13, 486.18, 500)	225.79	Small
433.02	553 c	328.24	7.94e+01	6.10	-	-	0.120 ± 7e-03	2.07e-02	(250.09, 238.97, 303)	112.04	Small
531.01	-	3.69	2.97e-04	-	-	-	0.096 ± 4e-03	2.44e-02	(469.53, 457.33, 500)	183.64	Small
686.01	-	52.51	3.36e-01	4.68	-	-	0.118 ± 4e-03	4.38e-02	(46.09, 31.21, 40)	153.64	FP & Small
872.01	46 b	33.60	1.36e-01	-	-	-	0.084 ± 2e-03	4.57e-02	(486.30, 475.20, 500)	173.00	Small
1131.01	-	0.70	2.08e-07	1.02	1.02	0.211	0.2 ± 7e-02	3.84e-02	(549.24, 536.21, 500)	727.17	FP & Small
1353.01	289 c	125.87	4.46e+00	4.23	2.00	0.153	0.1048 ± 6e-04	9.04e-03	(544.28, 525.28, 442)	198.14	Spot
6016.01	-	4.55	7.76e-05	1.32	1.65	0.463	0.23 ± 2e-02	9.91e-03	(503.24, 487.04, 472)	1719.88	FP & Spot

---

[1] Values from *Kepler* Object of Interest (KOI) Catalog Q1-Q17 DR 25(https://exoplanetarchive.ipac.caltech.edu/)

[2] FP=Possible False Positive (https://exofop.ipac.caltech.edu/cfop.php); GD = Gravity Darkening (B.1); Evap = Evaporating planet (B.2); Spot=Spot Crossing (B.3); Bad Fold = incorrect data folding (B.4); Small = non-significant signal (B.5); Others = B.6;

Table 3.3: Parameters and statistics of 139 systems with $p > 0.05$

KOI	*Kepler*	$P_{\rm orb}$[1] (day)	$t_{\rm damp}$ (Gyr)	$(R_{\rm out}/R_{\rm p})_{\rm upp,\ Aligned}$	$(R_{\rm out}/R_{\rm p})_{\rm upp,\ Saturn}$	$(R_{\rm out}/R_\star)_{\rm upp}$	$(R_{\rm p}/R_\star)_{\rm ringless}$	p	($\chi^2_{\rm ringless,min}$, $\chi^2_{\rm ring,min}$, $N_{\rm bin}$)	(S/N)	Comment[2]
1.01	1 b	2.47	4.20e-05	1.11	1.01	0.127	0.1259 ± 7e-04	1.00e+00	(511.76, 511.76, 500)	9353.67	-
7.01	4 b	3.21	3.42e-04	5.99	1.36	0.031	0.02445 ± 7e-05	3.41e-01	(572.68, 566.10, 500)	284.12	-
10.01	8 b	3.52	1.11e-04	1.78	1.20	0.109	0.0940 ± 4e-04	7.51e-01	(491.06, 488.39, 500)	1565.89	-
17.01	6 b	3.23	9.43e-05	3.71	1.15	0.105	0.0932 ± 1e-04	3.60e-01	(456.00, 450.92, 500)	2671.28	-
18.01	5 b	3.55	1.12e-04	2.14	1.14	0.088	0.0790 ± 1e-04	1.36e-01	(482.37, 474.17, 500)	2054.24	-
20.01	12 b	4.44	1.69e-04	1.81	1.20	0.138	0.1179 ± 1e-04	4.81e-01	(583.61, 578.28, 500)	3127.91	-
22.01	422 b	7.89	1.34e-03	1.95	1.82	0.135	0.0956 ± 2e-04	1.33e-01	(473.51, 465.41, 500)	1886.93	-
42.01	410 A b	17.83	9.29e-02	8.28	-	-	0.0169 ± 2e-04	1.00e+00	(484.28, 484.20, 500)	144.80	-
46.01	101 b	3.49	3.06e-04	9.11	2.09	0.048	0.0320 ± 2e-04	2.20e-01	(451.10, 444.68, 500)	152.32	-
64.01	-	1.95	2.93e-05	2.81	-	-	0.04 ± 1e-02	1.45e-01	(532.93, 524.06, 500)	286.21	-
69.01	93 b	4.73	2.94e-03	2.78	-	-	0.0157 ± 2e-04	1.00e+00	(525.95, 526.55, 500)	265.72	-
70.01	20 c	10.85	1.62e-02	9.25	1.65	0.040	0.0289 ± 1e-04	6.40e-01	(482.40, 479.07, 500)	225.66	-
75.01	-	105.88	3.63e+00	3.20	-	-	0.0378 ± 2e-04	7.06e-01	(575.70, 572.23, 500)	208.26	-
82.01	102 e	16.15	6.07e-02	5.24	-	-	0.0289 ± 5e-04	9.92e-01	(516.92, 516.39, 500)	248.53	-
84.01	19 b	9.29	1.50e-02	9.23	1.63	0.033	0.02376 ± 9e-05	8.74e-01	(490.32, 488.50, 500)	220.22	-
85.01	65 c	5.86	3.38e-03	6.53	1.38	0.021	0.01652 ± 5e-05	4.95e-01	(553.43, 548.49, 500)	191.04	-
94.01	89 d	22.34	3.70e-02	3.71	1.40	0.089	0.0695 ± 2e-04	3.25e-01	(492.67, 486.86, 500)	858.57	-
94.02	89 c	10.42	1.20e-02	8.84	-	-	0.0255 ± 1e-04	7.58e-01	(548.33, 545.41, 500)	165.65	-
94.03	89 e	54.32	8.66e-01	-	-	-	0.0409 ± 5e-04	4.59e-01	(480.16, 475.61, 500)	201.68	-
97.01	7 b	4.89	2.53e-04	1.55	-	-	0.0823 ± 1e-04	3.32e-01	(518.47, 512.42, 500)	1580.40	-
98.01	14 b	6.79	1.21e-03	2.18	-	-	0.0455 ± 1e-04	6.91e-01	(518.91, 515.68, 500)	588.69	-
100.01	-	9.97	2.14e-03	-	-	-	0.055 ± 3e-03	7.82e-01	(541.86, 539.14, 500)	188.32	-
103.01	-	14.91	4.75e-02	-	1.88	0.040	0.0271 ± 2e-04	5.61e-01	(458.09, 454.44, 500)	114.38	-
104.01	94 b	2.51	1.93e-04	3.03	-	-	0.0390 ± 7e-04	8.64e-01	(520.19, 518.18, 500)	276.45	-
105.01	463 b	8.98	8.95e-03	-	1.58	0.041	0.0300 ± 2e-04	3.57e-01	(535.74, 529.75, 500)	175.89	-
108.01	103 b	15.97	4.70e-02	-	-	-	0.0212 ± 5e-04	7.25e-02	(507.09, 496.74, 500)	109.94	-
108.02	103 c	179.61	3.21e+01	-	-	-	0.0335 ± 7e-04	9.73e-01	(538.74, 537.79, 500)	118.02	-

---

[1] Values from *Kepler* Object of Interest (KOI) Catalog Q1-Q17 DR 25(https://exoplanetarchive.ipac.caltech.edu/)

[2] FP=Possible False Positive (https://exofop.ipac.caltech.edu/cfop.php); GD = Gravity Darkening (B.1); Evap = Evaporating planet (B.2); Spot=Spot Crossing (B.3); Bad Fold = incorrect data folding (B.4); Small = non-significant signal (B.5); Others = B.6;

KOI	*Kepler*	$P_{\rm orb}$ (day)	$t_{\rm damp}$ (Gyr)	$(R_{\rm out}/R_{\rm p})_{\rm upp,\ Aligned}$	$(R_{\rm out}/R_{\rm p})_{\rm upp,\ Saturn}$	$(R_{\rm out}/R_\star)_{\rm upp}$	$(R_{\rm p}/R_\star)_{\rm ringless}$	p	$(\chi^2_{\rm ringless,min},\ \chi^2_{\rm ring,min},\ N_{\rm bin})$	(S/N)	Comment
111.01	104 b	11.43	2.53e-02	9.43	-	-	0.0208 ± 6e-04	9.95e-01	(482.47, 482.07, 500)	149.05	-
111.02	104 c	23.67	2.16e-01	-	-	-	0.0205 ± 7e-04	1.00e+00	(507.95, 508.06, 500)	102.89	-
111.03	104 d	51.76	1.86e+00	-	-	-	0.0230 ± 2e-04	6.83e-01	(506.56, 503.35, 500)	104.53	-
115.01	105 b	5.41	2.21e-03	4.81	-	-	0.0243 ± 5e-04	1.00e+00	(533.29, 534.26, 500)	164.82	-
119.01	108 b	49.18	4.74e-01	4.79	-	-	0.0403 ± 5e-04	7.28e-01	(443.98, 441.43, 500)	146.21	-
122.01	95 b	11.52	1.92e-02	-	1.63	0.028	0.0203 ± 1e-04	3.48e-01	(612.05, 605.09, 500)	124.25	-
123.01	109 b	6.48	4.52e-03	4.25	-	-	0.0179 ± 4e-04	9.59e-01	(567.41, 566.21, 500)	104.11	-
125.01	468 b	38.48	1.24e-01	6.66	1.21	0.165	0.1396 ± 5e-04	1.71e-01	(539.81, 531.35, 500)	586.79	FP
127.01	77 b	3.58	1.58e-04	1.81	1.31	0.120	0.0981 ± 3e-04	5.86e-01	(497.21, 493.42, 500)	970.07	-
128.01	15 b	4.94	3.96e-04	1.79	-	-	0.1026 ± 5e-04	2.50e-01	(474.56, 468.17, 500)	1113.76	-
129.01	470 b	24.67	4.53e-04	2.78	1.76	0.114	0.0805 ± 4e-04	4.45e-01	(485.79, 481.08, 500)	211.74	-
130.01	-	34.19	5.36e-02	2.95	-	-	0.1142 ± 7e-04	6.75e-02	(457.67, 448.15, 500)	785.48	FP
131.01	471 b	5.01	4.38e-04	2.65	1.61	0.105	0.0765 ± 4e-04	2.37e-01	(453.50, 447.26, 500)	333.34	FP
135.01	43 b	3.02	8.54e-05	1.88	-	-	0.0855 ± 2e-04	3.59e-01	(442.14, 437.21, 500)	1246.59	-
137.01	18 c	7.64	3.37e-03	6.62	1.55	0.058	0.0426 ± 1e-04	9.21e-01	(485.86, 484.43, 500)	425.15	-
137.02	18 d	14.86	1.90e-02	3.51	-	-	0.0541 ± 5e-04	4.42e-01	(460.59, 456.11, 500)	444.75	-
139.01	111 c	224.78	4.17e+01	-	-	-	0.053 ± 1e-03	2.45e-01	(471.58, 465.18, 500)	127.91	-
141.01	-	2.62	1.38e-04	6.64	-	-	0.055 ± 2e-03	1.83e-01	(570.48, 561.75, 500)	325.66	-
143.01	-	22.65	5.32e-02	7.41	-	-	0.06 ± 2e-02	9.99e-01	(479.24, 479.01, 500)	115.81	FP
144.01	472 b	4.18	9.22e-04	2.86	-	-	0.0357 ± 8e-04	9.96e-01	(512.22, 511.84, 500)	206.94	-
148.02	48 c	9.67	1.31e-02	-	1.57	0.038	0.0280 ± 2e-04	2.60e-01	(509.73, 503.01, 500)	153.76	-
149.01	473 b	14.56	2.67e-02	-	-	-	0.0286 ± 2e-04	9.36e-01	(530.61, 529.21, 500)	105.77	-
150.01	112 b	8.41	1.03e-02	-	1.52	0.035	0.0263 ± 2e-04	6.78e-02	(512.70, 502.05, 500)	108.37	-
152.01	79 d	52.09	6.40e-01	-	-	-	0.0506 ± 6e-04	2.86e-01	(462.65, 456.81, 500)	166.31	-
153.01	113 c	8.93	1.12e-02	-	-	-	0.031 ± 1e-03	9.01e-01	(494.06, 492.45, 500)	132.84	-
153.02	113 b	4.75	2.13e-03	-	-	-	0.0254 ± 7e-04	9.98e-01	(595.02, 594.71, 500)	136.46	-
156.03	114 d	11.78	2.74e-02	-	-	-	0.035 ± 1e-03	4.26e-01	(504.95, 499.90, 500)	156.89	-
157.01	11 c	13.02	2.93e-02	-	-	-	0.0253 ± 3e-04	6.32e-01	(495.87, 492.40, 500)	120.27	-
157.02	11 d	22.69	1.32e-01	-	-	-	0.0275 ± 3e-04	9.20e-01	(485.51, 484.09, 500)	121.48	-
157.03	11 e	32.00	2.72e-01	-	-	-	0.0381 ± 7e-04	5.94e-01	(535.66, 531.63, 500)	131.42	-
161.01	475 b	3.11	4.52e-04	2.78	-	-	0.0309 ± 7e-04	9.80e-01	(525.60, 524.80, 500)	173.70	-
182.01	-	3.48	1.15e-04	1.61	1.17	0.154	0.1359 ± 3e-04	9.56e-01	(532.88, 531.71, 500)	907.22	FP

KOI	*Kepler*	$P_{\rm orb}$ (day)	$t_{\rm damp}$ (Gyr)	$(R_{\rm out}/R_{\rm p})_{\rm upp,\ Aligned}$	$(R_{\rm out}/R_{\rm p})_{\rm upp,\ Saturn}$	$(R_{\rm out}/R_\star)_{\rm upp}$	$(R_{\rm p}/R_\star)_{\rm ringless}$	p	$(\chi^2_{\rm ringless,min}, \chi^2_{\rm ring,min}, N_{\rm bin})$	(S/N)	Comment
183.01	423 b	2.68	5.46e-05	1.79	1.20	0.144	0.1240 ± 2e-04	7.58e-01	(531.38, 528.53, 500)	1927.67	-
186.01	485 b	3.24	9.44e-05	5.40	1.29	0.145	0.1177 ± 5e-04	7.09e-02	(463.20, 453.68, 500)	907.61	-
188.01	425 b	3.80	1.89e-04	2.07	-	-	0.1137 ± 8e-04	6.82e-01	(505.55, 502.34, 500)	763.67	-
189.01	486 b	30.36	7.40e-02	3.96	1.64	0.182	0.132 ± 1e-03	8.43e-01	(491.38, 489.33, 500)	495.16	FP
191.01	487 b	15.36	1.05e-02	2.85	-	-	0.1130 ± 6e-04	1.93e-01	(498.81, 491.33, 500)	722.16	-
192.01	427 b	10.29	2.75e-03	5.64	1.29	0.110	0.0892 ± 2e-04	6.18e-01	(575.01, 570.87, 500)	577.13	-
194.01	488 b	3.12	7.67e-05	1.36	1.14	0.145	0.1346 ± 4e-04	4.36e-01	(557.03, 551.56, 500)	894.33	-
195.01	426 b	3.22	1.05e-04	2.31	-	-	0.117 ± 1e-03	7.15e-01	(510.76, 507.73, 500)	806.33	-
196.01	41 b	1.86	2.41e-05	1.75	-	-	0.1001 ± 5e-04	8.59e-02	(567.27, 556.20, 500)	932.49	-
197.01	489 b	17.28	2.22e-02	9.19	1.52	0.124	0.0916 ± 8e-04	9.92e-02	(495.08, 485.81, 500)	370.23	-
199.01	490 b	3.27	7.58e-05	4.05	1.41	0.120	0.0923 ± 4e-04	7.36e-01	(506.74, 503.88, 500)	652.81	-
200.01	74 b	7.34	9.60e-04	2.80	-	-	0.0911 ± 7e-04	8.52e-01	(514.93, 512.85, 500)	430.98	-
201.01	491 b	4.23	3.04e-04	2.23	1.97	0.116	0.0806 ± 5e-04	8.58e-01	(441.44, 439.70, 500)	657.38	-
202.01	412 b	1.72	1.46e-05	1.34	1.18	0.117	0.103 ± 2e-03	7.27e-01	(448.69, 446.11, 500)	895.88	-
203.01	17 b	1.49	8.41e-06	1.55	1.12	0.146	0.1323 ± 1e-04	4.32e-01	(619.80, 613.66, 500)	3014.03	-
204.01	44 b	3.25	1.03e-04	2.79	-	-	0.0802 ± 8e-04	9.14e-02	(527.39, 517.27, 500)	348.47	-
205.01	492 b	11.72	6.63e-03	3.53	-	-	0.097 ± 1e-03	2.29e-01	(522.98, 515.67, 500)	369.77	-
206.01	433 b	5.33	4.32e-04	6.35	1.42	0.082	0.0633 ± 4e-04	6.08e-01	(533.62, 529.71, 500)	257.22	-
208.01	493 b	3.00	9.31e-05	2.82	1.83	0.125	0.0865 ± 5e-04	7.29e-01	(568.67, 565.42, 500)	202.89	-
209.01	117 c	50.79	3.85e-01	5.41	1.55	0.094	0.0698 ± 4e-04	7.41e-01	(510.66, 507.82, 500)	358.63	-
209.02	117 b	18.80	3.14e-02	3.70	-	-	0.0466 ± 5e-04	2.40e-01	(471.61, 465.15, 500)	237.63	-
217.01	71 b	3.91	1.60e-04	5.25	1.32	0.166	0.1334 ± 5e-04	2.44e-01	(564.36, 556.70, 500)	1059.21	-
229.01	497 b	3.57	3.05e-04	-	-	-	0.0505 ± 5e-04	2.48e-01	(486.02, 479.46, 500)	117.38	-
232.01	122 c	12.47	1.25e-02	-	1.49	0.059	0.0438 ± 2e-04	5.17e-01	(469.98, 465.94, 500)	269.24	-
244.01	25 c	12.72	1.63e-02	4.23	-	-	0.03561 ± 9e-05	2.16e-01	(522.14, 514.67, 500)	429.53	-
244.02	25 b	6.24	4.08e-03	8.56	1.33	0.023	0.01875 ± 6e-05	5.76e-01	(459.81, 456.24, 500)	223.07	-
245.01	37 d	39.79	1.17e+00	-	-	-	0.0227 ± 3e-04	9.98e-01	(504.20, 503.92, 500)	154.71	-
246.01	68 A b	5.40	3.05e-03	7.72	1.53	0.023	0.01688 ± 4e-05	1.00e+00	(490.53, 498.47, 500)	249.46	-
250.01	26 b	12.28	2.19e-02	-	-	-	0.0480 ± 5e-04	1.18e-01	(468.86, 460.52, 500)	108.72	-
251.01	125 b	4.16	1.03e-03	-	-	-	0.0450 ± 9e-04	9.99e-01	(522.41, 522.17, 500)	136.30	-
254.01	45 b	2.46	4.52e-05	1.90	-	-	0.1821 ± 9e-04	8.35e-01	(481.66, 479.60, 500)	1514.84	-
261.01	96 b	16.24	5.82e-02	6.12	-	-	0.0261 ± 4e-04	3.23e-01	(532.12, 525.82, 500)	153.96	-

KOI	*Kepler*	$P_{\rm orb}$ (day)	$t_{\rm damp}$ (Gyr)	$(R_{\rm out}/R_{\rm p})_{\rm upp,\ Aligned}$	$(R_{\rm out}/R_{\rm p})_{\rm upp,\ Saturn}$	$(R_{\rm out}/R_\star)_{\rm upp}$	$(R_{\rm p}/R_\star)_{\rm ringless}$	p	$(\chi^2_{\rm ringless,min}, \chi^2_{\rm ring,min}, N_{\rm bin})$	(S/N)	Comment
277.01	36 c	16.23	4.68e-02	-	-	-	0.0207 ± 1e-04	9.86e-01	(527.45, 526.75, 500)	139.68	-
279.01	450 b	28.45	1.32e-01	6.63	1.85	0.050	0.0349 ± 2e-04	6.91e-01	(531.31, 528.00, 500)	206.16	-
280.01	-	11.87	2.98e-02	9.31	-	-	0.0194 ± 2e-04	8.24e-01	(527.11, 524.77, 500)	126.35	-
282.01	130 c	27.51	2.56e-01	-	-	-	0.0236 ± 7e-04	3.94e-01	(475.67, 470.66, 500)	111.58	-
304.01	518 b	8.51	1.15e-02	-	-	-	0.0228 ± 2e-04	1.00e+00	(489.96, 490.58, 500)	108.97	-
314.01	138 c	13.78	6.55e-02	-	-	-	0.0249 ± 8e-04	1.00e+00	(448.61, 448.73, 500)	113.40	-
319.01	-	46.15	3.17e-01	9.03	-	-	0.051 ± 9e-03	2.25e-01	(523.15, 515.79, 500)	137.89	-
351.02	90 g	210.60	3.43e+01	-	1.79	0.087	0.0597 ± 4e-04	8.91e-02	(383.31, 374.62, 427)	111.28	-
366.01	-	75.11	4.79e-01	4.14	-	-	0.064 ± 2e-03	5.33e-01	(375.88, 371.57, 367)	172.90	-
367.01	-	31.58	2.35e-01	-	2.01	0.062	0.0422 ± 6e-04	6.63e-01	(284.44, 281.38, 310)	192.72	-
398.01	148 d	51.85	4.65e-01	5.14	-	-	0.100 ± 3e-03	3.18e-01	(493.58, 487.69, 500)	184.33	-
433.01	553 b	4.03	5.57e-04	-	2.11	0.071	0.0478 ± 4e-04	9.36e-01	(494.54, 493.24, 500)	129.83	-
464.01	561 b	58.36	8.60e-01	-	-	-	0.068 ± 1e-03	4.90e-01	(461.90, 457.74, 500)	174.35	-
611.01	-	3.25	1.32e-04	-	-	-	0.11 ± 4e-02	3.84e-01	(413.93, 409.50, 500)	405.50	-
620.01	51 b	45.16	3.75e-01	-	1.73	0.104	0.0725 ± 5e-04	8.62e-01	(525.96, 523.91, 500)	120.00	-
620.02	51 d	130.18	5.87e+00	-	1.45	0.131	0.0985 ± 7e-04	5.02e-01	(288.97, 284.74, 305)	130.48	-
631.01	628 b	15.46	1.39e-02	8.02	-	-	0.0617 ± 8e-04	9.62e-01	(123.10, 121.88, 111)	120.26	-
674.01	643 b	16.34	1.44e-02	-	-	-	0.0369 ± 3e-04	9.16e-01	(454.41, 453.04, 500)	137.26	-
676.02	210 b	2.45	2.53e-04	7.88	-	-	0.0381 ± 6e-04	5.62e-01	(483.27, 479.43, 500)	265.21	-
680.01	435 b	8.60	4.84e-04	2.31	1.89	0.090	0.0630 ± 3e-04	9.78e-01	(504.98, 504.17, 500)	468.57	-
760.01	-	4.96	3.50e-04	9.70	-	-	0.112 ± 3e-03	2.52e-01	(123.17, 117.00, 139)	179.87	-
767.01	670 b	2.82	6.55e-05	2.08	1.67	0.166	0.1200 ± 6e-04	5.49e-01	(451.94, 448.26, 500)	922.58	-
802.01	-	19.62	1.70e-02	4.11	-	-	0.144 ± 1e-03	9.55e-01	(407.32, 406.22, 414)	239.43	-
806.01	30 d	143.21	8.97e+00	-	1.67	0.131	0.0922 ± 8e-04	4.28e-01	(472.50, 467.79, 500)	108.09	-
806.02	30 c	60.32	5.04e-01	6.00	1.71	0.188	0.132 ± 2e-03	6.64e-01	(484.77, 481.58, 500)	305.49	-
824.01	693 b	15.38	1.02e-02	5.75	-	-	0.121 ± 2e-03	5.43e-01	(506.00, 501.84, 500)	122.79	-
834.01	238 e	23.65	5.62e-02	7.56	-	-	0.057 ± 1e-03	3.56e-01	(502.90, 497.27, 500)	162.09	-
841.02	27 c	31.33	1.47e-01	-	-	-	0.066 ± 2e-03	7.20e-01	(502.77, 499.83, 500)	107.50	-
880.02	82 c	51.54	7.77e-01	-	-	-	0.056 ± 2e-03	1.00e+00	(488.24, 488.50, 500)	118.13	-
883.01	-	2.69	5.44e-05	1.64	1.27	0.217	0.1800 ± 8e-04	7.14e-02	(493.31, 483.20, 500)	1462.56	-
884.01	247 c	9.44	7.18e-03	-	-	-	0.0492 ± 4e-04	4.71e-01	(473.11, 468.71, 500)	159.90	-
889.01	75 b	8.88	2.19e-03	7.55	1.59	0.160	0.114 ± 2e-03	4.02e-01	(517.30, 511.93, 500)	329.94	-

KOI	*Kepler*	$P_{\rm orb}$ (day)	$t_{\rm damp}$ (Gyr)	$(R_{\rm out}/R_{\rm p})_{\rm upp,\ Aligned}$	$(R_{\rm out}/R_{\rm p})_{\rm upp,\ Saturn}$	$(R_{\rm out}/R_\star)_{\rm upp}$	$(R_{\rm p}/R_\star)_{\rm ringless}$	p	$(\chi^2_{\rm ringless,min}, \chi^2_{\rm ring,min}, N_{\rm bin})$	(S/N)	Comment
918.01	725 b	39.64	1.66e-01	6.56	1.46	0.151	0.1143 ± 8e-04	5.62e-01	(544.34, 540.01, 500)	373.56	-
959.01	-	12.71	2.50e-02	2.12	1.96	0.260	0.179 ± 1e-03	8.41e-01	(92.72, 89.28, 65)	1216.12	FP
961.01	42 b	1.21	9.26e-05	3.27	-	-	0.0446 ± 3e-04	9.61e-01	(743.83, 742.28, 500)	107.21	-
984.01	-	4.29	1.41e-03	-	-	-	0.031 ± 3e-03	2.26e-01	(995.18, 981.19, 500)	180.30	-
1074.01	762 b	3.77	1.62e-04	4.20	1.44	0.137	0.1043 ± 4e-04	8.08e-02	(568.08, 556.81, 500)	439.51	-
1089.01	418 b	86.68	1.92e+00	-	-	-	0.083 ± 2e-03	7.55e-01	(475.60, 473.04, 500)	145.85	-
1426.02	297 c	74.93	1.98e+00	-	-	-	0.0632 ± 9e-04	6.60e-01	(392.61, 389.30, 395)	119.29	-
1448.01	-	2.49	1.50e-05	1.68	1.27	0.230	0.1894 ± 4e-04	6.96e-01	(657.90, 653.84, 500)	1137.21	FP
1456.01	855 b	7.89	1.93e-03	3.23	-	-	0.0754 ± 6e-04	5.40e-01	(504.84, 500.66, 500)	226.00	-
1474.01	419 b	69.73	8.96e-01	-	-	-	0.0633 ± 7e-04	3.72e-01	(458.00, 452.46, 453)	185.06	-
1478.01	858 b	76.14	2.86e+00	-	1.78	0.070	0.0489 ± 2e-04	2.39e-01	(400.00, 392.79, 382)	122.21	-
1545.01	-	5.91	5.65e-04	4.81	1.50	0.162	0.1212 ± 9e-04	5.52e-01	(506.69, 502.59, 500)	318.66	-
1547.01	-	30.69	6.38e-02	-	-	-	0.126 ± 2e-03	2.09e-01	(166.69, 157.65, 139)	110.46	-
1781.01	411 c	7.83	5.03e-03	5.57	-	-	0.0420 ± 6e-04	7.47e-01	(515.99, 513.16, 500)	173.86	-
1784.01	-	5.01	5.19e-04	8.43	-	-	0.3 ± 4e+01	3.61e-01	(558.13, 551.92, 500)	210.08	FP
6969.01	-	1.79	2.44e-06	1.13	1.02	0.242	0.2368 ± 3e-04	3.13e-01	(527.82, 521.46, 500)	2074.42	FP

Chapter 4

Observational Quest for Alignment of Disk Orientations in Nearby Star-Forming Regions: Orion, Lupus, Taurus, Upper Scorpius, and ρ Ophiuchi

Stars are the fundamental building blocks of the visible universe, and their formation and evolution are among the most important areas of research in astronomy. It is well-known that multiple star formation is commonly observed in star forming regions (e.g. Lada & Lada, 2003), and also that more than half of stars at present with stellar masses larger than the Solar mass form binary systems (e.g. Duchêne & Kraus, 2013). Nevertheless, details of the multiple star formation process are not yet well understood theoretically despite numerous previous efforts (e.g Krumholz, 2014). The star formation directly sets the initial conditions of planet formation and evolution, so the understanding of stellar physics is also important for unveiling the histories of exoplaentary systems as well.

One of the key concepts in star formation is the angular momentum evolution, and one of possible important probes is the alignment among directions of rotations. Previous studies exploit stellar spins to search for the alignment (Jackson & Jeffries, 2010; Corsaro et al., 2017; Jackson et al., 2018; Kovacs, 2018), but the stellar rotations may not be a good proxy of the rotation direction of the disk since the amplitude of the stellar spin is significantly smaller than that of the disk angular momentum, and could be affected more easily by other local processes. For instance, the strong diversity of spin-orbit architecture is well established in exo-planetary systems (e.g. Winn & Fabrycky, 2015). In particular, Kepler-56 is a transiting multi-planetary system exhibiting a significantly oblique stellar spin; Huber et al. (2013) discovered that its stellar inclination angle i_{s} is about 45 degree from the asteroseismic analysis. While it is not clear if the misalignment is of primordial or dynamical origin, this indicates a possibility that the stellar spin and disk rotation axes are significantly different. Furthermore, it would be more difficult to identify directions of stellar spins embedded in disks or envelopes. In addition, the directions of outflows could change from large to small scales, implying that the they might not be good tracers of the stellar spins (Bussmann et al., 2007).

Therefore the physics of star formation may be more likely to be imprinted in the degree of the alignment of proto-planetary disk orientations, rather than that of stellar spins. This is why we attempt the systematic analysis of the axes of spatially resolved disks and their correlations in five near-by star-forming regions; Orion, Lupus, Taurus, Upper Scorpius, and ρ Ophiuchi.

The rest of the chapter is organized as follows. Section 4.1 describes the statistical analysis of the alignment among disks in this chapter. Specifically, we adopt Kuiper's test to check the departure from the uniform distribution of the position angles (PA) of disks. Section 4.2 summarizes our target star-forming regions and their observations, and Section 4.3 presents the main result of the chapter. We perform a sparse modeling estimate of the PA for Lupus region, and compare the PA values against those estimated from CLEAN+`imfit` and `uvmodelfit` in Section 4.4. The details of the sparse modeling are described in Appendix. The implications of the present result are discussed in Section 4.6. Finally, Section 4.7 is devoted to the conclusion.

4.1 Statistical analysis of the position angle and inclination of the disks

Given the projected image of a disk, one can approximate it by an ellipse and estimate its position angle, PA, and inclination, i, relative to our line-of-sight. Specifically, PA refers to the angle of the major axis measured counter-clockwise from the north. Since we assume that the disk is circular in reality, cos i should be equal to the ratio of the minor and major axes of the ellipse; the face-on and edge-on disks correspond to $i = 0^\circ$ and $i = 90^\circ$, respectively. Note we consider the range of PA and i as $0^\circ \leq \mathrm{PA} < 180^\circ$ and $0^\circ \leq i < 90^\circ$ since the ellipse fit alone cannot distinguish between PA and $\mathrm{PA} + 180^\circ$ and between i and $180^\circ - i$. In the case that the additional spectroscopic data are available (for instance the Lupus III below), one can break the degeneracy between PA and $\mathrm{PA} + 180^\circ$ is broken, and estimate PA for $0^\circ \leq \mathrm{PA} < 360^\circ$.

Since the disk inclination may change the detection threshold of the disk, its correlation might suffer from the selection bias; for instance, the observed flux of an optically-thick disk is proportional to $\cos i$, which preferentially increases the fraction of face-one disks with $i \approx 0^\circ$. Thus we mainly use the observed distribution of PA in order to test the possible correlation of the disk orientation. When we identify a signature of correlation in the PA distribution for a particular star-forming region, however, we consider the distribution of i as well to see if it exhibits a similar non-uniformity.

Due to the degeneracy of the value of PA mentioned above, a widely-used statistics to validate the non-uniformity of the distribution, the Kolmogorov-Smirnov test for instance, cannot be applied in a straightforward fashion. Therefore we adopt a statistics proposed by Kuiper (1960), which improves the KS test for variables with rotational invariance. In the present case, the Kuiper test evaluates the difference of the two cumulative distributions using the following statistics:

$$D = \max_{1\leq n\leq N}[F_{\rm ref}(\mathrm{PA}_n) - F_{\rm obs}(\mathrm{PA}_n)] + \max_{1\leq n\leq N}[F_{\rm obs}(\mathrm{PA}_n) - F_{\rm ref}(\mathrm{PA}_n)], \tag{4.1}$$

where PA_n denotes the position angle of the n-th disk ($1 \leq n \leq N$), $F_{\rm ref}$ is the reference cumulative distribution, and $F_{\rm obs}$ is the empirical cumulative distribution of the observed data.

If we take the reference distribution to be uniform, the non-uniformity can be evaluated from the observed value of $D_{\rm obs}$; specifically, the large value of $D_{\rm obs}$ implies the larger non-uniformity. Assuming that the the observed distribution is also sampled from the uniform distribution, we can compute the expected distribution for D in the form of $p_{\rm null}(D)$. Then, we can test the non-uniformity of the observed distribution by investigating whether $D_{\rm obs}$ is consistent with $p_{\rm null}(D)$ or not.

In the Kuiper test, we define p-value as the probability that the value of D for $p_{\rm null}(D)$ is larger than the observed $D_{\rm obs}$; $p \simeq 0.05$ roughly corresponds to 2σ-significance, and $p \simeq 0.003$ to 3σ-significance. In computing p-value, we employ `astropy` that adopts the formulae in Stephens (1965) and Paltani (2004).

The estimation of mean and standard deviation of PA with rotational symmetry, $\overline{\mathrm{PA}}$ and $\sigma_{\rm PA}$, is a bit tricky, and we adopt the following estimators (Mardia & Jupp, 2009). For those disks with $0° \leq \mathrm{PA} < 180°$, we first define $\theta = 2\mathrm{PA}$, and then compute

$$x_{\rm mean} = \frac{1}{N}\sum_{i=1}^{N}\cos\theta_i, \quad y_{\rm mean} = \frac{1}{N}\sum_{i=1}^{N}\sin\theta_i. \tag{4.2}$$

Converting $(x_{\rm mean}, y_{\rm mean})$ into the polar coordinates $(r_{\rm mean}, \theta_{\rm mean})$, we obtain

$$\overline{\mathrm{PA}} = \frac{1}{2}\theta_{\rm mean}, \quad \sigma_{\rm PA} = \frac{1}{2}\sqrt{-2\log r_{\rm mean}}. \tag{4.3}$$

For the Lupus III with with $0° \leq \mathrm{PA} < 360°$ (Yen et al., 2018), we simply set $\theta =$PA, and use equation (4.3) without the factor 1/2.

4.2 Targets and data

For our analysis of the correlation of the disk orientations, we select five nearby star-forming regions associated with many resolved disks; Orion Nebular Cluster (ONC) (Bally et al., 2000; Eisner et al., 2018), the Lupus star forming region (Bally et al., 2000; Ansdell et al., 2016; Tazzari et al., 2017; Yen et al., 2018), the Taurus Molecular Cloud (TMC) (Kitamura et al., 2002; Andrews & Williams, 2007; Isella et al., 2009; Guilloteau et al., 2011), the Upper Scorpius OB Association (Barenfeld et al., 2016, 2017), and the ρ Ophiuchi cloud complex (Cox et al., 2017; Cieza et al., 2019). The basic properties of those targets are summarized in Table 4.1, and their angular distribution on the sky is plotted in Figure 4.1.

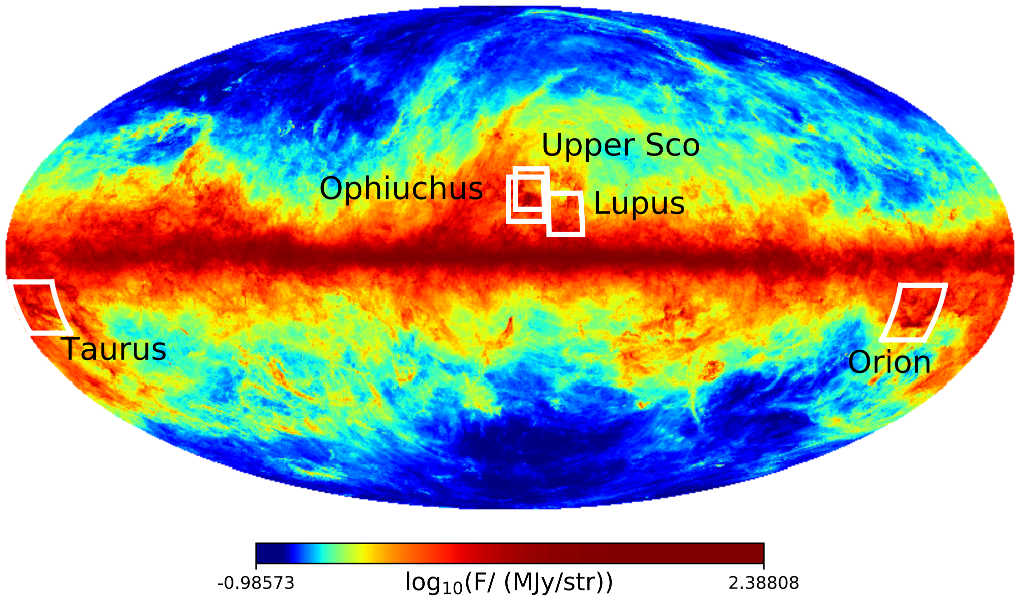

Figure 4.1 Map of the five star-forming regions analyzed in this chapter overlaid on the thermal dust emission at 353 GHz (Planck Collaboration et al., 2016b).

All the five regions are observed in the radio band, in particular with ALMA. Unfortunately, the ALMA data for ONC are largely contaminated by phase errors, so it is difficult to present the robust discussion on the alignment. For this reason, we mainly use the data presented by HST (Hubble Space Telescope) in the optical band for ONC (Bally et al., 2000). Further details of the five star-forming regions are described below in Section 4.2.5-4.2.4. Table 4.6-4.5 summarize the disk parameters.

Table 4.1 Parameters of disks in the Lupus region (Yen et al., 2018).

Field	# Disk	Field Size / Resolution	Wavelength	p (Kuiper's test)	Mean(PA) ± σ(PA)	Ref [a]
Lupus	37	7° / 0.3″	Radio/ALMA	0.29	31.8° ± 114.4° [a]	1
- Lupus III	16/37	0.5° / 0.3″	Radio/ALMA	0.037	77.3° ± 69.9° [a]	1
- Outside the Lupus III	21/37	7° / 0.3″	Radio/ALMA	0.30	298.6° ± 94.3° [a]	1
Taurus	45	15° / 0.4–1″	Radio	0.69	31.7° ± 58.6°	2–5
Upper Scorpius	16	8° / 0.37″	Radio/ALMA	0.16	14.6° ± 39.9°	6
Ophiuchus	49	3° / 0.2″	Radio/ALMA	0.68	165.5°± 59.1°	7,8
- L1688	31/49	0.5° / 0.2″	Radio/ALMA	0.95	156.4°± 59.4°	7,8
ONC	31	6′ / 0.1″	Optical/HST	0.47	21.3° ± 55.9°	9

Notes

[a] The range of PA is [0, 360°) in Yen et al. (2018).

[Ref] (1) Yen et al. (2018) (2) Kitamura et al. (2002); (3) Andrews & Williams (2007); (4) Isella et al. (2009); (5) Guilloteau et al. (2011); (6) Barenfeld et al. (2017); (7) Cox et al. (2017); (8) Cieza et al. (2019); (9) Bally et al. (2000)

4.2.1 Lupus

The Lupus clouds are a young (1-2 Myr) and nearby (150-200 pc) star-forming region (Comerón (2008) and references therein). Using ALMA, Ansdell et al. (2016) conducted a systematic survey for radio emission from 89 disks identified by previous literature (Hughes et al., 1994; Comerón, 2008; Merín et al., 2008; Mortier et al., 2011). Instead of using the image from continuum data, Yen et al. (2018) stacked the observed CO line emission from the region alone, and they were able to determine the disk rotation direction spectroscopically. Therefore they broke the degeneracy of the direction of PA, and obtained the estimate in the range of $0^\circ \leq \mathrm{PA} < 360^\circ$. In the current analysis, we adopt PA estimated by Yen et al. (2018).

Interestingly we notice significant clustering of stars inside the the Lupus III cloud. With the parallaxes from Gaia Data Release 2 (Gaia Collaboration et al., 2018), we are able to identify stars located in the Lupus III three-dimensionally. Once the distance to each star, d, is given, its location in the equatorial coordinate system is written as

$$(x, y, z) = (d \cos\alpha \cos\delta, d \sin\alpha \cos\delta, d \sin\delta) \tag{4.4}$$

where α and δ are the right ascension, and the declination of the star. Then, we find that the three-dimensional region of the Lupus III is localized in $-60 < x$ (pc) < -56, $-114 < y$ (pc) < -106 as shown in Figure 4.2. The maximum distance among stars in the Lupus III is roughly 10 pc from us. In the analysis, we exclude systems without Gaia parallaxes: J16011549-4152351, J16070384-3911113, J160934.2-391513, and J16093928-3904316. In total, our analysis uses 16 disks in the Lupus III, and 21 disks outside the Lupus III, and the typical errors of their PA are less than 10°.

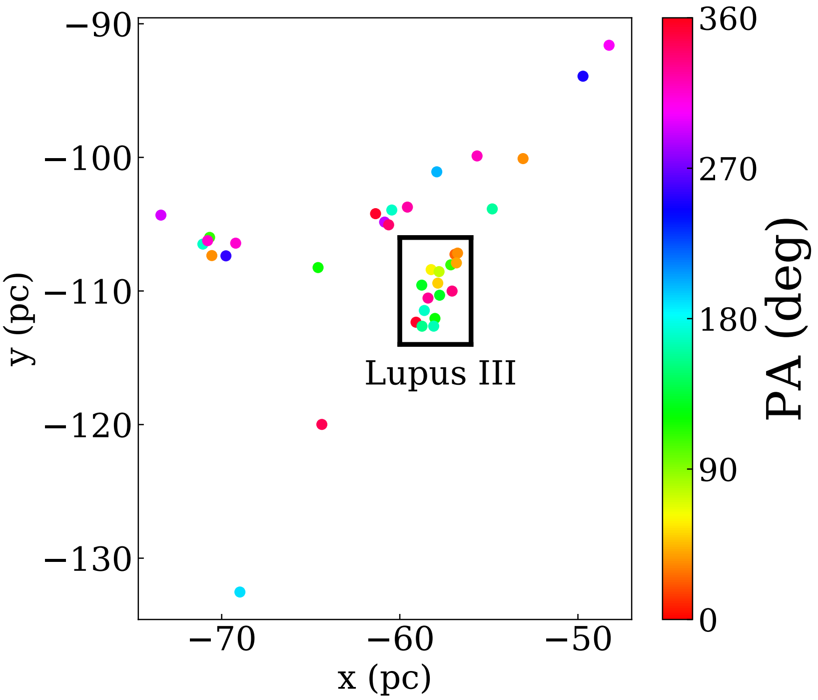

Figure 4.2 Distribution of disks in the Lupus cloud projected on the x-y plane in the equatorial coordinate system. The circles are color-coded according to PA.

4.2.2 The Taurus Molecular Cloud

The Taurus Molecular Cloud is a nearby low-mass star-forming region located at 140 pc away, and the typical stellar ages are estimated to be 1-10 Myr; Kenyon et al. (2008) and references therein. We compile the values of PA published in previous literature (Kitamura et al., 2002; Andrews & Williams, 2007; Isella et al., 2009; Guilloteau et al., 2011). When more than one estimates are given to the same object, we choose one from the latest literature. When different values are available for the same system, we decide to adopt the value from the most recent literature. In total, we consider 45 disks in the Taurus region and the errors of their PA values are typically less than 10°.

4.2.3 The Upper Scorpius OB Association

Upper Scorpius OB Association is a population of stars with the age of 5-11 Myr (Preibisch et al., 2002; Pecaut et al., 2012) located at 145 pc away ; Preibisch et al. (2002) and references therein. Unlike the other four regions that we consider in this chapter, the molecular gas in the region is already dispersed. Out of 106 possible disk-bearing stars identified by infrared observations (Carpenter et al., 2006; Luhman & Mamajek, 2012), Barenfeld et al. (2016) detected radio emission from 57 systems using ALMA. In the current analysis, we adopt PA estimated by Barenfeld et al. (2017), which presents disk parameters in their Table 1. Unfortunately the majority of disks are not well resolved spatially, and we select 16 stellar systems whose errors of PA are less than $\sim 30^\circ$.

4.2.4 The ρ Ophiuchi cloud complex

The ρ Ophiuchi cloud complex is one of the closest star-forming region located at $\sim$ 137 pc away (Ortiz-León et al., 2017), with the stellar age being within 0.5 - 2 Myr (Wilking et al., 2008). In the region, we are particularly interested in the dense cloud L1688 ($246.2^\circ < \alpha < 247.2^\circ$, $-24.8^\circ < \delta < -24^\circ$) with plenty of resolved disks to look for the possible alignment of their orientations.

This region was surveyed independently by Cox et al. (2017) and Cieza et al. (2019), which we combine in the analysis; Cox et al. (2017) conducted a survey for radio emission from 49 stellar systems with infrared excesses identified by Evans et al. (2003), and found 46 resolved disks using ALMA. The angular resolution of the survey is about $0.2''$, roughly corresponding to 30 au. We adopt the values of PA listed in their Table 4. More recently, Cieza et al. (2019) obtained continuum images of 147 systems identified by Evans et al. (2009) at $0.2''$ resolution. Among the 147 observed systems, they were able to spatially resolve 59 disks.

We compile the PA of all the disks identified by the two surveys, but exclude those within $i = 0^\circ$ within 1σ or with PA errors exceeding 30° in the analysis below. The combined list include 51 disks in total, and 17 disks out of them have measured PAs both by the two studies. The mean and standard deviation of their difference, ΔPA, are -2.3° and 24.0°, respectively, implying no significant bias between the two measurements. There are two disks with large difference $|\Delta\mathrm{PA}| \simeq 50^\circ$ between the two observations, so we also exclude them from this analysis. For the robust analysis, we try two different combinations in the analysis; one uses Cox et al. (2017) and the other uses Cieza et al. (2019) for the overlapped disks. Finally, our sample contains 49 disks in the entire field of the ρ Ophiuchi cloud complex, out of which 31 systems are located in the cloud L1688.

4.2.5 Orion Nebular Cluster

The Orion Nebular Cluster (ONC) is one of the closest young stellar clusters embedded in the Orion Nebular. The parent cloud of the Orion Nebular, Orion A, is approximately one order of magnitude larger than ONC in size. ONC is located at $\sim$ 400 pc away, and the age is estimated as 2 Myr (Reggiani et al., 2011).

Our analysis of the ONC is based on the optical survey by Bally et al. (2000) that detected 31 disks in the ONC from the narrow-band images of the Orion Nebular with WFPC2 (Wide Field and Planetary Camera 2) on HST. We use the values of PA listed in their Tables 1 and 2. There is also an observation of ONC by ALMA (Eisner et al., 2018), but it turns out that it is challenging to correctly determine the disk orientations due to large phase errors in the observation. We discuss this issue further in Sec 4.5.

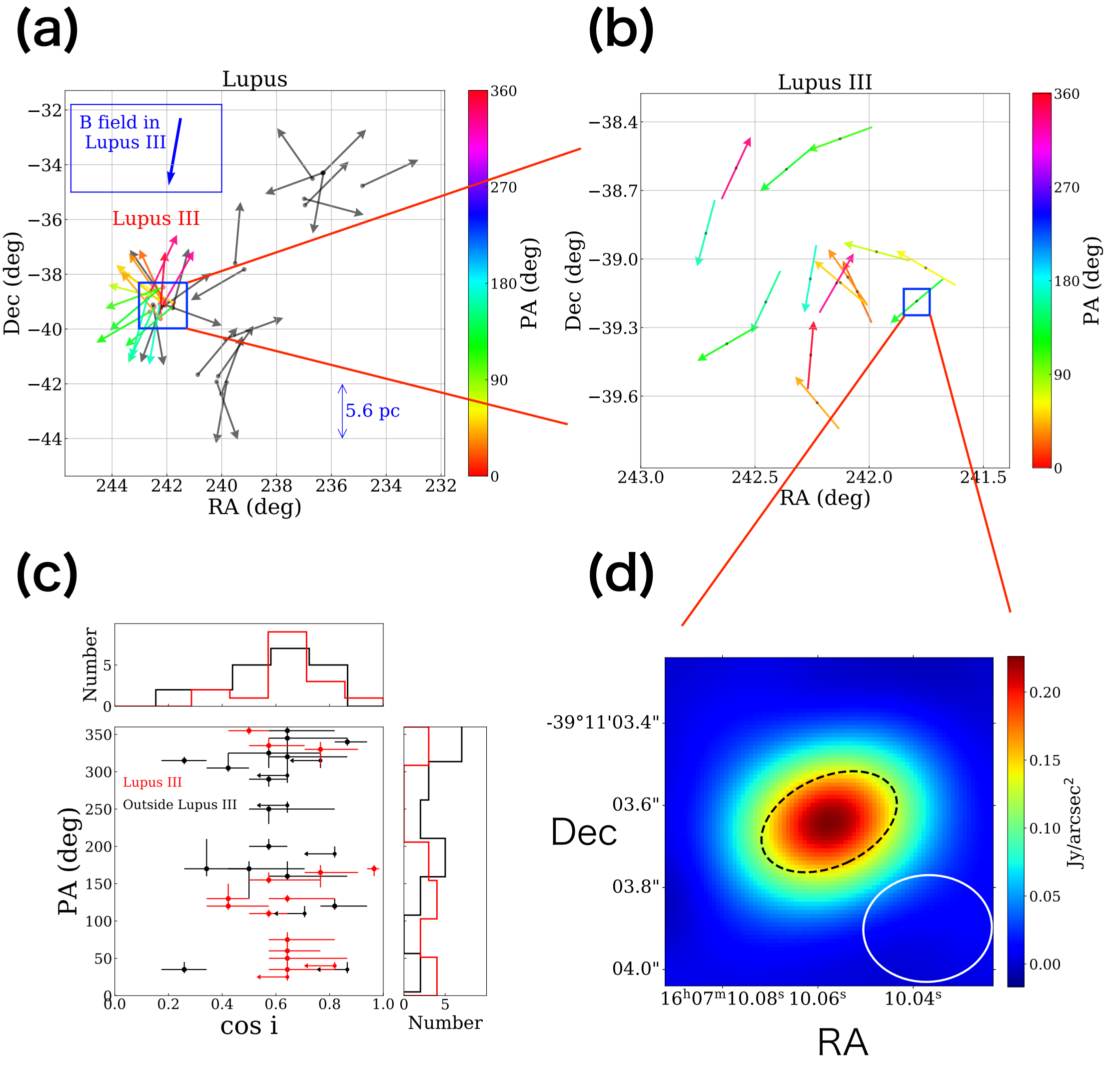

Figure 4.3 Distribution of disk orientations in Lupus. We use measurement in Yen et al. (2018). (a) Directions of disk rotations in field. The arrows represent the directions of major axes of disks (strictly, the direction from the blue- to red-shifted emission due to the Keplerian motion.). As for the disks in the Lupus III, we express PA using color arrows. The blue square border is the Lupus III shown in panel (b). (b) Zoom-up view of 16 disks (black) in the Lupus III, whose region is determined by Gaia DR2 data. c) Distribution of PA and cos i of 37 disks measured by Yen et al. (2018). (d) Example of a continuous image, corresponding to the spectroscopic observation, for a disk around Sz 90. The image is convolved with the beam patten, and it is produced by CLEAN in this study. The lower left white ellipse shows the beam size, and the dotted ellipse in the center represents the estimated size of the disk deconvolved from the beam.

Table 4.2 Parameters of disks in the Lupus region (Yen et al., 2018).

Name	RA (deg)	Dec (deg)	PA (deg)	i (deg)	x (pc)	y (pc)	z (pc)	In Lupus III?
Sz 65	234.86565	-34.77154	295^{+20}_{-10}	< 50	-73.4	-104.3	-88.6	No
J15450887-3417333	236.28690	-34.29272	170^{+10}_{-40}	60^{+5}_{-15}	-71.1	-106.5	-87.3	No
Sz 68	236.30354	-34.29194	110^{+10}_{-5}	< 45	-70.7	-106.0	-86.9	No
Sz 69	236.32247	-34.30795	315^{+10}_{-10}	< 40	-70.8	-106.2	-87.1	No
Sz 71	236.68630	-34.51001	35^{+10}_{-5}	< 30	-70.6	-107.4	-88.3	No
Sz 72	236.96088	-35.47660	315^{+5}_{-5}	75^{+5}_{-5}	-69.2	-106.4	-90.5	No
Sz 73	236.98719	-35.24310	255^{+5}_{-10}	< 50	-69.8	-107.4	-90.5	No
Sz 83	239.17623	-37.82106	120^{+10}_{-5}	35^{+5}_{-15}	-64.6	-108.2	-97.9	No
Sz 84	239.51043	-37.60086	355^{+5}_{-5}	50^{+5}_{-15}	-61.4	-104.2	-93.1	No
Sz 129	239.81857	-41.95296	170^{+40}_{-10}	70^{+5}_{-10}	-60.5	-103.9	-108.1	No
RY Lup	239.86822	-40.36433	290^{+5}_{-10}	55^{+5}_{-5}	-60.9	-104.8	-103.0	No
J16000236-4222145	240.00976	-42.37082	340^{+5}_{-5}	30^{+5}_{-10}	-60.6	-105.1	-110.6	No
Sz 130	240.12926	-41.72704	325^{+10}_{-20}	55^{+10}_{-15}	-59.6	-103.7	-106.7	No
MY Lup	240.18543	-41.92536	200^{+10}_{-5}	55^{+5}_{-5}	-57.9	-101.1	-104.6	No
Sz 133	240.87239	-41.66727	320^{+10}_{-5}	50^{+5}_{-20}	-55.7	-99.9	-101.8	No
Sz 88A	241.75244	-39.03885	60^{+5}_{-10}	50^{+5}_{-10}	-58.2	-108.4	-99.8	Yes
J16070854-3914075	241.78558	-39.23552	345^{+10}_{-20}	50^{+5}_{-20}	-64.4	-120.0	-111.2	No
Sz 90	241.79190	-39.18435	130^{+5}_{-5}	50^{+5}_{-15}	-58.8	-109.6	-101.3	Yes
Sz 95	241.96790	-38.96846	75^{+10}_{-10}	50^{+5}_{-15}	-57.8	-108.6	-99.5	Yes
Sz 96	242.05257	-39.14273	25^{+5}_{-5}	< 50	-56.9	-107.3	-98.8	Yes
J16081497-3857145	242.06234	-38.95412	35^{+10}_{-5}	75^{+5}_{-5}	-53.1	-100.1	-91.6	No
Sz 98	242.09367	-39.07967	35^{+10}_{-5}	50^{+5}_{-15}	-56.8	-107.2	-98.5	Yes
Sz 100	242.10729	-39.10044	250^{+5}_{-20}	55^{+5}_{-20}	-49.7	-93.9	-86.4	No
Sz 103	242.12607	-39.10320	50^{+5}_{-10}	50^{+5}_{-20}	-57.9	-109.4	-100.6	Yes
J16083070-3828268	242.12786	-38.47423	110^{+5}_{-5}	55^{+5}_{-5}	-57.1	-108.0	-97.1	Yes
V856 Sco	242.14281	-39.10519	330^{+10}_{-20}	40^{+5}_{-15}	-58.4	-110.5	-101.6	Yes
Sz 108B	242.17802	-39.10520	160^{+20}_{-5}	50^{+5}_{-20}	-54.8	-103.9	-95.5	No
J16085373-3914367	242.22384	-39.24365	305^{+20}_{-5}	65^{+5}_{-5}	-48.3	-91.6	-84.6	No
Sz 111	242.22780	-39.62875	40^{+5}_{-5}	< 35	-56.8	-107.9	-101.0	Yes
J16090141-3925119	242.25584	-39.42008	355^{+5}_{-5}	60^{+5}_{-5}	-59.1	-112.3	-104.3	Yes
Sz 114	242.25765	-39.08689	170^{+5}_{-10}	15^{+5}_{-5}	-58.6	-111.5	-102.3	Yes
J16092697-3836269	242.36236	-38.60758	130^{+20}_{-10}	65^{+5}_{-5}	-57.8	-110.3	-99.4	Yes
Sz 118	242.45268	-39.18811	155^{+10}_{-5}	55^{+5}_{-15}	-58.8	-112.6	-103.6	Yes
J16100133-3906449	242.50549	-39.11255	190^{+10}_{-5}	< 35	-69.0	-132.5	-121.5	No
J16101984-3836065	242.58259	-38.60194	335^{+10}_{-5}	55^{+5}_{-10}	-57.1	-110.0	-98.9	Yes
J16102955-3922144	242.62308	-39.37079	120^{+10}_{-5}	65^{+5}_{-10}	-58.0	-112.1	-103.5	Yes
Sz 123A	242.71489	-38.88726	165^{+10}_{-20}	40^{+5}_{-15}	-58.1	-112.6	-102.2	Yes

Table 4.3 Summary of star-forming regions along with analyses of alignment

Name	RA (deg)	Dec (deg)	PA (deg)	cos$i$	r_{disk} (arcsec)	Ref[a]
04158+2805	64.743	28.474	88.0 ± 5.0	0.60 ± 0.13	3.10 ± 0.35	2
AA Tau	68.731	24.481	94.0 ± 9.0	0.36 ± 0.19	0.55 ± 0.10	2
BP Tau	64.816	29.107	10.0 ± 2.0	0.68 ± 0.02	0.25 ± 0.01	4
CI Tau	68.467	22.842	14.0 ± 1.0	0.64 ± 0.02	0.37 ± 0.01	4
CQ Tau	83.994	24.748	31.0 ± 8.0	0.73 ± 0.06	0.43 ± 0.02	4
CY Tau	64.391	28.346	165.0 ± 4.0	0.85 ± 0.02	0.28 ± 0.01	4
DG Tau	66.770	26.104	179.0 ± 3.0	0.82 ± 0.02	0.28 ± 0.01	4
DG Tau b	66.761	26.092	26.0 ± 2.0	0.49 ± 0.04	0.34 ± 0.01	4
DL Tau	68.413	25.344	29.0 ± 2.0	0.79 ± 0.02	0.35 ± 0.01	4
DM Tau	68.453	18.169	144.0 ± 9.0	0.90 ± 0.03	0.25 ± 0.01	4
DN Tau	68.864	24.250	86.0	0.78	0.34	3
DO Tau	69.619	26.180	67.0 ± 9.0	0.79 ± 0.08	1.01 ± 0.05	1
DQ Tau	71.721	17.000	156.0 ± 6.0	0.71 ± 0.05	0.12 ± 0.01	4
DR Tau	71.776	16.979	108.0	0.81	0.24	3
FT Tau	65.913	24.937	121.0 ± 8.0	0.93 ± 0.03	0.21 ± 0.01	4
GM Aur	73.796	30.366	57.0 ± 4.0	0.54 ± 0.05	0.53 ± 0.03	4
GO Tau	70.763	25.339	107.0	0.80	0.43	3
HH 30	67.906	18.207	125.0 ± 0.0	0.15 ± 0.02	0.71 ± 0.01	4
HL Tau	67.910	18.233	135.0 ± 2.0	0.74 ± 0.01	0.43 ± 0.01	4
Haro 6-10 N	67.349	24.550	53.0 ± 18.0	0.38 ± 0.30	0.12 ± 0.06	4
Haro 6-10 S	67.349	24.550	178.0 ± 8.0	0.30 ± 0.19	0.18 ± 0.03	4
Haro 6-13	68.064	24.483	179.0 ± 10.0	0.69 ± 0.09	0.26 ± 0.01	4
Haro 6-33	70.412	25.941	31.0 ± 28.0	0.79 ± 0.20	0.28 ± 0.06	4
Haro 6-5B	65.503	26.441	155.0 ± 8.0	0.56 ± 0.17	3.40 ± 0.51	1
IQ Tau	67.465	26.112	41.0 ± 6.0	0.53 ± 0.10	1.54 ± 0.11	1
LkCa 15	69.824	22.351	65.0 ± 6.0	0.76 ± 0.04	0.60 ± 0.02	4
LkCa15	69.824	22.351	65.0 ± 6.0	0.76 ± 0.04	0.60 ± 0.02	4
MWC 480	74.693	29.844	22.0 ± 3.0	0.82 ± 0.02	0.34 ± 0.01	4
MWC 758	82.615	25.333	168.0 ± 22.0	0.82 ± 0.12	0.50 ± 0.04	4
RY Tau	65.489	28.443	23.0	0.60	0.32	3
T Tau	65.498	19.535	4.0 ± 17.0	0.71 ± 0.15	0.24 ± 0.03	4
UZ Tau E	68.178	25.875	91.0 ± 2.0	0.60 ± 0.02	0.38 ± 0.01	4
UZ Tau W	68.179	25.875	145.0 ± 24.0	0.82 ± 0.11	0.20 ± 0.02	4

Notes

[a] References that we used for the analysis: 1. Kitamura et al. (2002), 2. Andrews & Williams (2007), 3. Isella et al. (2009), 4. Guilloteau et al. (2011).

Table 4.4 Parameters of disks in the Upper Scorpius (Barenfeld et al., 2017).

Name	RA (deg)	Dec (deg)	PA (deg)	i (deg)	$r_{\rm disk}$ (arcsec)
2MASS J15534211-2049282	238.42546	-20.81745	73^{+5}_{-6}	89^{+1}_{-2}	$0.32^{+0.15}_{-0.05}$
2MASS J16014086-2258103	240.42025	-22.96695	26^{+22}_{-23}	74^{+10}_{-31}	$0.26^{+0.06}_{-0.06}$
2MASS J16020757-2257467	240.53154	-22.95130	80^{+17}_{-15}	57^{+14}_{-19}	$0.34^{+0.06}_{-0.05}$
2MASS J16024152-2138245	240.67300	-21.63401	63^{+28}_{-21}	41^{+14}_{-21}	$0.17^{+0.02}_{-0.02}$
2MASS J16035767-2031055	240.99029	-20.51682	5^{+22}_{-26}	69^{+21}_{-27}	$0.82^{+0.63}_{-0.33}$
2MASS J16054540-2023088	241.43917	-20.38358	10^{+36}_{-10}	67^{+9}_{-29}	$0.14^{+0.04}_{-0.01}$
2MASS J16072625-2432079	241.85938	-24.53355	2^{+19}_{-14}	43^{+10}_{-17}	$0.21^{+0.01}_{-0.01}$
2MASS J16075796-2040087	241.99150	-20.66691	0^{+15}_{-14}	47^{+8}_{-14}	$0.08^{+0.01}_{-0.01}$
2MASS J16081566-2222199	242.06525	-22.36722	173^{+24}_{-18}	86^{+4}_{-26}	$0.57^{+0.42}_{-0.29}$
2MASS J16082324-1930009	242.09683	-19.50003	123^{+3}_{-2}	74^{+5}_{-4}	$0.46^{+0.04}_{-0.04}$
2MASS J16090075-1908526	242.25313	-19.13479	149^{+9}_{-9}	56^{+5}_{-5}	$0.41^{+0.04}_{-0.03}$
2MASS J16123916-1859284	243.16317	-18.98412	46^{+22}_{-27}	51^{+14}_{-36}	$0.34^{+0.06}_{-0.05}$
2MASS J16142029-1906481	243.58454	-19.10134	19^{+32}_{-19}	27^{+10}_{-23}	$0.21^{+0.01}_{-0.01}$
2MASS J16153456-2242421	243.89400	-22.70117	170^{+10}_{-31}	46^{+12}_{-21}	$0.15^{+0.01}_{-0.01}$
2MASS J16163345-2521505	244.13938	-25.35140	64^{+9}_{-9}	88^{+2}_{-9}	$0.51^{+0.18}_{-0.16}$
2MASS J16270942-2148457	246.78925	-21.80127	176^{+25}_{-29}	70^{+15}_{-33}	$0.16^{+0.07}_{-0.04}$

Table 4.5 Parameters of disks in the Ophiuchus region (Cox et al. (2017) and Cieza et al. (2019))

Name	RA (deg)	Dec (deg)	$\mathrm{PA}_{\mathrm{cox}}$ (deg) ^{a}	$\mathrm{PA}_{\mathrm{cieza}}$ (deg) ^{a}	$\cos i$ ^{b}	r_{disk} (arcsec) ^{b}	In L1688?
2MASS J16213192-2301403	245.38301	-23.02799	164.0 ± 6.6	···	0.363 ± 0.168	0.097 ± 0.007	No
2MASS J16214513-2342316 (ODISEA_C4_003)	245.43801	-23.70894	174.3 ± 1.0	174.2 ± 1.0	0.188 ± 0.024	0.314 ± 0.016	No
2MASS J16233609-2402209	245.90047	-24.03923	6.7 ± 6.5	···	0.450 ± 0.107	0.080 ± 0.007	No
2MASS J16313124-2426281 (ODISEA_C4_126)	247.88019	-24.44123	49.0 ± 0.2	56.0 ± 10.0	0.121 ± 0.005	0.650 ± 0.015	No
2MASS J16314457-2402129	247.93574	-24.03708	133.8 ± 8.9	···	0.627 ± 0.133	0.055 ± 0.004	No
2MASS J16335560-2442049AB	248.48171	-24.70149	77.0 ± 15.0	···	0.688 ± 0.123	0.335 ± 0.042	No
DoAr 25 (ODISEA_C4_039)	246.59867	-24.72064	110.0 ± 1.4	93.7 ± 0.2	0.455 ± 0.021	0.535 ± 0.019	Yes
DoAr 33	246.91252	-23.97199	78.2 ± 5.6	···	0.782 ± 0.030	0.113 ± 0.003	No
DoAr 43a	247.87864	-24.41119	38.3 ± 1.6	···	0.412 ± 0.026	0.134 ± 0.004	No
EM* SR 13Aab	247.18861	-24.47204	90.0 ± 27.0	···	0.799 ± 0.113	0.206 ± 0.020	Yes
GSS 31a (ODISEA_C4_037A)	246.59734	-24.35000	169.0 ± 5.0	163.0 ± 18.0	0.600 ± 0.074	0.050 ± 0.002	Yes
GSS 31b	246.59763	-24.35049	147.0 ± 15.0	···	0.718 ± 0.120	0.035 ± 0.002	Yes
GY 211 (ODISEA_C4_070)	246.78790	-24.56909	33.1 ± 1.2	36.1 ± 2.6	0.479 ± 0.018	0.133 ± 0.003	Yes
GY 224	246.79653	-24.67975	92.2 ± 0.8	···	0.346 ± 0.014	0.214 ± 0.004	Yes
GY 235 (ODISEA_C4_075)	246.80755	-24.72557	177.0 ± 13.0	28.8 ± 7.0	0.827 ± 0.062	0.104 ± 0.005	Yes
GY 314 (ODISEA_C4_104)	246.91426	-24.65443	138.9 ± 2.1	103.7 ± 2.3	0.562 ± 0.026	0.129 ± 0.003	Yes
GY 33 (ODISEA_C4_043)	246.61475	-24.69830	160.5 ± 1.7	158.9 ± 1.7	0.288 ± 0.043	0.169 ± 0.006	Yes
Haro 1-17	248.09137	-24.70422	79.0 ± 12.0	···	0.474 ± 0.179	0.068 ± 0.008	No
IRAS 16201-2410	245.78841	-24.28482	81.4 ± 8.2	···	0.621 ± 0.086	0.228 ± 0.021	No
IRS 63 (ODISEA_C4_130)	247.89858	-24.02497	150.0 ± 5.2	147.1 ± 0.1	0.689 ± 0.047	0.261 ± 0.012	No
L1689-IRS 7B	248.08671	-24.50819	156.0 ± 28.0	···	0.600 ± 0.355	0.055 ± 0.007	No
LDN 1689 IRS 5Bb	247.96631	-24.93816	117.0 ± 17.0	···	0.364 ± 0.295	0.065 ± 0.013	No
SR 20 W (ODISEA_C4_116)	247.09724	-24.37807	65.7 ± 1.7	56.0 ± 5.0	0.345 ± 0.032	0.210 ± 0.011	Yes
SR 24b (ODISEA_C4_062)	246.74377	-24.76034	22.5 ± 8.3	47.5 ± 3.6	0.572 ± 0.099	0.492 ± 0.059	Yes
V935 Sco (ODISEA_C4_005)	245.57718	-23.36349	80.5 ± 4.7	108.7 ± 0.3	0.581 ± 0.051	0.107 ± 0.005	No
WL6	246.84080	-24.49828	16.0 ± 28.0	···	0.679 ± 0.282	0.053 ± 0.009	Yes
WSB 38B	246.69345	-24.20012	108.0 ± 14.0	···	0.384 ± 0.240	0.043 ± 0.006	Yes
WSB 60 (ODISEA_C4_114)	247.06876	-24.61624	135.0 ± 27.0	135.5 ± 5.8	0.924 ± 0.063	0.277 ± 0.013	Yes
WSB 63	247.22530	-24.79575	0.1 ± 1.3	···	0.402 ± 0.024	0.133 ± 0.003	No
WSB 67 (ODISEA_C4_121)	247.59749	-24.90459	12.8 ± 8.4	22.3 ± 13.5	0.640 ± 0.084	0.087 ± 0.005	No
WSB 82 (ODISEA_C4_143)	249.93933	-24.03451	171.6 ± 2.2	172.3 ± 0.7	0.486 ± 0.030	0.650 ± 0.029	No
YLW 52a	246.96582	-24.52946	129.0 ± 17.0	···	0.491 ± 0.321	0.108 ± 0.021	Yes
2MASS J16250692-2350502 (ODISEA_C4_017)	246.27878	-23.84745	···	173.8 ± 1.3	0.299 ± 0.175	0.117 ± 0.015	No
2MASS J16253673-2415424 (ODISEA_C4_021)	246.40305	-24.26194	···	14.2 ± 0.0	0.269 ± 0.018	0.087 ± 0.002	Yes
2MASS J16253812-2422362 (ODISEA_C4_022A)	246.40880	-24.37697	···	15.8 ± 2.4	0.792 ± 0.019	0.544 ± 0.009	Yes
2MASS J16254662-2423361 (ODISEA_C4_026)	246.44430	-24.39348	···	107.2 ± 0.4	0.271 ± 0.010	0.361 ± 0.005	Yes
2MASS J16261722-2423453 (ODISEA_C4_033)	246.57180	-24.39605	···	71.7 ± 0.4	0.219 ± 0.022	0.104 ± 0.001	Yes
ISO-Oph 37 (ODISEA_C4_038)	246.59823	-24.41111	···	48.3 ± 0.9	0.323 ± 0.002	0.362 ± 0.001	Yes
(GY92) 30 (ODISEA_C4_042)	246.60614	-24.38385	···	160.3 ± 0.3	0.743 ± 0.040	0.112 ± 0.001	Yes
2MASS J16263778-2423007 (ODISEA_C4_046)	246.65744	-24.38365	···	100.5 ± 7.8	0.842 ± 0.016	0.223 ± 0.002	Yes
2MASS J16264046-2427144 (ODISEA_C4_047)	246.66862	-24.45416	···	155.7 ± 1.1	0.833 ± 0.008	0.409 ± 0.002	Yes
2MASS J16264285-2420299 (ODISEA_C4_050A)	246.67850	-24.34179	···	149.8 ± 9.8	0.501 ± 0.180	0.058 ± 0.006	Yes
2MASS J16264502-2423077 (ODISEA_C4_051)	246.68759	-24.38563	···	118.9 ± 4.0	0.623 ± 0.003	0.419 ± 0.001	Yes
2MASS J16265197-2430394 (ODISEA_C4_056)	246.71651	-24.51112	···	38.0 ± 1.5	0.341 ± 0.052	0.379 ± 0.019	Yes
2MASS J16265677-2413515 (ODISEA_C4_060)	246.73653	-24.23111	···	50.8 ± 0.5	0.444 ± 0.044	0.124 ± 0.005	Yes
2MASS J16270524-2436297 (ODISEA_C4_067)	246.77188	-24.60839	···	168.4 ± 0.9	0.332 ± 0.022	0.204 ± 0.003	Yes
2MASS J16270677-2438149 (ODISEA_C4_068)	246.77819	-24.63764	···	14.2 ± 0.9	0.253 ± 0.043	0.117 ± 0.004	Yes
2MASS J16271838-2439146 (ODISEA_C4_083)	246.82655	-24.65423	···	46.5 ± 0.6	0.100 ± 0.017	0.260 ± 0.002	Yes
2MASS J16273982-2443150 (ODISEA_C4_105A)	246.91590	-24.72098	···	118.6 ± 1.6	0.713 ± 0.026	0.095 ± 0.002	Yes

Notes

[a] $\mathrm{PA}_{\mathrm{cox}}$ is posion angle from Cox et al. (2017), and $\mathrm{PA}_{\mathrm{cox}}$ is from Cieza et al. (2019).

[b] Basically, we list values in Cox et al. (2017). If the values in Cox et al. (2017) are not available, we use values in Cieza et al. (2019).

Table 4.6 Parameters of disks or jets in Bally et al. (2000).

Name	RA (deg)	Dec (deg)	PA (deg)	cos$i$	$r_{\rm disk}$ (arcsec) [b]
072-135[a]	83.78004	-5.35958	108.0	···	···
109-327[a]	83.79558	-5.39072	160.0	···	···
114-426	83.79729	-5.40733	29.0	0.26	1.35
117-352[a]	83.79887	-5.39772	50.0	···	···
121-1925	83.80042	-5.32361	118.0	0.62	0.40
132-1832	83.80504	-5.30897	55.0	0.20	0.75
141-301[a]	83.80892	-5.38367	172.0	···	···
154-240[a]	83.81408	-5.37781	100.0	···	···
163-026	83.81788	-5.34053	159.0	0.25	0.40
165-254	83.81892	-5.38161	4.0	0.33	0.15
172-028	83.82175	-5.34114	140.0	0.57	0.35
174-236[a]	83.82229	-5.37672	57.0	···	···
176-543[a]	83.82313	-5.42850	32.0	···	···
177-341[a]	83.82363	-5.39469	105.0	···	···
179-353[a]	83.82475	-5.39817	145.0	···	···
181-247[a]	83.82533	-5.37981	165.0	···	···
182-332	83.82575	-5.39208	0.0	0.33	0.15
182-413[a]	83.82587	-5.40372	86.0	···	···
183-405	83.82637	-5.40136	43.0	0.71	0.35
183-419[a]	83.82629	-5.40528	70.0	···	···
191-232	83.82971	-5.37547	168.0	0.33	0.15
203-504[a]	83.83442	-5.41783	20.0	···	···
203-506	83.83458	-5.41825	16.0	0.50	0.20
205-421[a]	83.83550	-5.40583	70.0	···	···
206-446[a]	83.83592	-5.41292	80.0	···	···
218-354	83.84079	-5.39831	72.0	0.43	0.70
218-529	83.84092	-5.42464	176.0	0.50	0.20
239-334	83.84942	-5.39281	17.0	0.40	0.25
244-440[a]	83.85175	-5.41111	20.0	···	···
252-457[a]	83.85492	-5.41596	160.0	···	···
294-606	83.87242	-5.43508	86.0	0.25	0.50

Notes

[a] PA is estimated from orientations of jets.

[b] Radius of disk.

4.3 Result of the correlation of PA in five star-forming regions

We look for the statistical signature of the alignment of PA in the five star-forming regions; Orion, Lupus, Taurus, Upper Sco, and Ophiuchus. In summary, out of all regions except for the Lupus, four regions show the random orientations of disks. On the other hand, we find the possible alignment in the Lupus III at 2σ level, although the detection is still marginal. Table 4.1 lists the mean and the standard deviation of PA of disks and the p-value from the Kuiper test, which measures the extent to which the cumulative distribution $N(<\text{PA})$ is consistent with the uniform distribution, for the five star-forming regions. We discuss the results for each region below in order.

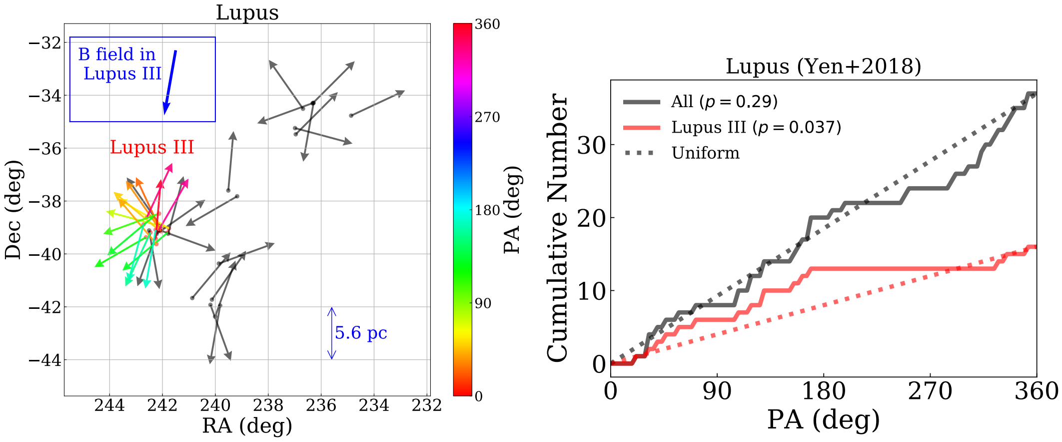

Figure 4.4 (left) Same as panel (a) of Figure 4.3. (right) Cumulative distribution of PA in the entire field and the Lupus III.

Firstly, we consider the Lupus region. The orientations of 37 disks are summarized in Figure 4.3, and their distribution projected along the z-axis defined in the equatorial coordinate system is plotted in Figure 4.2. Note that stars in the Lupus III are concentrated in the black box region with the depth of $\simeq 10$ pc. The distribution of PA and $\cos i$ is plotted in Figure 4.3, and Figure 4.4 shows the cumulative distribution of PA for the Lupus region. The PA estimated for the Lupus is based on the spectroscopic data of CO lines, allowing the estimate in the range of $0° \leq \text{PA} < 360°$. Thus, the PA in the left panel of Figure 4.4 is the angle measured counter-clockwise from the north to the direction of each arrow. While the entire field of the Lupus does not exhibit any preferential direction ($p = 0.29$), the disk axes in the Lupus III are orientated toward the east; Mean(PA) $\pm\ \sigma$(PA) $=77.3° \pm 69.9°$. The statistical significance of this alignment is barely 2σ ($p = 0.037$), but the inclination distribution in this region seems to exhibit the consistent correlation as well (Figure 4.3). The values of $\cos i$ are clustered around 0.6 for the Lupus III cloud in particular.

Nevertheless this could be an artifact due to the large uncertainties of $\cos i$ in Yen et al. (2018) that might distort the apparent distribution of $\cos i$ around 0.5 when combined with the selection bias toward $\cos i \approx 1$ disks (see Section 4.1). Therefore, we also examine the distribution of $\cos i$ independently estimated by Ansdell et al. (2016). Indeed their estimates of $\cos i$ for the entire Lupus region do not show a significant peak, but as long as 9 disks with PA in the Lupus III are concerned, the distribution of $\cos i$ by Ansdell et al. (2016) also exhibits a peak around 0.6. Thus we interpret that the clustering of $\cos i$ for the Lupus III is not an artifact, and consistent with the the alignment in PA of disks in the region.

Since some of disks are marginally detected by Yen et al. (2018), their PA values might be susceptible to systematical noises, which can affect the result of the alignment.

To investigate this possibility, we produce the correlation plot for signal-to-noise ratios of CO emission and PA in Figure 4.5. From the plot, we find that there is no clear correlation between the flux and PA values. Additionally, even if we consider only the disks with high confidence e.g. S/N larger than 10, the signature of the alignment still holds, although the significance is weak due to the small statistics. Thus, it would be unlikely that some unknown systematics produce the alignment in the Lupus III.

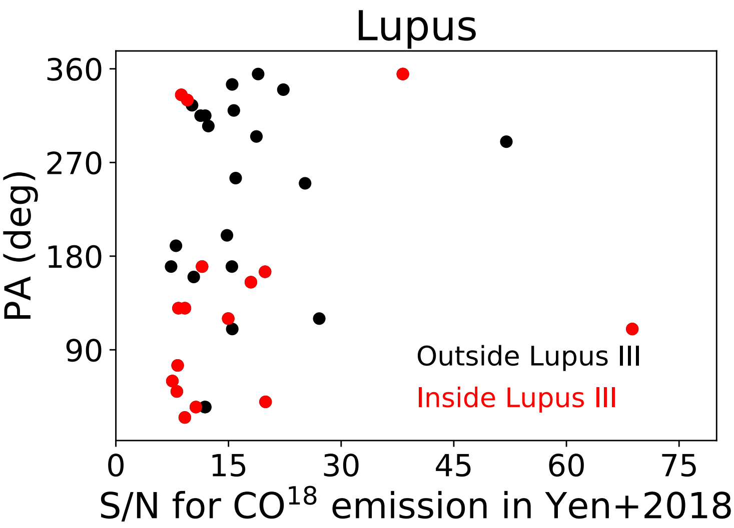

Figure 4.5 Correlation plot for signal-to-noise ratios and position angles. Red points correspond to the disks in the Lupus III.

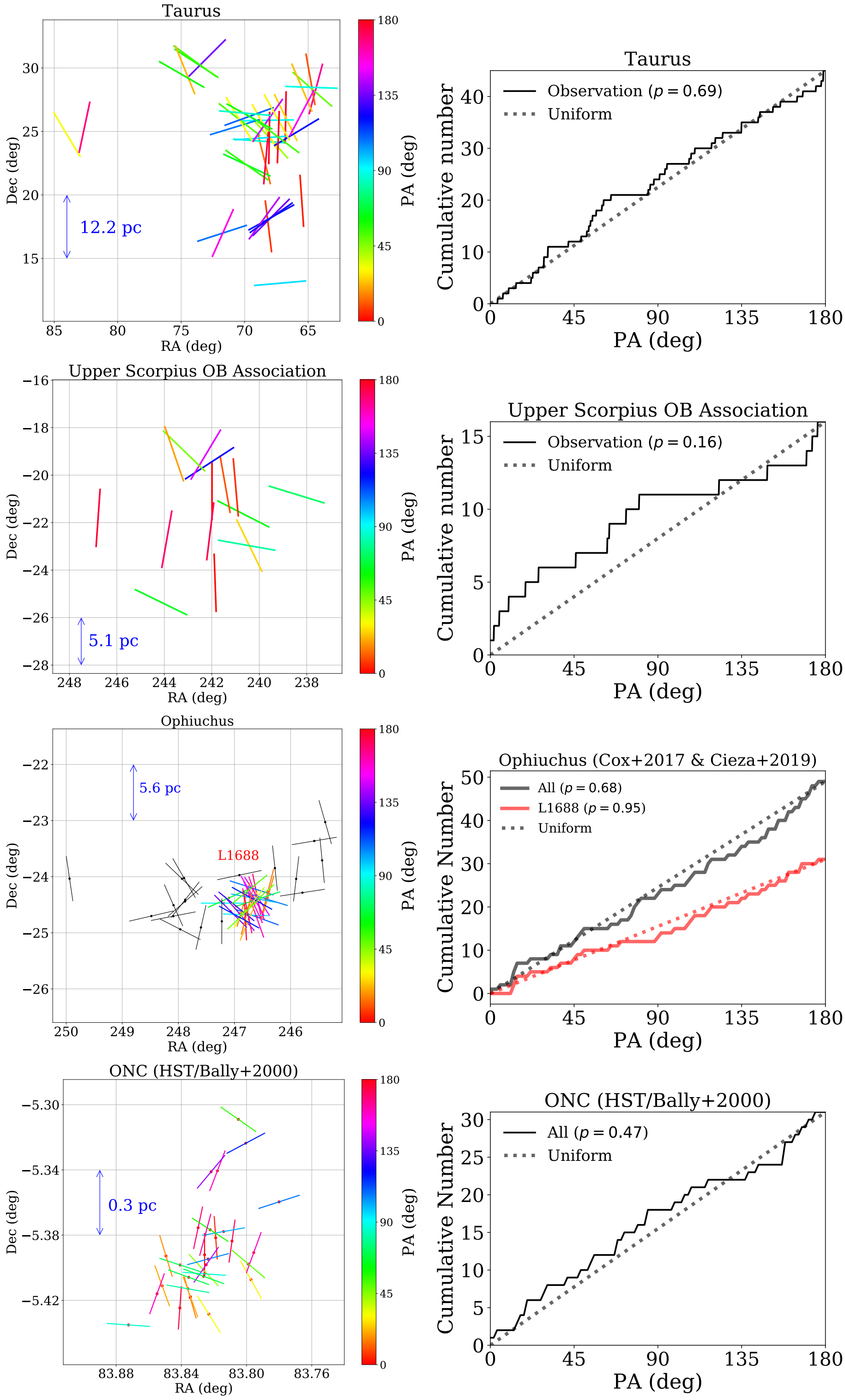

Figure 4.6 Same as Figure 4.4 but the bars represent directions of major axes of disks. Plots include Taurus, Upper Sco, Ophiuchus, and ONC in order.

The other three regions, Taurus, the Upper Scorpius, Ophiuchus, and ONC do not exhibit any significant signature of alignment as shown in Figure 4.6. In the Taurus region, the disks seem to be randomly oriented in the entire field. Disks in smaller subregions seem to be locally correlated, but it is not clear if the correlation is statistically significant. In the Upper Scorpius, the entire field shows weak alignment ($p = 0.16$), which is suggestive but not conclusive. In the Ophiuchus, the entire field shows no clear alignment either in the entire region ($p = 0.68$) or in the L1688 cloud ($p = 0.95$) if we adopt the estimations from Cox et al. (2017) for overlapped disks. Although we also attempt the analysis by adopting the estimations from Cieza et al. (2019) for the overlapped systems, we cannot find any signatures of the alignment either: $p = 0.97$ for the entire region, and $p = 0.94$ for the L1688 cloud. Additionally, in the ONC, 31 disks by Bally et al. (2000) do not show statistically significant signature of such alignment.

4.4 Comparison of different estimators of PA: case of Lupus cloud

The estimated values of PA even for the same data are somewhat different in previous literature, which may indicate that the estimates are sensitive to the adopted reduction method. This could bias the evidence of the alignment discussed in Section 4.3. Therefore, it is important to make sure of the robustness of derived PA against the choices of their estimators. In this section, we introduce three specific methods of estimating PA, and compare the results. In the analysis, it is not straightforward to implement sparse modeling. Thus, we select the Lupus disks, among which we detect the possible alignment, as the fiducial data for the comparison.

The first method (Section 4.4.1) is the straightforward and intuitive one, which uses the disk image produced by CLEAN and deconvolves it with an elliptic gaussian function. The second one (Section 4.4.2) does not analyze the disk image, but directly fits the gaussian function or disk models to the visibility on the *uv* plane, which has been adapted in literature (e.g Ansdell et al., 2016; Tazzari et al., 2017). In the third method (Section 4.4.3), we create a super-resolution image of the disk using sparse modeling, and apply the gaussian fit. The sparse modeling is now recognized as one of the most powerful techniques in a broad area of science, and indeed it played a vital role recently in the black hole shadow imaging (Event Horizon Telescope Collaboration et al., 2019). Incidentally, to our knowledge, the present chapter is the first attempt to reconstruct multiple protoplanetary disk images using the sparse modeling.

For the purpose of comparison, we choose visibilities measured by Ansdell et al. (2016) and the disks identified in the chapter as a fiducial dataset. Out of their ALMA (the Atacama Large Millimeter/submillimeter Array) survey of proto-planetary disks in the Lupus clouds, we analyze 29 disks with estimated PA (listed in their Table 2). First, we download the raw data from the ALMA Science Archive (https://almascience.nao.ac.jp/aq/). Then, we calibrate and reduce the data using CASA 4.4.0. Then, we exclude line emissions and average over the wavelengths using the standard pipelines, and extract the disk continuum emission alone. After the standard calibration, we apply self-calibration that adjusts the gains of antennas using the bright emissions of targets so as to increase the S/N.

4.4.1 CLEAN+`imfit`

CLEAN is an intuitive and widely-used routine to visualize astronomical objects from the interferometric data, as already used in the case of ONC (see Section 4.2.5). The CLEAN routine first Fourier transforms the observed visibilities, and produces an initial image. Next, it identifies the highest peak beyond the threshold (= 0.001 Jy/Beam in case of the Lupus), which roughly corresponds to 3σ level in the image, and subtracts the point spread function (called dirty beam in radio astronomy) at the peak position from the image. The fraction of the subtraction is specified by the gain parameter `gain` (we adopt `gain`=0.02 in the current analysis). This process is repeated iteratively, until the maximum flux in the residual image becomes less than the threshold, or the number of iterations exceeds 10,000. Following the procedure in the pipeline, we adopt a Briggs weighting with a robust weighting parameter of 0.5. Here, the Briggs weighting is a combination of natural weighting (constant weights to all visibilities) and uniform weighting (weights inversely proportional to visibility density), and the robust weighting parameter determines the relative ratio of the two weighting (Briggs, 1995). The typical frequency of the observation is ~ 335 GHz, and the typical beam size is $0.34'' \times 0.28''$ ($\simeq 48$ au × 39 au for 140 pc), which is comparable to the diffraction limit of $\lambda/D_{\rm max}$, with λ and $D_{\rm max}$ being the observed wavelength and the maximum length of the baseline. After creating images using the CASA task `clean`, we deconvolve them with the two-dimensional elliptical Gaussian function using the CASA task `imfit`, which returns the value of PA and the associated error. Figure 4.7 shows an example of the disk, Sz 90, in the Lupus clouds imaged by `clean`.

4.4.2 `uvmodelfit`

Instead of measuring PA of the reconstructed image in real space from interferometric data, one can derive PA directly by analyzing the visibility data on *uv* plane (e.g Ansdell et al., 2016; Tazzari et al., 2017). In particular, since Fourier transform of the Gaussian function is also Gaussian, the Gaussian fitting can be more directly implemented in the visibility defined on *uv* plane. Indeed there exists a CASA task `uvmodelfit` for that purpose, which has been applied to determine PA of disk systems, independently of that based on CLEAN+`imfit`. The non-linear fitting routine implemented in `uvmodelfit` requires an iteration, which we attempt up to 20 times. Figure 4.8 shows an example of the analysis with `uvmodelfit`.

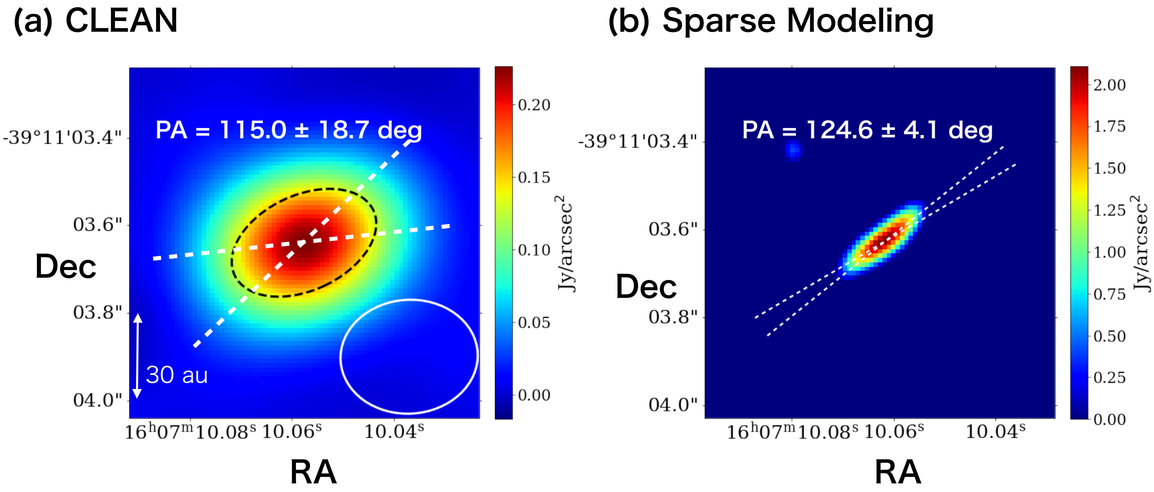

Figure 4.7 Flux maps of a disk around Sz 90 in the Lupus clouds. The size of boxes is $0.8'' \times 0.8''$, and we adopt (α, δ) in J2000. *Left*: Image created by `clean`; see Section 4.4.1. The black dashed ellipse represents the size of the source deconvolved from the beam, whose size is shown as the white ellipse in the lower right. *Right*: Image created by sparse modeling with $(\Lambda_l, \Lambda_t) = (10^2, 10^2)$. See Section 4.4.3 for details of the sparse modeling.

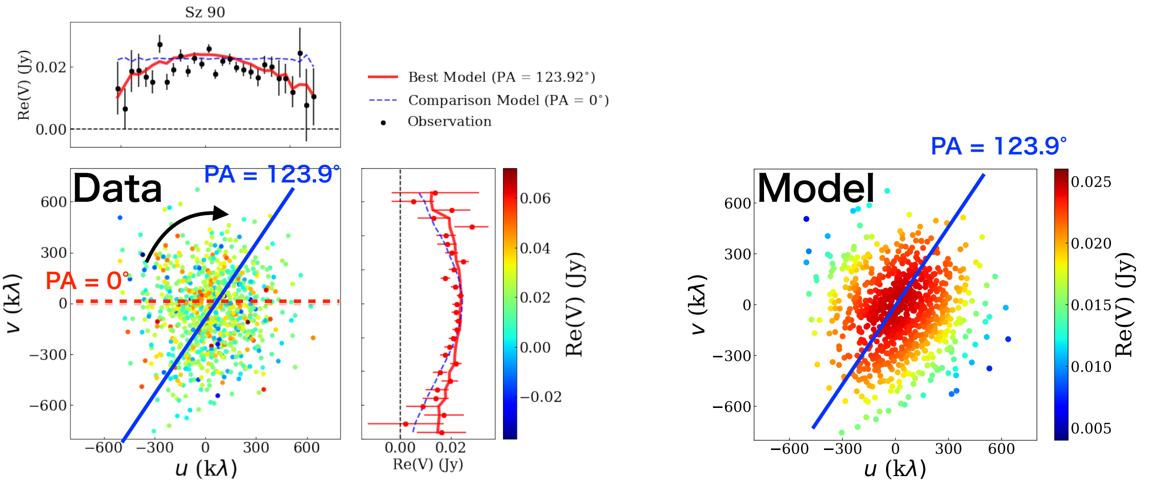

Figure 4.8 Example of the PA fit for Sz 90 from `uvmodelfit` in Section 4.4.2. The points on the uv plane indicate the real part of the visibilities color-coded according to the right-bar. *Left*: Observed visibilities. Upper and right panels show their projected binned values along v and u directions, respectively. Blue lines show the best-fit model with PA=123.9°, which should be compared with PA=115.0°±18.7° (CLEAN) and 124.6°±4.1° (sparse modeling) presented in Figure 4.7. Lines in the scatter plot show major axes of Gaussian functions on visibility plane. For comparison, we also plot the case of PA = 0° in red dashed lines. *Right*: Visibility plots for the best-fit model.

4.4.3 Sparse modeling

Recent progress in data science indicates a possibility to reconstruct the image of astronomical objects with its angular resolution better than the conventional diffraction limit $\lambda/D_{\rm max}$. In particular, a super-resolution technique on the basis of sparse modeling attracts significant attention, and has proved to be successful in a variety of areas. In short, sparse modeling is one of the mathematical frameworks to estimate the essential information content buried in the data that are dominated by a small number of base functions. In that case, even if the observation samples only a fraction of the entire data space, one may recover the precise information using the sparsity in the solution. Indeed this is very well suited for the radio interferometric observation in which the available uv-plane coverage is very limited (e.g. Honma et al., 2014; Ikeda et al., 2016; Akiyama et al., 2017b,a; Kuramochi et al., 2018; Event Horizon Telescope Collaboration et al., 2019).

Indeed, an effective angular resolution of interferometric images reconstructed with sparse modeling has been shown to become better than 0.2∼0.3 $\lambda/D_{\rm max}$ (e.g. Kuramochi et al., 2018). Thus one can expect that the PA estimated with sparse modeling improves these estimates based on conventional methods including CLEAN+`imfit` and `uvmodelfit`. Note, however, that our main purpose here is not to identify the small-scale structures of scales $\ll \lambda/D_{\rm max}$, but to estimate PA of the resolved disks after smoothing over their typical sizes $\sim \lambda/D_{\rm max}$. Therefore we do not expect that the PA estimated with sparse modeling is much different from that with CLEAN+`imfit` or `uvmodelfit`, but do want to make sure of the robustness of the estimated values through their mutual comparison.

4.4.3.1 Formulation of sparse modeling

In sparse modeling, in addition to the standard chi-squared value χ^2, additional regularizations are introduced in the cost function. In this chapter, we use the following expression to find the best intensity maps $\boldsymbol{I} = \{I_{i,j}\}$ in reference to Kuramochi et al. (2018):

$$\boldsymbol{I} = \arg\min_{I}(\chi^2(I) + \Lambda_l||\boldsymbol{I}||_1 + \Lambda_t||\boldsymbol{I}||_{\rm tsv}) \ \ \text{s.t.} \ \ I_{i,j} \geq 0, \tag{4.5}$$

where $||\boldsymbol{I}||_p$ is the Λ_p norm of $\boldsymbol{I}$:

$$||\boldsymbol{I}||_p = \left\{ \sum_i \sum_j |I_{i,j}|^{1/p} \right\}^p . \tag{4.6}$$

The first term $\chi^2(\boldsymbol{I})$ in Eq (4.5) is the standard χ^2-term that expresses the difference between observed and model visibility in the complex plane:

$$\chi^2(\boldsymbol{I}) = \sum_k \frac{1}{\sigma_k^2}(\boldsymbol{V}_k - (\boldsymbol{F}\boldsymbol{I})_k)^2, \tag{4.7}$$

where $\boldsymbol{V}_k$ is the k-th observed visibility, σ_k is the observational error associated with $\boldsymbol{V}_k$, and $(\boldsymbol{F}\boldsymbol{I})_k$ is the model visibility (Fourier transformation of $\boldsymbol{I}$) corresponding to $\boldsymbol{V}_k$. In Eq (4.5), $\Lambda_l||\boldsymbol{I}||_1$ is the regularization term with Λ_1 norm, which is known to construct sparse solutions (due to its nature). The coefficient $\Lambda_{\rm l}$ controls sparsity in solutions; the larger $\Lambda_{\rm l}$ prefers sparse solutions (less number of non-zero $I_{i,j}$). Finally, the third term in Eq (4.5) is the TSV regularization with the coefficient Λ_t defined as follows:

$$||\boldsymbol{I}||_{\rm tsv} = \sum_i \sum_j (|I_{i+1,j} - I_{i,j}|^2 + |I_{i,j+1} - I_{i,j}|^2), \tag{4.8}$$

which represents the squared sum of a gradient of an image. By minimizing this TSV regularization, we favor a smooth solution with less variations in $I_{i,j}$. When finding the optimal solution in Eq (4.5), we use a monotonic fast iterative shrinkage thresholding algorithm (MFISTA) introduced by Beck & Teboulle (2009b,a) following Akiyama et al. (2017a). We finish fitting until 1000 iterations or achieving convergence; we find that almost all fitting is converged before reaching 1000 iterations. These processes are implemented by PRIISM (Nakazato et al., 2019).

In this chapter, we choose $\Lambda_l = 10^0, 10^1, 10^2, 10^3$ (Jy^{-1}) and $\Lambda_t = 10^0, 10^2, 10^4, 10^6, 10^8$ (Jy^{-2}) as fiducial coefficients in sparse modeling. The prepared size of $\boldsymbol{I}$ is 200 pixels square, where 1 pixel corresponds to $0.01''$. Among 20 solutions with different sets of (Λ_l, Λ_t), we choose the optimal solutions using 10-fold cross-validation (CV) (see the detail in Akiyama et al. (2017b)). In the process of CV, we first separate the data into training and testing sets. Specifically, we randomly partition the visibility into 10 sets, and we sum up 9 sets as training data, to which we apply the sparse modeling. Then, we compute the Mean Squared Error (MSE) between the testing data and the model visibility obtained from fitting the training data. We iterate this process 10 times by choosing different training sets, and we derive the mean of MSE as well as the standard deviation of mean MSE; the standard deviation of mean MSE is computed as the standard deviation of values of MSE divided by $\sqrt{10-1}$. Finally, we obtain 20 images with MSE and its error $\{\mathrm{MSE}_i,\ \sigma(\mathrm{MSE}_i)\}$ for sets of (Λ_l, Λ_s). In CV, the lower value of MSE is favored as solutions, so we determine the image with lowest MSE to be the best solution with $\{\mathrm{MSE}_{\mathrm{best}},\ \sigma(\mathrm{MSE}_{\mathrm{best}})\}$.

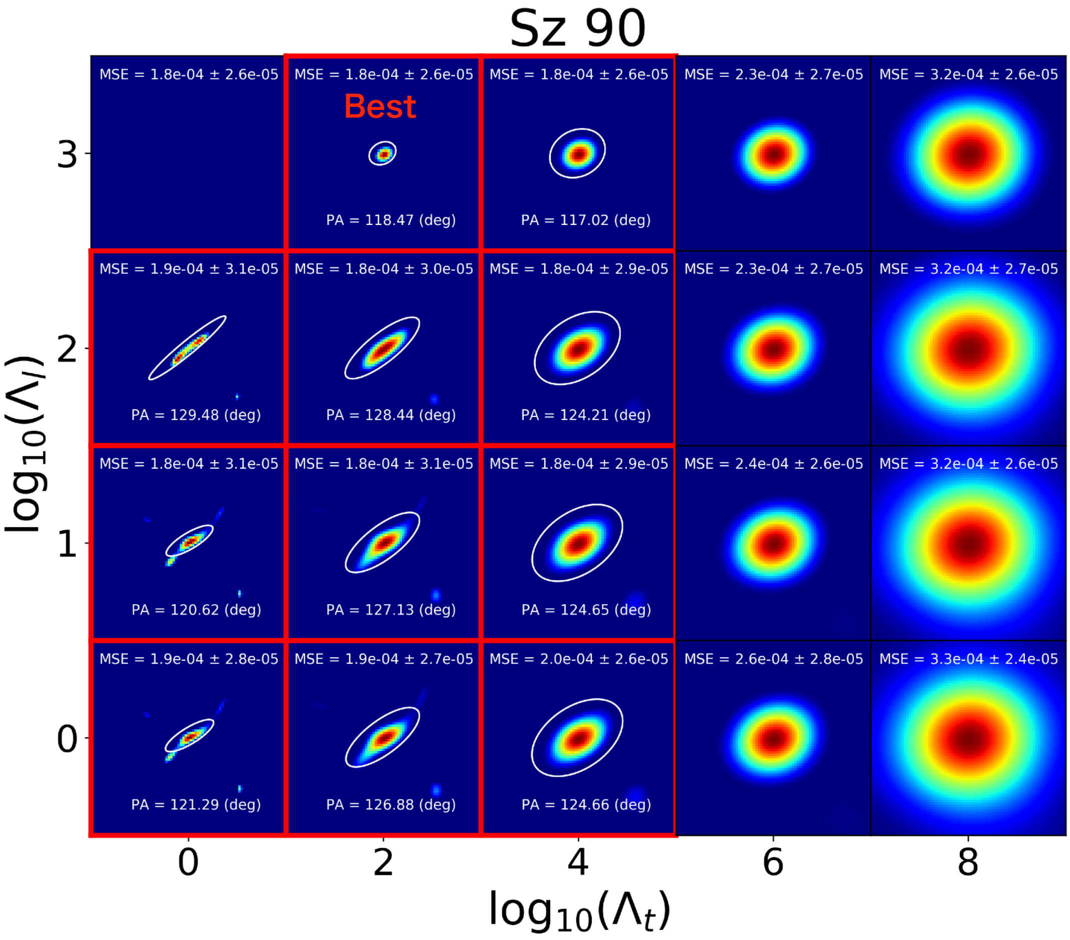

Figure 4.9 Imaging of a disk around Sz 90 using sparse modeling. The size of each box is 0.8″× 0.8″. There are 20 images corresponding to combinations of Λ_1 and Λ_{tsv}. We also show Mean Squared Error (MSE) and its 1σ uncertainty in the panels. Red panels have MSE less than $\mathrm{MSE}_{\mathrm{best}} + \sigma(\mathrm{MSE}_{\mathrm{best}})$ (consistent with lowest MSE within 1σ level). In computing PA, we only use the data in the white ellipse. The average value of PA among likely solutions (red panel) is PA $= 124.6 \pm 4.1°$.

4.4.3.2 Methods of estimating PA in sparse modeling

Using the derive images with sparse modeling, we try two methods for estimating PA in this chapter. The first method is fitting the two-dimensional elliptical Gaussian function to the images. The second method uses the tensor of second-order brightness moments defined as:

$$\boldsymbol{Q} = \frac{\sum_i \sum_j q(\boldsymbol{r}_{i,j}, L) I_{i,j} (\boldsymbol{r}_{i,j} - \bar{\boldsymbol{r}})(\boldsymbol{r}_{i,j} - \bar{\boldsymbol{r}})^T}{\sum_i \sum_j q(\boldsymbol{r}_{i,j}, M) I_{i,j}}, \tag{4.9}$$

where $\boldsymbol{r}_{i,j} = (x_i, y_j)$. Here, $q(\boldsymbol{r}_{i,j}, L)$ is the step function defined as

$$q(\boldsymbol{r}_{i,j}, L) = \begin{cases} 1 & (\boldsymbol{r}_{i,j} \in M) \\ 0 & (\text{otherwise}), \end{cases} \tag{4.10}$$

where the region L determines the non-zero pixels in Eq (4.9).

We find that it fails to estimate PA if we use all pixels of the image. This is due to artificial non-zero pixels produced by sparse modeling. Thus, we divide estimations into two steps. As the first step, we roughly determine the region L for the analysis of PA by fitting a gaussian function to all pixels. Specifically, we determine L to be 3σ contours of derived gaussian considering the fact that the signal-to-noise ratios of emissions from disks are $S/N \sim 400$ at most. Then, using the data only in L, we derive PA using a gaussian function and tensor of second-order brightness moments.

Among 20 images with different sets of (Λ_l, Λ_s), we exclude images with large MSE to estimate PA from observations. Specifically, we use PA estimated only from images with MSE less than $\mathrm{MSE_{best}} + \sigma(\mathrm{MSE_{best}})$. Using the sets of PA, we compute the mean and the standard deviation of them. Figure 4.9 shows the example of images with sparse modeling, and we find $\mathrm{PA} = 124.6 \pm 4.1°$.

4.4.4 Comparison of PA of disks in the Lupus clouds derived from the three methods and previous literature

Now let us compare the values of PA of disks in the Lupus clouds estimated from the three different methods, as well as the published values of PA (Tazzari et al., 2017; Yen et al., 2018). For the fair comparison, we also adopt the completely independent observation (Ansdell et al., 2018), which observed the disks in Ansdell et al. (2016) as well. Although the signal-to-noise ratios in Ansdell et al. (2018) are relatively small, the angular resolution is better ($\sim 0.25''$) than Ansdell et al. (2016). As there are no published PA in the data presented by Ansdell et al. (2018), we reduce and calibrate the data by ourselves using the prepared pipeline, and derive PA using CLEAN+`imfit`.

Therefore, there are six independent measurements of PA: CLEAN+`imfit`, `uvmodelfit`, sparse modeling, fitting visibility with physical disk model (Tazzari et al., 2017), spectroscopical estimation based on Keplerian motion (Yen et al., 2018), and CLEAN+`imfit` for the data in Ansdell et al. (2018). We adopt the values of PA derived from CLEAN+`imfit` in Ansdell et al. (2016) as the reference of the comparison. Six panels in Figure 4.10 show the difference ΔPA against reference value (CLEAN+`imfit` with Ansdell et al. (2016)).

Panels (a)-(c) represent the result for the elliptical Gaussian fit of the sparse modeling image, surface brightness tensor of the sparse modeling image, and `uvmodelfit`, respectively. It is reassuring that the tensor and Gaussian fit of the same image in panels (a) and (b) yield almost identical results. As illustrated clearly in Figure 4.7, sparse modeling identifies small-scale structures that are impossible to see in the conventional CLEAN image, while they have to be interpreted carefully. Such small-scale structures, however, do not affect the PA measurement of the proto-planetary disks that requires the smoothing over the disk size. Therefore, we made sure that the PA measured from the decomposition of the CLEAN image significantly convolved with the similar beam size is in reality consistent with that independently estimated with sparse modeling.

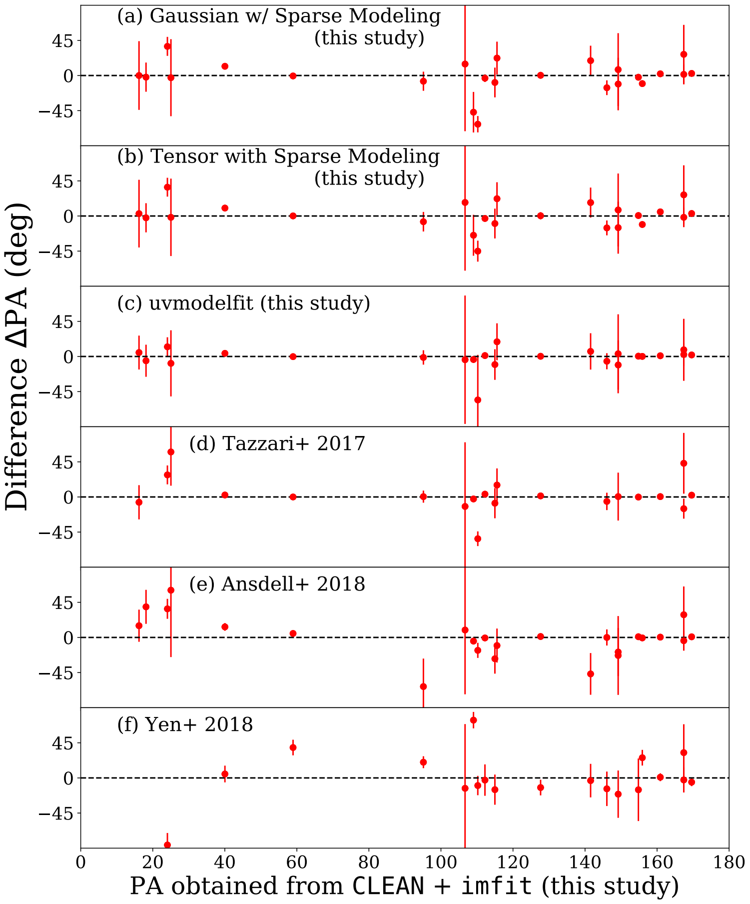

Figure 4.10 Comparison of PA of disks in the Lupus clouds. Panels (a)-(d) use the same data as in Ansdell et al. (2016). The reference value derived using CLEAN and `imfit` is plotted in the horizontal axis. The difference of the PA derived from different methods relative to the reference value is plotted in the vertical axis. a) elliptical Gassuain fit of the sparse modeling image, b) tensor fit of the sparse modeling image, c) `uvmodelfit`, d) Tazzari et al. (2017), e) CLEAN+`imfit` for data in Ansdell et al. (2018), f) Yen et al. (2018).

Panels (a)-(c) present the results for the same dataset (Ansdell et al., 2016) but based on different analysis methods performed by ourselves. In contrast, panel d) presents comparison between our result and Tazzari et al. (2017) that directly fit the visibility data to physical model for the same data, which indicates that both are basically consistent.

Panel (e) plots the comparison of the different datasets (Band 6 of Ansdell et al. (2018), and Ansdell et al. (2016)) but analyzed using the same method (CLEAN + `imfit`) by us. Again, both datasets yield mostly consistent values, supporting the robustness of the PA values estimated from with the data presented by Ansdell et al. (2016).

Finally, panel (f) shows the comparison with the spectroscopic analysis by Yen et al. (2018), which is also used in the current analysis in Section 4.3. Out of the 22 overlapped disks, we find that 15 disks satisfy $|\Delta\mathrm{PA}| < 30^\circ$, and the mean and median of ΔPA are 0.17° and 30°, respectively, implying that the bias is not large, despite the large scatter.

In summary, our systematic comparison using the Lupus data made sure that there is no significant bias in the estimated PA among different analysis methods and datasets, although there are relatively large scatters.

4.5 Apparent alignment introduced by systematical noise

The disks in ONC were also observed by ALMA in Eisner et al. (2018), and we can exploit their observations to investigate the alignment. They did not present the published values of disk orientations, so we attempt to estimate the directions of disk's majors axes by ourselves. However, during the analysis, we find that the alignment can be apparently realized among disks due to systematical errors associated with observations. Here, we briefly explain this possible false positive of the alignment found in ONC.

Eisner et al. (2018) surveyed $1.'5 \times 1.'5$ region of the ONC around the central massive star θ^1 Ori C, and, from the mosaic map constructed from 136 pointings, they detected the submillimeter continuum excesses for 104 stars with $> 4\sigma$ level. The excess fluxes of some systems do not come from dust, but are dominated by free-free emission due to external radiation from nearby OB stars (Eisner et al., 2018). Since the values of PA of most ONC disks are not available in the literature, we attempt to analyze the raw data at the ALMA Science Archive (https://almascience.nao.ac.jp/aq/) by ourselves. Specifically we reduce and calibrate the ONC data using the prepared pipelines with CASA 5.4.2, and then apply the self-calibration. Then, we image the region using the CASA task `tclean` (`gridder=mosaic` and `mosweight=True`), and, finally, we fit the CLEAN images using `imfit` in CASA. The fit was made for the circular region of a radius of 30 pixels (or $0.36''$), which safely covers the radio emission, around each object.

Using the measurement of PA for disks, we attempt to find the alignment among disks. A fraction of disks are not well resolved or detected due to the observational limitations, so we select 36 disks with fairly resolved emission for the analysis. We find that these disks show the significant alignment with the mean direction PA $\simeq 30^\circ$ at 6σ level.

On the other hand, we also check the goodness of the calibration by investigating the images of the check source, which was observed in between the measurement of the calibrators and science targets. Generally, the check source should be the point source, but in this observation, it is not point source but has the finite size $\simeq 0.06''$ with PA $\simeq 40^\circ$. We suspect that the same spreading also distorts the images of disks in ONC, which lead to the apparent alignment in the field. We note that the large distortion of the image of the check source is also consistent with large phase scatters during the calibration.

Since phase errors are likely to distort the small objects, we attempt to investigate the alignment only using comparatively large disks. As a result, we find $p = 0.005$ for 23 disks with length of major axes larger than $0.13''$, and $p = 0.28$ for 12 disks large than 0.15″, and both of groups show the mean direction PA $\simeq$ 30°. Due to the large systematical errors, these results are not far from conclusive, but can be suggestive, and the additional analyses or observations with better conditions and resolutions would be encouraging for discussing the alignment in this region further.

4.6 Discussion

One of the possible origins of the angular momentum of disks is the random turbulence field in the progenitor molecular cloud cores (e.g. Burkert & Bodenheimer, 2000). If so, one may expect different cloud cores, and thus disks formed out of them, would exhibit random orientation even in the same cloud. In this study, we find random orientations in the four regions, and this is basically consistent with the turbulent origin of the angular momentum. On the other hand, the Lupus III region shows the preferential direction among the disks, and this is suggestive and might imply the additional processes including the coherent global rotation of the initial cloud and/or the magnetic field that account for generation of the angular momentum.

While correlation among the directions of magnetic fields, disk rotations, and jets/outflows have been extensively studied by observations and simulations, there is no consensus (Ménard & Duchêne, 2004; Curran & Chrysostomou, 2007; Targon et al., 2011; Hull et al., 2013; Tatematsu et al., 2016; Planck Collaboration et al., 2016a; Mocz et al., 2017; Hull et al., 2017; Stephens et al., 2017; Chen & Ostriker, 2018; Kong et al., 2019). In the following, we present discussion concerning the possible effect that generate the disk alignment.

Consider first the magnetic field. The relative importance of the magnetic field may be characterized by the Alfvén Mach number:

$$\mathcal{M}_{\rm A} = \frac{\sigma_v}{v_{\rm A}} = \frac{\sqrt{4\pi\rho}}{B}\sigma_v, \tag{4.11}$$

where σ_v is the turbulent velocity dispersion of the gas, $v_{\rm A}$ is the Alfvén velocity, and B and ρ are the magnetic field and mass density of the gas cloud. It is natural to expect that the magnetic field contributes to the alignment of disk orientations if it exceeds the random turbulent motion of gas, $\mathcal{M}_A < 1$. Indeed, Planck Collaboration et al. (2016a) found on the basis of the *Planck* data that all of molecular clouds, including the five regions considered in this chapter, are Alfvénic ($\mathcal{M}_A \simeq 1$) or sub-Alfvénic ($\mathcal{M}_A < 1$) by comparing simulations and observations. Furthermore, Hull et al. (2017) found that at least the shape of gas clouds with $\mathcal{M}_A < 1$ is significantly affected by the magnetic field.

Chandrasekhar & Fermi (1953) derived that the angular dispersion of the magnetic field direction, σ_ϕ (rad), is equal to the Alfvén Mach number. If σ_ϕ is assumed to be the same as σ_ψ that is the angular dispersion of the polarization vector direction, one can estimate $\mathcal{M}_{\rm A}$ from the observed value of σ_ψ as

$$\mathcal{M}_{\rm A} \simeq \sigma_\psi. \tag{4.12}$$

Table D.1 of Planck Collaboration et al. (2016a) shows that $\sigma_\psi = 36° \pm 0.1°$ in the Orion, $\sigma_\psi = 46° \pm 0.1°$ in the Lupus, $\sigma_\psi = 43° \pm 0.1°$ in the Taurus, and $\sigma_\psi = 29° \pm 0.1°$

in the Ophiuchus. Therefore, Eq (4.12) implies that $\mathcal{M}_{\rm A} \simeq 0.6 \sim 0.8$, and there is no large difference in values of $\mathcal{M}_{\rm A}$ for those regions. Unless the assumption $\sigma_\phi \sim \sigma_\psi$ is broken due to the projection effect of polarization vectors, it is unlikely that the strong magnetic field is responsible for the alignment observed only in the Lupus.

Next, let us consider if the disk orientations in Lupus III are somehow related to the global shape and magnetic field of the star-forming regions. For that purpose, we estimate the magnetic field in the region using the *Planck* polarization map, "COM_CompMap_DustPol-commander_1024_R2.00.fits" at NASA/IPAC Infrared Science Archive, (Planck Collaboration et al., 2016a). The angular resolution is $10'$, which roughly corresponds to 1.2 pc in spatial scales for systems at a distance of 400 pc.

The Lupus III cloud exhibits the filamentary structure along the direction PA$\simeq 90^\circ$ (Benedettini et al., 2015). There is no associated velocity gradient in the Lupus III, so there is no indication of the rotation (Benedettini et al., 2015). Using the Planck data, we determine the direction of magnetic field to be PA $\simeq 10^\circ$ at the scale of 0.3° and $\simeq 170^\circ$ the scale of 1° in the Lupus III adopting the bilinear interpolation. Thus the magnetic field there is also roughly perpendicular to the direction of the filamentary structure (see also Planck Collaboration et al. (2016a)).

Since the spectroscopic data in the Lupus region allow to estimate the PA of the disks in the range of $0^\circ \leq \mathrm{PA} < 360^\circ$, the derived value of Mean(PA) $\pm\, \sigma$(PA) $=77.3^\circ \pm 69.9^\circ$ indicates the coherent rotation of those disks and the disk planes are parallel to the filamentary structure of the gas cloud, and perpendicular to the magnetic field there. It is interesting to note that the directions of filamentary structure and the magnetic field are roughly perpendicular in the Lupus III, and indeed that they are correlated with the disk orientations in the Lupus III. This may be suggestive, but not conclusive at this point. Due to the limited statistics and uncertainties of the disk and magnetic field data, further quantitative analysis is not easy at this point, but additional and future observations would be very rewarding.

Finally we note that the stellar density may be an important parameter for the disk alignment, which varies a lot among the five regions; 4700 pc^{-3} (ONC), 500 pc^{-3} (Lupus III), 6 pc^{-3} (Taurus), $\geq$ 80 pc^{-3}(Upper Sco), and 610 pc^{-3} near L1688 (Ophiuchus) (Nakajima et al., 2000; King et al., 2012). If the mean separations among stars are small, gravitational torques from nearby stars would become significant. In reality, the Lupus III with the potential alignment has the small scale $\simeq 3$ pc, in marked constrast to > 10 pc for Taurus and Upper Sco. On the other hand, since the L1688 or ONC observed by HST does not show any signature of the disk orientation even on a scale of ~ 1 pc, the observed size of the region alone does not explain the apparent presence/absence of the disk alignment.

4.7 Summary

The spatial correlation among proto-planetary disk rotations in star-forming regions may carry unique information on physics of the multiple star formation process. In this chapter, we focus on five nearby star-forming regions where many proto-planetary disks are spatially resolved with ALMA, and search for the statistical signature of the alignment of the position angles of the disks.

Our major findings are summarized as follows;

1 We attempt to find the spatial correlation of disks among particular five star-forming regions using measured PA. In order to see if the distribution of the PA is consistent to be uniform, we applied the Kuiper test. In the four regions,Taurus, Upper Scorpius, Ophiuchus, and ONC, the PA distribution is consistent with the uniform distribution. This result is not inconsistent with the turbulent nature of angular momentum. On the other hand, the disks in the Lupus III region show the possible alignment at 2σ level. This is not conclusive but suggestive for the further investigation.

2 We examined three different estimators for the PA measurement, CLEAN+`imfit`, `uvmodelfit`, and sparse modeling for the Lupus region. As expected, sparse modeling yields a super-resolution image of disks, from which we can estimate the PA without deconvolving the beam that is often comparable to the size of the disk. Nevertheless the resulting values of the PA between CLEAN+`imfit` and sparse modeling are in good agreement. We also confirm the agreement with previous literature (Tazzari et al., 2017; Yen et al., 2018) and the independent observation (Ansdell et al., 2018). While our study is limited to the case of the Lupus clouds, the estimations of PA would be independent of estimators.

3 In the Lupus III, the directions of the magnetic field and the filamentary structure are roughly perpendicular, implying that the collapse dynamics of those structures are somehow related to the magnetic field. Additionally, the disk orientation in Lupus III is fairly aligned with the nearby filament. Since the Planck data imply that the $\mathcal{M}_{\rm A}$ in those five regions is very similar, it is unlikely that the magnetic field is mainly responsible for the observed alignment in the Lupus. Therefore the role of the magnetic field in the disk alignment is not clear at this point, but deserves to be revisited with future data.

In addition to the disk alignment that we have studied here, jets and outflows may be used as independent tracers of the stellar spin axes (e.g. Stephens et al., 2017). While the disk rotation and the stellar spin may be slightly misaligned, such complementary statistics are very important to understand the star formation and evolution of the disk and stellar angular momenta, particularly in the context of the observed spin-orbit misalignment of exo-planetary systems (e.g. Ohta et al., 2005; Bate et al., 2010; Huber et al., 2013; Winn & Fabrycky, 2015; Kamiaka et al., 2018, 2019; Suto et al., 2019). Moreover, investigating the misalignment between stellar and disk axes itself would be interesting (e.g. Davies, 2019).

Our comparison for estimating PA in different methods is still limited to the case of the Lupus clouds. In addition, our current result is statistically limited. Thus, future analyses or observations of other disk systems, especially for ONC, are highly desired. The origin of the alignment is still unclear, and magnetohydrodynamical simulations covering thedynamic range from giant molecular cloud down to disk scales (e.g. Kuffmeier et al., 2017; Mocz et al., 2017) or observations (e.g. Hull et al., 2017) are necessary to understand the implication of the statistics of the current result. We have started such attempts by analyzing simulation results using the data given by Chen & Ostriker (2018). Our study is the first step to understand alignment among disks and its implications for star formation, and we hope to report the results of these advanced studies elsewhere.

Chapter 5

Global Mapping of an Exo-Earth using Sparse Modeling

As summarized in Section 2.2.3, scattered light of directly imaging Earth-like exoplanets can be interpreted as indications of movements of surface inhomogeneity resulting from orbital and rotational motions (Ford et al., 2001; Pallé et al., 2008; Cowan et al., 2009; Oakley & Cash, 2009; Fujii et al., 2010; Cowan et al., 2011; Fujii et al., 2011). As explained in Section 2.2.3.2, Kawahara & Fujii (2011) formulated an inversion method named spin–orbit tomography (SOT) for recovering 2D-surface maps by introducing Tikhonov regularization (L2-norm), which enables the direct estimation of the surface albedo. The same technique was applied successfully by Fujii & Kawahara (2012) to reconstruct 2D maps even for planets with various obliquities and orbital inclinations. Also, Kawahara (2016) revealed the relation between the planet spin axis and the frequency modulation of light curves. Farr et al. (2018) constructed the Bayesian framework of 2D mapping and quantified the uncertainty in the albedo map and the obliquity. They applied the Gaussian process to regulate the inter-pixel variance of the map instead of the L2 term. Recently, Fan et al. (2019) successfully recovered a global map with Tikhonov regularization from real observational multi-wavelength light curves of the Earth during the two-year DSCOVR/EPIC observations (Jiang et al., 2018). This is a clear practical example of how to mitigate the effects of clouds from light curves.

The aim of this study is to improve the spatial resolution of an inferred map using sparse modeling. This approach attracts increasing attention in the field of astronomy (e.g. Honma et al., 2014; Ikeda et al., 2016; Akiyama et al., 2017b,a; Kuramochi et al., 2018; Event Horizon Telescope Collaboration et al., 2019). As fiducial data, we adopted the mock albedo map of the Earth and the real observational data obtained from the Deep Space Climate Observatory (DSCOVR) by Fan et al. (2019). For comparison, we solved the mapping problem using both Tikhonov regularization and sparse modeling, and discuss the difference in the output maps.

5.1 Formulation of the mapping

5.1.1 Forward and inverse modeling of planetary scattered light

For the global mapping, we adopt the formulations in Section 2.2.3 assuming the the planetary surface albedo $\boldsymbol{m}$, discretized to $N_{\rm pixel}$ pixels ($\boldsymbol{m} = \{m_j = m(\theta_j, \phi_j)\}$ for $j = 1, 2, ..., N_{\rm pixel}$), where (θ_j, ϕ_j) is the location of the jth pixel on the sphere's surface. The scattered light curve $\boldsymbol{d}$ consists of $N_{\rm data}$ points ($\boldsymbol{d} = \{d_i = d(t_i)\}$ for $i = 1, 2, ..., N_{\rm data}$), where t_i is the ith time frame. The planetary surface albedo and light curves are connected by the relation $d_i = \sum_j^{N_{\rm pixel}} G_{i,j} m_j + \epsilon_i$ in Eq (2.20) with a transfer matrix $\boldsymbol{G} = \{G_{i,j} = G(\theta_j, \phi_j; \Phi_i, \Theta_i; \zeta, \Theta_{\rm eq})\}$ for $i = 1, 2, ..., N_{\rm data}$ and $j = 1, 2, ..., N_{\rm pixel}$. The transfer function $\mathbf{G}$ has two fundamental timescales, associated with the spin and orbital periods. Combinations of these timescales allow the consideration of different positions on the planetary surface at different epochs. The inversion method exploiting this property is called SOT (see more detailed discussions in Kawahara & Fujii, 2010, 2011; Fujii & Kawahara, 2012).

For solving $\boldsymbol{m}$, one approach would exploit the Tikhonov regularization, and it can be solved analytically as in Eq (2.23) and (2.24). In fitting, we assume spin parameters $(\zeta, \Theta_{\rm eq})$ to be those of the Earth for the simplicity, but they can be also estimated from the light curves. Such constraints will give unique information in the architecture of exoplanetary systems.

Alternatively to Tikhonov regularization, we consider sparse modeling, which involves the combination of the L1-norm and Total Squared Variation (TSV) introduced in Kuramochi et al. (2018) as the regularization terms for mapping planets. Then, the loss function $Q_{l1,{\rm tsv}}$ is given by

$$Q_{l1,{\rm tsv}} = \sum_{i=1}^{N_{\rm data}} \frac{(d_i - \sum_{j=1}^{N_{\rm pixel}} G_{i,j} m_j)^2}{\sigma_i^2} + \Lambda_l Q_l + \Lambda_{\rm tsv} Q_{\rm tsv}, \tag{5.1}$$

$$Q_l = \sum_i^{N_{\rm pixel}} |m_i|, \tag{5.2}$$

$$Q_{\rm tsv} = \sum_i^{N_{\rm pixel}} \sum_j^{N_{\rm pixel}} \frac{1}{2} W_{i,j} (m_i - m_j)^2, \tag{5.3}$$

where $W_{i,j}$ is the neighboring matrix defined as

$$W_{i,j} = \begin{cases} 1 & \text{if } i\text{-th and } j\text{-th pixels are adjacent.} \\ 0 & \text{otherwise.} \end{cases}$$

In Eq (5.1), Λ_l and $\Lambda_{\rm tsv}$ are the regularization parameters of L1 and TSV, respectively. The second term $\Lambda_l Q_l$ describes the sparsity of the solution. The larger value of Λ_l gives more zero-valued pixels in the solution. The third term $\Lambda_{\rm tsv} Q_{\rm tsv}$ in Eq (5.1) is defined as the sum of the difference in the values of adjacent pixels. This term determines the smoothness of the solution. We solved the minimization of $Q_{l1,{\rm tsv}}$ with a monotonic variant of the fast iterative shrinking threshing algorithm (MFISTA; Beck & Teboulle (2009a,b)), following Akiyama et al. (2017a) and Kuramochi et al. (2018).

5.1.2 Choices of regularization parameters in inverse modeling

The optimization of regularization parameters is important issues in statistical methods, but the general discussion for the selection is difficult. In the global mapping problem with the Tikhonov regularization, Kawahara & Fujii (2011) proposed to use l-curve method, which determines the optimal solution as the maximum curvature point of the model norm versus residuals corresponding to χ^2 (Hansen, 2010). Following their method, we adopt the l-curve in this chapter to find the optimal regularization parameters for the Tikhonov regularization.

In case of the sparse modeling with the combination of L1-norm and TSV, however, l-curve method cannot be applied straightforwardly because there is one additional regularization term. One might be able to extend l-curve to the higher-order method, but this is beyond the current scope of this work as there is no such previous study in the field of sparse modeling. Another possibility is the cross validation method, where the data are split into training and validation data, and the trained model is evaluated against the test data. However, this method favors the overfitted solution in the global mapping as discussed in Section 5.2.

One possible strategy is to train regularization parameters by simulating several configurations, and apply the trained optimal regularization parameter to the real data (e.g. Event Horizon Telescope Collaboration et al., 2019). In the case of global mapping, we firstly prepare different land distributions, simulate the observational data for the models, recover the maps from the simulated data, and choose the acceptable regularization parameters by comparing the recovered maps with the ground-truth images. Finally, one will recover the map from the real data by adopting the regularization parameters, which are determined by the inject and recovery tests in the above. Given this procedure in mind, we focus on studying the potential of the sparse modeling here; specifically, we attempt to investigate whether there exist possible combinations of regularization parameters in sparse modeling that recovers the better map than the Tikhonov regularization by comparing them with the ground-truth map of the Earth. On the other hand, we put aside the discussion on the optimization of regularization parameters for the future consideration.

5.2 Mapping the cloudless Earth

As a test bed, we adopt a static cloud-subtracted Earth model, as used in Kawahara (2016). Figure 5.1(a) shows this injected albedo map of the Earth after removal of the cloud-cover fraction with ISCCP D1 data (the cloud map of 2008 Jun 30 21:00). On this map, the ocean has zero albedo and land has a constant albedo after subtracting the cloud coverage. The spherical pixelization was realized using Hierarchical Equal Area Iso Latitude pixelation of the sphere (HEALPix) (Górski et al., 2005) with 3072 pixels in total. With regard to the TSV terms, we calculated $W_{i,j}$, referring to the orders of pixels on the sphere. Concerning the geometry and orbital parameters, we assumed $i = 0°$, $\zeta = 90°$, $\Theta_{\rm eq} = 180°$, $P_{\rm spin} = 23.93447$ hours, and $P_{\rm orb} = 365.24219$ days. We generated a one-year light curve with 1024 points at $\simeq$8 hours interval, and we added Poisson noise to the light curves by varying S/N= $2, 5$. In the analysis, we adopted "Tikhonov" and "L1-norm+TSV" regularization terms respectively for comparison. Figure 5.1(b) shows the mean weight of $G_{i,j}$ over the Earth surface in this mock observation. The Earth surface was globally surveyed except for the regions very close to the North and South poles.

Figure 5.1(c)-(f) shows the recovered maps estimated from the light curves with S/N=2 or S/N=5 with the "Tikhonov" and "L1-norm+TSV" regularization terms. The chosen regularization parameters are $\lambda = 19.3$ in the case S/N=2 and $\lambda = 10.0$ in the case S/N=5 according to the l-curve criterion (Hansen, 2010) for Tikhonov regularization. For "L1-norm+TSV" regularization, we set $(\Lambda_l, \Lambda_{\rm tsv}) = (10^{-0.50}, 10^{-0.25})$ in the case S/N=2 and $(\Lambda_l, \Lambda_{\rm tsv}) = (10^{-0.25}, 10^0)$ in the case S/N=5 as the optimal solutions determined by the comparison with the ground-truth map.

Both methods, in cases of S/N=2,5, generally succeed in recovering the major continents. However, as is evident from the comparison with the input map, Figure 5.1(d,f) shows better resolved and more consistent maps than Figure 5.1(c,e); the detailed structures of the continents (e.g., the shapes of South America and Africa) are well reproduced in Figure 5.1(d,f). This tendency is more clearly seen in the comparison with S/N=2. The Tikhonov regularization (Figure 5.1(e)) fails to discriminate North and South America or the the Eurasian Continent and the Australian Continent. In contrast, sparse modeling (Figure 5.1(f)) successfully distinguishes these continents with well characterized coastlines. We note that the smaller λ value gives a higher resolution with Tikhonov regularization, albeit with an over-fitted inferred map and induced noise.

Differences among the reconstructed maps originate from various aspects. Tikhonov regularization is not physically motivated by the nature of the planetary surface. This term acts as a regulator for observational noise and the spatial resolution of the surface (Kawahara & Fujii, 2011). In contrast, the L1-norm efficiently identifies ocean regions because their albedo is zero. In addition, the TSV term suppresses the emergence of the bumpy structures on the maps, and the recovered maps become smoothed as a result of the minimization.

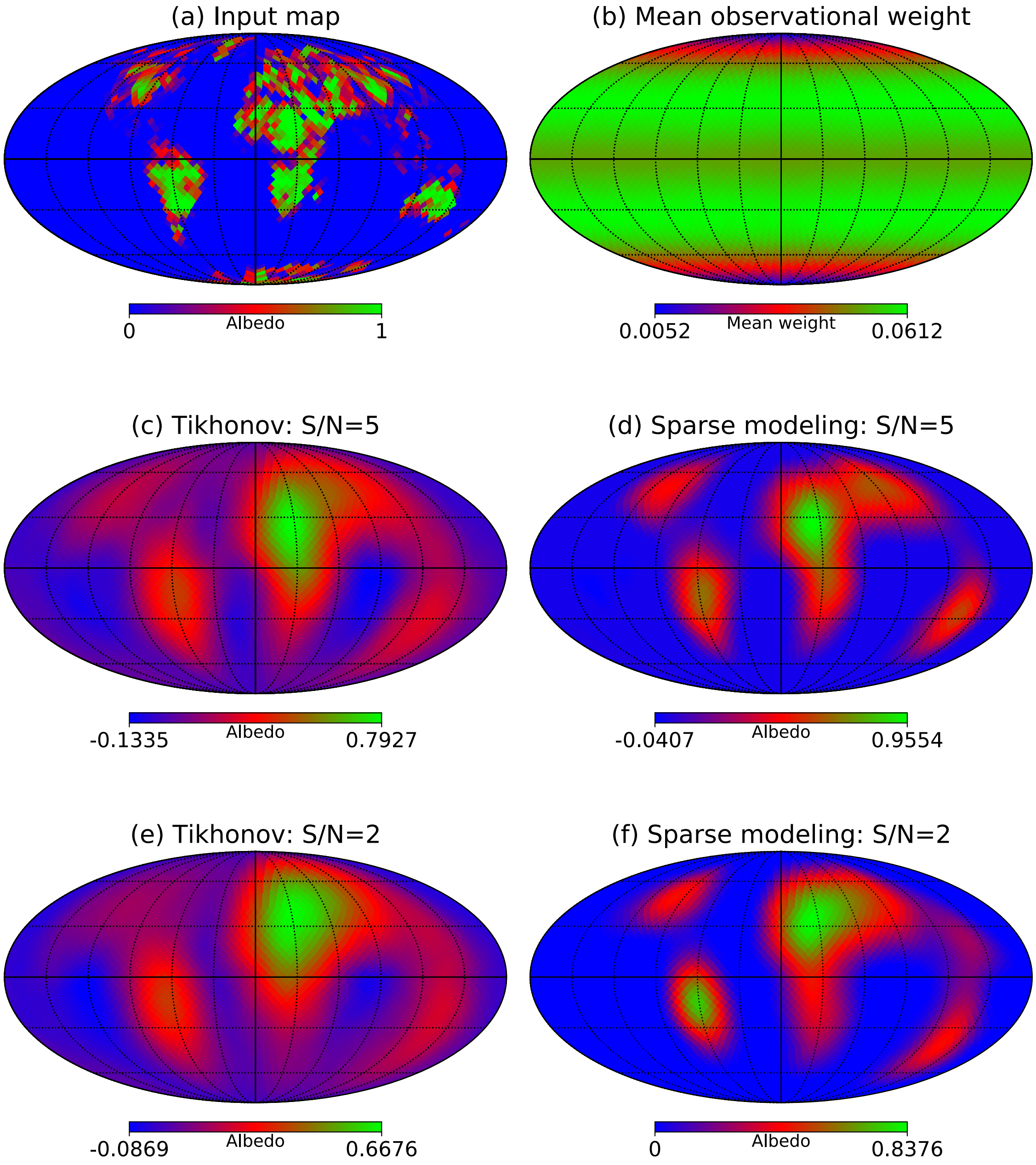

Figure 5.1 Mock albedo map of the Earth and the recovered surface estimated from the lightcurves with S/N=2, 5. (a) Injected albedo map of the Earth. (b) Annual mean of the observational weights $G_{i,j}$ of the mock data. (c) Recovered map based on Tikhonov regularization (S/N=5). (d) Recovered map with S/N=5 based on regularization of the L1-term an TSV. (e) Same as (c), but for S/N=2. (f) Same as (d), but for S/N=2.

We also compare the cross validation and l-curve method for recovering the maps in the Tikhonov regularization. For that purpose, we adopt the same light curve and geometrical configuration as used in case of S/N=5 in the above. The panel (a) in Figure

5.2 shows the deviations of recovered maps from the ground truth map depending on the regularization parameter λ. Blue point corresponds to the map closest to the ground truth map, the black point is obtained from the cross validation panel (c), and the red point is determined by the l-curve method in panel (e). The panels (b), (d), and (f) correspond to the recovered maps obtained from the comparison with the ground truth map, the cross validation, and l-curve method, respectively. For the cross validation, we adopt 10-fold for splitting the data by the random selection, and compute the root mean squared errors by exploiting trained models and the test data. The comparison demonstrates that the cross validation gives the overfitted map, and it is fairly deviated from the ground truth map. In addition, root mean squared errors in the cross validation are significantly insensitive to λ, implying that the method is not suitable for the global mapping. On the other hand, the l-curve method returns the map close to the best possible map by comparison with the ground truth map.

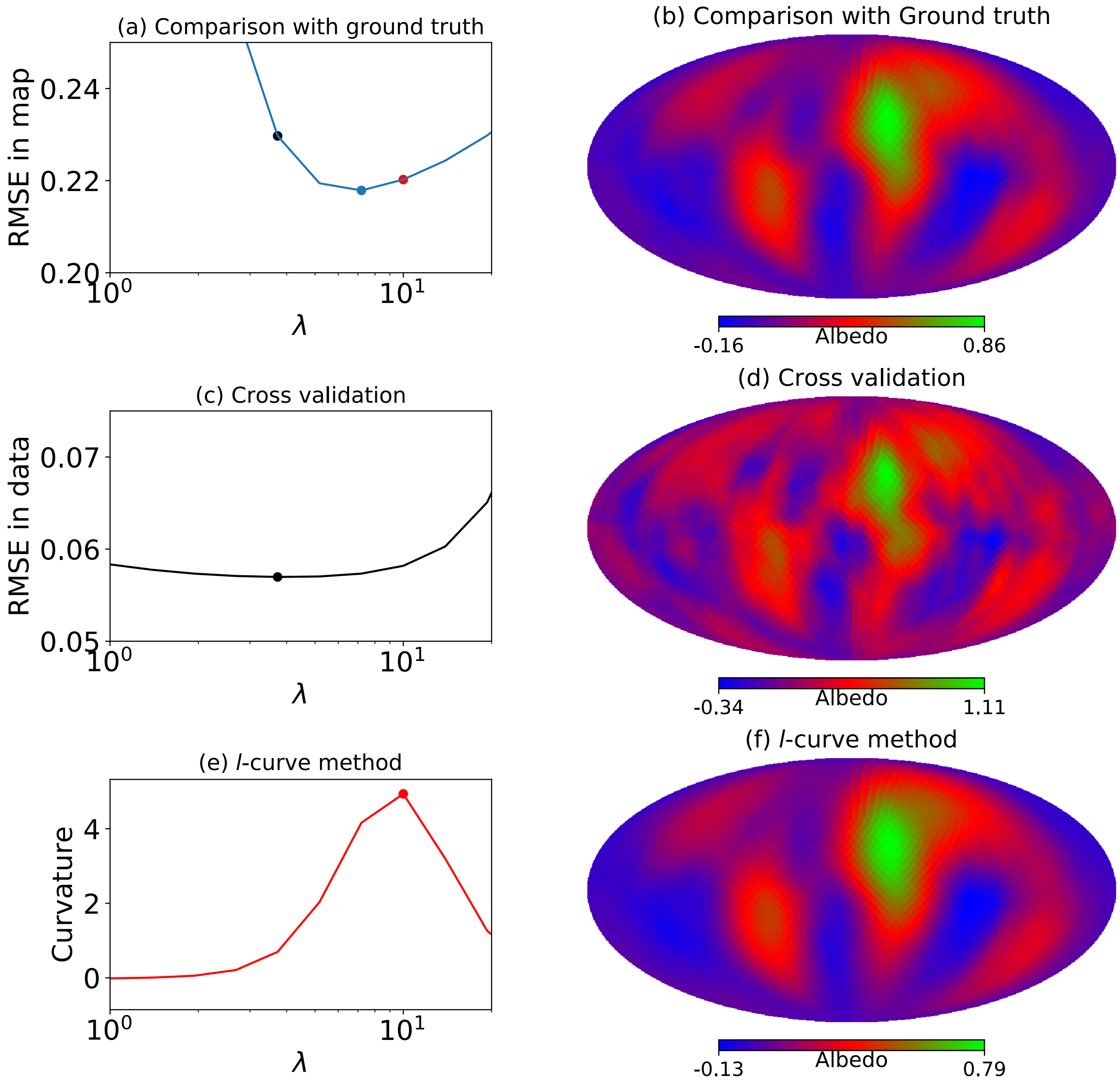

Figure 5.2 Comparison of recovered maps from the lightcurves with S/N=5 in Tikhonov regularization . Blue, black, and red points correspond to optimal maps in panel (b), (d), and (f), respectively. (a) Root mean squared errors (RMSE) between recovered maps and ground truth map. (b) Recovered map obtained from comparison with ground truth map. (c) Root mean squared errors in cross validation. (d) Recovered map obtained from comparison with ground truth map. (e) Curvature exploited in l-curve method. (f) Recovered map obtained from l-curve method.

5.3 Application to observed light curves

Recently, Fan et al. (2019) reproduced the surface map of the Earth using real light curve observations of ∼10,000 DSCOVR/EPIC frames collected over a two-year period. Observations were taken in 10 optical narrow band channels, and the principal components (PCs) were calculated among all the light curves to extract the surface feature. The second PC (PC2) was found to trace the surface inhomogeneity with a strong linear correlation. The Earth surface map was estimated from that light curve using Tikhonov regularization, following Kawahara & Fujii (2011). Figures 5.3(b)-(c) show the mean weight matrix of the observation obtained by the Earth Polychromatic Imaging Camera (EPIC) onboard DSCOVR and the corresponding recovered map, respectively. This observation is fairly insensitive to the north and south poles because DSCOVR is always located near the first Lagrangian point between the Earth and the Sun. In their solution, they adopted $\lambda = 10^{-1.5}$ as the regularization parameter in Eq (2.22). Their estimation (Figure 5.3(c)) captured the coarse features of the Earth surface, but not all the continents were successfully recovered (e.g., South America and Australia).

For comparison, we solved the same problem using the L1-norm and TSV regularization terms The light curves have negative and positive values owing to the nature of the principal component. In the solution derived by Fan et al. (2019), the regions with negative PC2 are more likely to be ocean. To make efficient use of sparsity, i.e., to associate zero values to ocean regions, we produced the non-negative light curves by subtracting the minimum value of the light curves from the overall light curves, and slightly offsetting the entire data set by 0.005. This ad hoc operation, or the choice of the added constant, does not significantly affect the results because the constant offset in the light curve would only result in a constant change to the whole recovered map. Figure 5.3(d) shows the recovered map, based on the L1-norm and TSV regularization. We adopted $\Lambda_l = 10^{-3}$ as the regularization parameter and $\Lambda_{\mathrm{tsv}} = 10^{-3}$ in Eq (5.1) as the optimal solution chosen by comparison with the ground-truth map. Notably, the mapping by the new regularization term resolves the structure of South America and Australia, which are blurred and connected to Antarctica in Figure 5.3(c). It also successfully resolves other continents very consistently with the features of the Earth surface. However, our newly proposed map does not recover Antarctica as implied in Figure 5.3 c. This may be due to its low observational weights (Figure 5.3(b)) and different spectral features than other continents.

Finally, we show solutions with 9 different combinations of $\Lambda_l = (10^{-4}, 10^{-3}, 10^{-2})$ and $\Lambda_{\mathrm{tsv}} = (10^{-4}, 10^{-3}, 10^{-2})$ in Figure 5.4. Toward the larger value of Λ_l, the reconstructed maps become more sparser, and inconsistent with the ground truth. On the other hand, with smaller value of Λ_l, the solutions become more similar to those obtained from the Tikhonov regularization (Figure 5.3(c)). The optimal solution with $(\Lambda_l, \Lambda_{\mathrm{tsv}}) = (10^{-3}, 10^{-3})$ is exactly in the middle of these two kinds of solutions, and the three cost functions in $Q_{l1,\mathrm{tsv}}$ balance each other at this point.

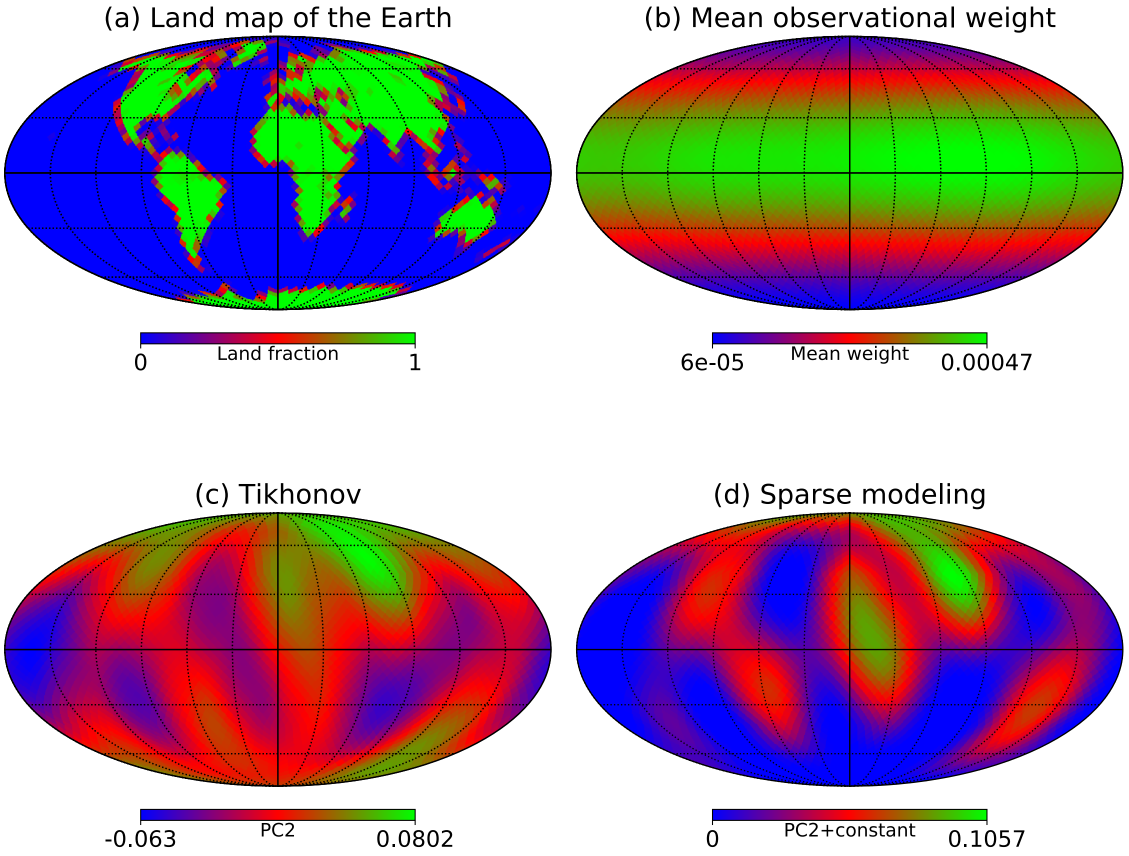

Figure 5.3 Mapping the surface of the Earth using the 2-year DSCOVR/EPIC observations. (a) Ground truth of pixelated land fraction surface map of the Earth (Fan et al., 2019). (b) Annual mean of the observational weights $G_{i,j}$ in the 2-year DSCOVR/EPIC observations. (c) Recovered map with Tikhonov regularization derived by Fan et al. (2019). (d) Recovered map with regularization of L1-norm and TSV. The ligth curves of PC2 are offset by a constant value descried in Section 3.

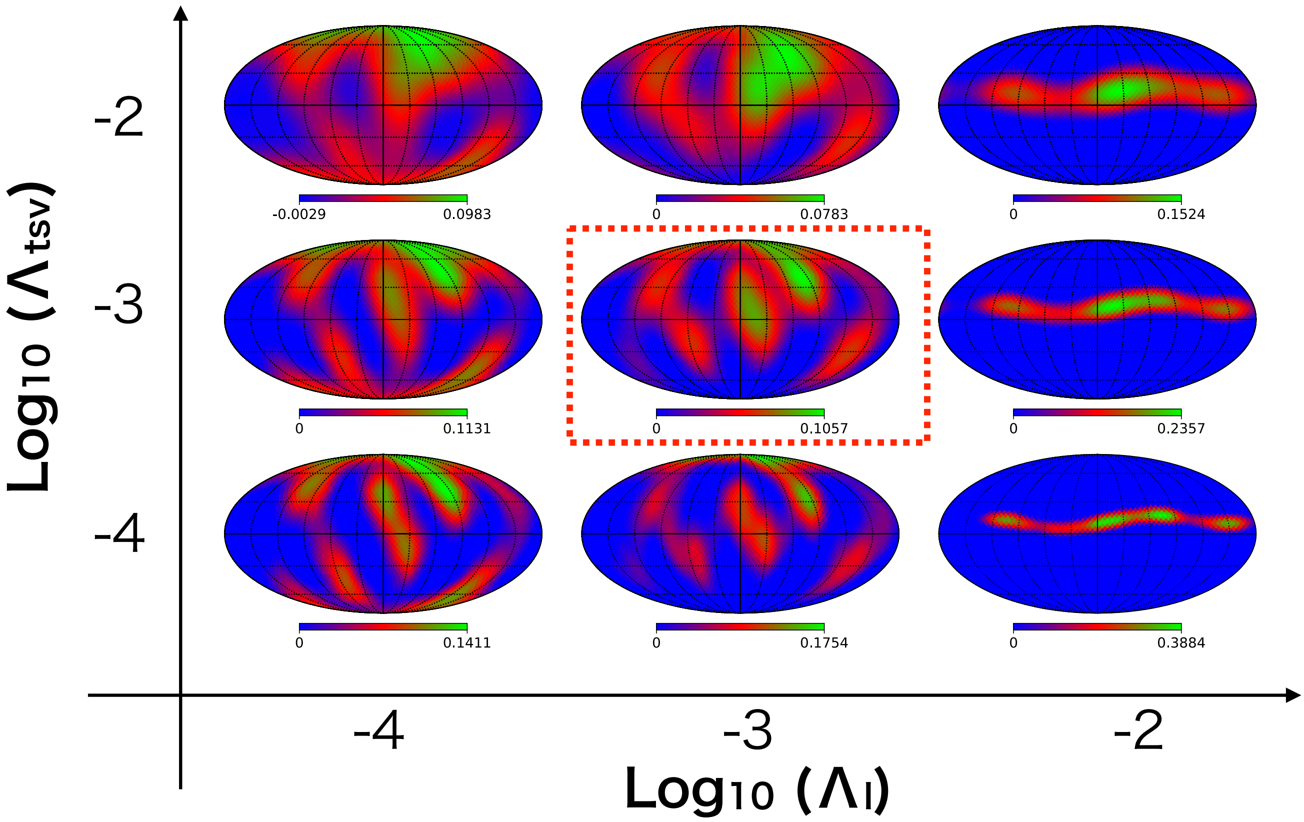

Figure 5.4 Recovered surface maps with different combinations of $\Lambda_l = (10^{-4}, 10^{-3}, 10^{-2})$ and $\Lambda_{\rm tsv} = (10^{-4}, 10^{-3}, 10^{-2})$. The optimal solution is shown in the center of the panel being surrounded by red dotted lines.

5.4 Demonstration of global mapping in future observation

In the future space direct imaging observations (e.g. the Habitable Exoplanet Observatory (HabEx) and the Large UV/Optical/IR Surveyor (LUVOIR)), it would be unrealistic to have continuous occupancy of an instrument for years. In addition, the instrumental and astrophysical noises in actual exoplanet observations would be orders of magnitude larger than those in Earth's light curves. It is necessary to take the consideration of much less time frames and higher noise level for exoplanet observations. In this section, we test the feasibility of the method under a more realistic assumption.

As a fiducial system, we consider an Earth size planet around a Sun-like star with T = 5780 K ($T_\odot$) and $R_\star = R_\odot$ at a distance of 10 pc. The semimajor axis of the planetary orbit is assumed to be 1 AU, and the planetary flux in each band is calculated by convolving the planet's reflectivity with the stellar spectrum. For simplicity, we assume the reflection to be Lambertian, and the phase angle α is asssumed to be 90°, where the planet is at a quadrature. We consider a HabEx-like telescope with a diameter $D = 4m$. The coronagraph design contrast is assumed to be 10^{-10}, and the end-to-end throughput is taken to be 0.3 in the coronagraph or starshade instrument. The integration time is 1.8 hours, which corresponds to the average time interval in the current observation. For simplicity, we consider the snapshot of each image rather than the smeared image with 1.8 hours integration.

We calculate the observational noises using `coronagraph`, which is an open source Python package for computing the noise of space direct imaging missions (Robinson et al., 2016; Lustig-Yaeger et al., 2019). Adopting the imaging mode in `coronagraph`, we compute S/N in each band. As the DSCOVR observation uses narrow-band filters (317, 325, 340, 388, 443, 552, 680, 688, 764 and 779 nm), we reassign the band centers and full width at half maximum (FWHM) to emulate broadband filters of our mock observatory. For instance, we take the average of the light curves in three narrow-band filters of DSCOVR (317, 325, and 340 nm) as the light curve in a single band. In the similar manner, we combine the light curves in the filters with band centers of (680 and 688 nm) and (764 and 779 nm) by averaging their light curves. As a result, we have the light curve with six broadband filters with band centers = (325, 388, 443, 552, 684, 770 nm) and FWHM = (30, 33, 22, 87, 45, 41 nm).

Figure 5.5 shows the compositions of the noise sources based on Robinson et al. (2016). The calculation is basically based on the sample code “luvoir_demo.py" in `coronagraph`. The noise sources are composed of Poisson noise, local zodiacal light, exozodiacal light, dark current, read noise, and speckle noise. In the current case, the dominant noise sources are Poisson noise and the background emission from zodiacal and exozodiacal light. In the reconstructed broadband filters, we find S/N = (1.36, 1.82, 1.69, 2.66, 1.42, 1.29) assuming 1.8 hours integration.

Instead of a continuous 2-year observation, we assume multi-epoch observations as those presented in Schwartz et al. (2016) and Farr et al. (2018). We divide 1 year into 12 blocks ($\simeq$ 1 month), and use the first $D_{\mathrm{obs/month}} = 1$ or 5 days in each block. Adopting S/N as above, we inject Gaussian noise to the light curves, and decompose them into principal components using the singular value decomposition (SVD). As revealed in Fan et al. (2019), the second strongest principal component (PC2) is linearly correlated with the land fraction; the coefficient of determination r^2 is 0.91 in their paper. Figure 5.5 shows the scatter plot of PC2 and the land fraction in case of $D_{\mathrm{obs/month}} = 5$ days with $r^2 = 0.51$, which implies the weak correlation. Similarly, we find $r^2 = 0.49$ and 0.52 for $D_{\mathrm{obs/month}} = 1$ day and the full data. On the other hand, we find $r^2 = 0.93$ without the injection of noise, so the noise would account for the weak correlation in the current case. Finally, we fit a linear function of the land fraction to the PC2, and we add an offset to PC2 to normalize the land fraction to be zero when PC2 = 0.

Figure 5.6 shows the recovered surface maps using Tikhonov regularization and sparse modeling. Even 1 day in each block is sufficient to retrieve the planetary surfaces, and the sparse modeling succeeds in separating North and South America continents from each other. Observations with $D_{\mathrm{obs/month}}$ of 5 days enable us to recover the maps with very similar accuracy to those produced from continuous observations. These results encourage the mapping of “Second Earth" using future directly imaging missions such as HabEx and LUVOIR.

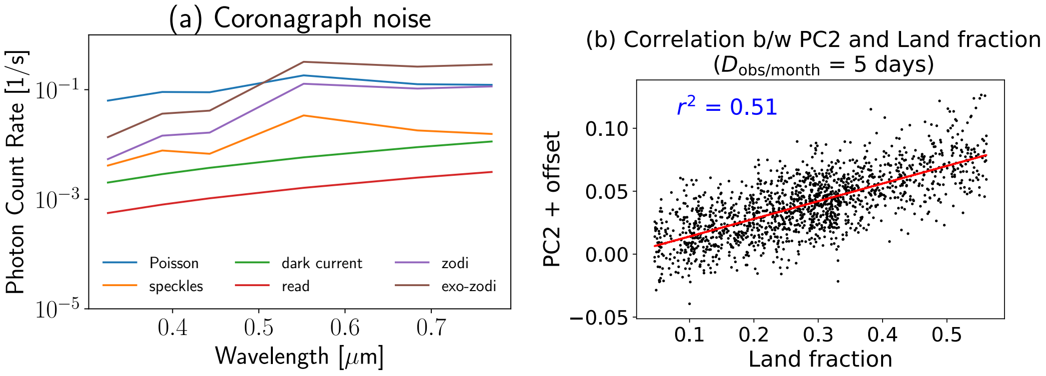

Figure 5.5 (a)Statistical noises in the unit of photon counts derived by `coronagraph` (Robinson et al., 2016; Lustig-Yaeger et al., 2019). (b) Scatter plot of land fraction and PC2 extracted from light curves with $D_{\rm obs/month} = 5$ days. Red line shows a linear fitting to the data, and the coefficient of determination $r^2 = 0.51$.

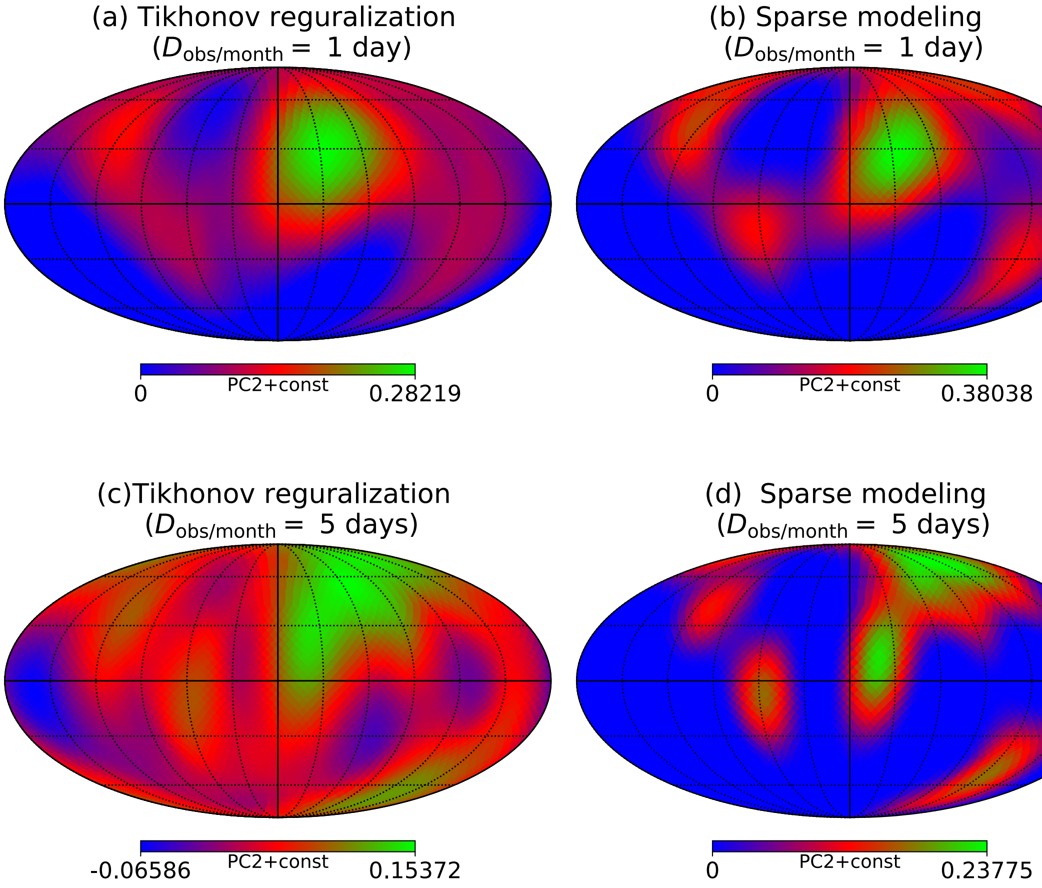

Figure 5.6 Global mapping of the DSCOVR data assuming observations from a distance of 10 pc using Tikhonov regularization (a,c) and Sparse modeling (b,d). The solution with the sparse modeling in panel (b) uses $(\Lambda_l, \Lambda_{\mathrm{tsv}}) = (10^{-4.5}, 10^{-3.5})$, and panel (d) uses $(\Lambda_l, \Lambda_{\mathrm{tsv}}) = (10^{-4.0}, 10^{-3.5})$. The data in the first $D_{\mathrm{obs/month}} = 1, 5$ days in each month are used to recover these maps. For clarity of the map, we intentionally set the minimum values to be 0 in panels (a) and (b).

5.5 Summary

The use of reflected light curves for mapping surfaces is an important probe of exoplanet surface inhomogeneity. Previous studies of recovering surface maps from observed light curves only regularized observational noise with Tikhonov regularization (the L2-norm) without the consideration of physical properties of planetary surfaces. In this chapter, we introduced sparse modeling (L1+TSV regularization) to estimate a planetary surface efficiently by exploiting the surface properties, (a) distinct spectral difference between land and ocean and (b) continuity of planetary surfaces. As a test calculation, we injected and recovered the mock albedo map of the Earth using both regularization terms, and found that sparse modeling reproduces more consistent continental surface distributions. We also applied our method to observations of the Earth obtained by DSCOVR to investigate the advantage of sparse modeling in real data analysis. We found that sparse modeling successfully recovers the continents (Australia and South America) that are not clearly estimated by Tikhonov regularization. We also showed that 1 or 5 days per month in 2-year observation is sufficient for retrieving the surface map of an Earth analog at a distance of 10 pc.

In this chapter, we demonstrate that the choice of regularization terms in exoplanet mapping can significantly affect the resulting recovered maps. Our current demonstration remains limited to the combination of the configuration of the Earth and the L1 + TSV term. Although we demonstrate the potential of the sparse modeling with specific regularization parameters, the selection of such optimal regularization parameters is another problem. This would require the validation methods including the inject and recovery training with several different continents.

Chapter 6

Summary and Future Prospects

6.1 Summary

In this thesis, we focus on observational aspects of exoplanetary and stellar systems by exploiting current (ALMA and Kepler) and future instruments (LUVOIR and HabEx). The significant findings and attempts in each chapter are summarized as follows:

Chapter 3

- We intensively search for exoplanetary rings around the 168 Kepler planets, whose light curves would allow the detection of Saturn-like rings. Most of planets have short orbital periods, and the expected composition of ring particles is rock rather than ice. In this sense, this search is complementary to the previous search around long-period planets (Aizawa et al., 2017), and significantly improved over the previous search around short-period planets (Heising et al., 2015).
- Although we identify 29 tentative systems, where the ring model is statistically preferred over the ringless model, none of the signatures turn out to be robust after inspecting the light curves in detail. These false positives (e.g. stellar spots, evaporating planets) are useful for the future search for rings.
- The null results put upper limits on the size of possible rings, and using the sets of constraints, we demonstrate that the occurrence rate of exoplanetary rings larger than twice the planetary radius should be less than 15 %. Although the majority of planets are very different from the Solar System, our search provides the quantitative constraint on the ring formation and evolution in exoplanetary systems.

Chapter 4

- We systematically search for the evidence of alignment of proto-planetary disks in five nearby star-forming regions. In the analyses, we mostly exploit the ALMA observations of them to determine their geometry.

- We find that PA distributions are well described by the uniform distribution in four regions other than Lupus region, and this is basically consistent with the turbulent nature of angular momentum. On the other hand, we identify the possible signature of the alignment in the Lupus III at the statistical significance of 2σ, and it might imply other mechanisms for generating angular momentum beyond turbulent motions.

- We also confirm the robustness of observed disk geometries in the Lupus region by comparing different methods for extracting disk's geometry (CLEAN+imfit, uvmodelfit, and sparse modeling). Although the sparse modeling significantly resolves the substructures of disks, it does not give the significant improvement on the estimations of position angles and inclinations compared with other methods.

- We find the alignment among disks in the Orion Nebular Cluster, but it turns to be likely a false positive after inspecting details of calibrations for the interferometric observations. Specifically, the systematic errors in the observation make disk images stretched in a certain direction so that the apparent alignment is produced. This effect becomes significant for marginally resolved disks, and it should be carefully addressed for the robust discussion of the alignment.

Chapter 5

- We propose to exploit a sparse modeling in global mapping of an Earth analog from its scattered light curves. We find that the sparse modeling potentially recovers the better resolved map than the Tikhonov regularization in case of the cloudless Earth. We also apply the sparse modeling to the real scattered light curves of the Earth, and we demonstrate that the method can separate the the Australian continent and the South American continent, which cannot be resolved in the reconstructed map using Tikhonov regularization.

- We also attempt to recover the surface map from noise-injected light curves by assuming an Earth analog at a distance of 10 pc. We find that the multi-epoch observation for 1 day per month can reconstruct the main surfaces of an Earth analog in future direct imaging missions such as HabEx or LUVOIR. This demonstrates the feasibility of global mapping in realistic situations with limited observational duration.

The methodology of search for rings presented in Chapter 3 will be applicable to other observations including TESS (Transiting Exoplanet Survey Satellite). The constraint on the ring frequency gives a quantitative information on ring formation complementary to the knowledge in the Solar System. In Chapter 4, we find that disk orientations are likely to be random in four regions out of five, and it is consistent with the turbulent nature of angular momentum. On the other hand, we find the possible alignment in the Lupus III at 2σ level, and it might require mechanism beyond turbulence. Additionally, we find the apparent alignment in ONC, but it is likely to be a false positive due to systematical noises. On the other hand, we demonstrate that the sparse modeling is potentially useful in global mapping of an Earth analog in the future observations in Chapter 5. Furthermore, we show that intermittent observations even with a cadence of one month allow the global mapping assuming a planet at a distance of 10 pc.

Chapter 4 and Chapter 5 have the connection to each other in viewpoints of the application of the sparse modeling, and the further studies would be rewarding. In addition, Chapter 3 and Chapter 5 commonly present the methodologies for identifying Solar-System counterparts in the exoplanetary systems: exorings and exosurfaces. Additionally, all of chapters attempt to give new light on the architectures of exoplanets: planetary spins and alignment among planetary systems and/or proto-planetary disks. They are complementary to previous discussions on spin-orbit misalignment, and will give unique information of planetary formation. In summary, the works in this thesis present previous unconventional viewpoints, and they will be helpful for further understanding of origin, formation, and evolution of planetary systems including the Solar System.

6.2 Future Prospects

Finally, we briefly discuss the possible future directions for each topic addressed in this thesis: search for planetary rings in the future, investigation into alignment among disks or cores and its implication, and further application of sparse modeling in astronomy.

6.2.1 Search for exoplanetary rings using transit method in the future

We have intensively searched for planetary rings using the Kepler data, so the next possible direction would be exploitation of other data including TESS, which basically observes the full sky. The promising targets for the ring search would be cold long-period planets like Saturn, but the short-period planets would be also be valuable to be explored if rocky rings generally exist. The typical observational duration of the TESS is one month, so the main targets in the ring search would be short-period planets with possible rocky rings. On the other hand, the particular sectors have been observed for more than one month, so it is still promising to search for icy rings around long-period planets.

Long-period planets can be also identified in long baselines achieved by combinations of current and future photometric observations including Kepler, TESS, CHaracterizing ExOPlanets Satellite (CHEOPS), and PLAnetary Transits and Oscillations of stars (PLATO). Recently, the collaboration of the Kepler mission and TESS has yielded the detection of Jupiter-sized planet HIP41378 f with $P = 542$ days (Santerne et al., 2019), and this demonstrates the feasibility of the method in the future.

In addition, a ring significantly increases the apparent size of the planet, and this leads to the underestimation of planetary density, which can be the indirect evidence of the ring system (Zuluaga et al., 2015). In reality, there is a class of the extremely low dense super Earth planets, so called Supper Puffs, and they might be explained by the ringed planets rather than the single planet (Piro & Vissapragada, 2019). Another interesting example is HIP41378 f with the extremely small density (0.09 ± 0.02 g cm^{-3}), and it can be explained by the ringed planet (Santerne et al., 2019). The small planetary density is the just the indirect evidence of the possible ringed planet, and additional analyses and observations are necessary to prove or reject the ring hypothesis. One way is to search for the anomalies in light curves caused by rings as investigated in this thesis, although it requires the exquisite photometric precision. Another way is to exploit multi-band observations of transit light curves, whose shapes potentially change depending on wavelength due to chromatic scattering and absorption by ring particles (e.g. Barnes & Fortney, 2004). Especially, the exoplanets discovered by TESS are comparatively close to the Earth, so it practically allows for the follow-up observations of transit light curves in other telescopes.

6.2.2 Exploration of alignment of disks and cores and its implication

In Chapter 4, we explore the disk-disk alignment by exploiting previous observations and literature, but as demonstrated in Section 4.5, the marginally resolved disks are susceptible to systematic noises, which can produce the apparent alignment. To evade such false positive, it will be useful to implement a simulation for systematical observations of proto-planetary disks with help of the CASA task `simalma` (McMullin et al., 2007) so that we can quantify to what extent we can recover the possible alignment from the noisy observation. Such attempts can be also essential for determining correct size of disks in systematical survey. On the other hand, the current ALMA data for ONC used in this thesis is largely susceptible to observational errors, and the additional observation will be essential for investigating the region further.

We can also extend the disk alignment to that among molecular cloud cores in star-forming regions. The rotational axes of stellar cores can be constrained by the measurements of Doppler shifts of the molecular lines (e.g. N_2H^+), and we can naturally apply our methodology to their estimated directions of rotations. Previously, Tatematsu et al. (2016) gave estimations of directions of axes of angular momentums for 34 dark cores in Orion A cloud, whose average mass of cores is $45.7 M_\odot$ (Tatematsu et al., 2008). They implicitly pointed out that the core orientations in the upper cloud are preferentially directed toward the east direction, which is still inconsistent with the global rotation of the cloud. We can similarly pursue the alignment among cores by exploiting several searches for cores in previous literature (Caselli et al., 2002; Pirogov et al., 2003; Chen et al., 2007; Tobin et al., 2011; Tatematsu et al., 2016; Chen et al., 2019), and such studies would be complementary to our current work.

On the other hand, the origin and implication of the alignment are still unknown, and the further exploration is rewarding. One possibility is a global rotation of a molecular cloud (Corsaro et al., 2017; Kuznetsova et al., 2019), but we do not find the large rotation in Lupus III. We are now analyzing the simulation data presented by Chen & Ostriker (2015), which tracked the core formation and evolution in the colliding convergent flows in molecular clouds. Their simulations consider magnetic fields, which are ignored in previous studies, so the results are complementary to the previous studies. We will report the results in the future.

6.2.3 Further application of sparse modeling

In this thesis, we explore the possibility of the sparse modeling in imaging of protoplanetary disks and global mapping of an Earth analog in future direct imaging observations. Beyond these attempts, further application and extension are rewarding. One natural application of sparse modeling would be identification of sub-structures of protoplanetary disks by exploiting the better effective angular resolution achieved the method. The structures of interest include the gap structures (e.g. ALMA Partnership et al., 2015), spiral structures (e.g. Pérez et al., 2016), bright arcs (e.g. Pérez et al., 2018), and misaignment in warped disks (e.g. Sakai et al., 2019). The typical enhancement of the angular resolution by sparse modeling is a few times (e.g. Honma et al., 2014), and the reanalyses of the data will potentially reveal the hidden structures of disks in existing data.

We can also extend usage of the sparse modeling to mapping of stellar spots on stellar surfaces. Periodic variations in light curves can be due to the apparent motions of stellar spots by the stellar rotations, and we can inversely solve the distributions of spots from the variations (e.g Walker et al., 2007). Stellar spots can be assumed to have zero luminosity in the estimation, we can naturally apply the sparse modeling to the light curves for the inference. Such attempts would also constrain not only the properties of stellar spots but also the stellar inclinations of stars, which are important for characterizing the planetary architectures as well.

In addition to the mapping of stellar spots, the methods for global mapping can be also improved in several points. The introduced regularization in this thesis is not unique, and one can also attempt other combinations, including L1, L2, TSV, and Total Variation (TV) terms, to search for optimal regularization terms. In choosing the optimal regularization parameters for the sparse modeling in the future observations, we suppose that we train the parameters by injecting and recovering different models as in Event Horizon Telescope Collaboration et al. (2019), but one might be able to extend the l-curve method to the three dimensional space (e.g surface curvature). One can also improve the method for global mapping to reconstruct a 2d “color” map of the exoplanetary surface from multi-band observations. Previously, Fujii et al. (2017) pointed out that there exist the degeneracy between surface types and their spatial distributions, but one can also exploit some regularization terms to suppress the number of surface types for solving the degeneracy. In the real scattered light curves, the clouds can be significant sources of systematic noises in mapping, so the methods for handling them should be seriously explored. In summary, it will be rewarding to pursue the complete methodology for recovering the 2d map of a colored Earth assuming the future observations.

Acknowledgement

First of all, I wish to express my sincere gratitude to my supervisor, Yasushi Suto, for his continuous support and encouragement. He directly or sometimes indirectly has taught me about a lot things: open-mindedness, how to choose research topics, how to survive the tough times, skills of critical thinking, and how to take balance between details and big pictures. In addition, he always took the precious time to give me advices whenever I wanted, and gave me a lot opportunities to deepen and expand the researches in various ways. These experiences and skills will be useful and encouraging for the rest of my life in a broad sense, not limited to the research.

I was also fortunate to collaborate with Hajime Kawahara, whose attitude toward science always stimulated me in various ways. The discussion with him was simply enjoyable and insightful, and it definitely broadened my perspective a lot. Working with him, I also realized that collaboration with others from different backgrounds are essentially important in pursuing good researches. I would also like to thank Kento Masuda for his insight advices and comments. The most important thing I learned from him is the importance of being and behaving professional, which significantly has affected my view of researches. Furthermore, I want to show my gratitude to Kashiyama Kazumi for his continuous supports in various respects. I was always overwhelmed by his broad knowledge. Through the discussion with him, I unconsciously has got familiar with a lot of topics, which definitely expanded my possibility. He also listened to me and gave me appropriate advices when I was worried about the future.

I would also like to show my gratitude to my collaborators, Yoko Oya, Shiro Ikeda, Takeshi Nakazato, Siteng Fan, and Tomoyuki Tajiri for their professional knowledge, comments, and discussions. Woking with them, I directly learned the importance of discussing with people beyond one's field. In addition, I would like to thank Kenta Hotokezaka and Kento Masuda for their warm welcome during my stay at Princeton. The conversations with them helped me envision the future of my life. Furthermore, I would like to show my special thanks to Ryoma Murata for his encouragement and supports.

Additionally, I would like to show my gratitude to my thesis committee, Profs. Kipp Cannon, Ryohei Kawabe, Hideyuki Tagoshi, Toru Yamada, and Satoshi Yamamoto for their constructive comments and encouragements. Particularly, I am very grateful to Ryohei Kawabe for discussion on data analyses of interferometric observations in Chapter 4.

My gratitude definitely goes to all (ex-)members in Theoretical Astrophysical Group

(UTAP)/Research Center of Early Universe (RESCEU). I thank people in our exoplanet group, Kazuhiro Kanagawa, Yuta Nakagawa, Toshinori Hayashi, Shijie Wang, and Lu Yuting for discussions and sharing time in the weekly meeting. In addition, I would also like to show my special thanks to Sunmyon Chon, Shoya Kamiaka, Riouhei Nakatani, Ken Osato, and Taizo Okabe for giving me advices and sharing the precious time. I was also fortunate to enjoy the life within and beyond the research thanks to Yuta Nakagawa, Akinari Hamabada, Leo Tsukada, and Kojiro Kawana.

Finally, I deeply thank my family and friends for their continuous supports and encouragements in my life.

I am grateful to the Kepler team for making the revolutionary data publicly available. I thank the DSCOVR team for making the data publicly available. I also gratefully acknowledge the support by Japan Society for the Promotion of Science Research Fellowships for Young Scientists (14J07182) and by the Advanced Leading Graduate Course for Photon Science. This research made use of Astropy,[1] a community-developed core Python package for Astronomy (Astropy Collaboration et al., 2013, 2018). This thesis makes use of the following ALMA data: ADS/JAO.ALMA#2013.1.00220.S and #2015.1.00534.S. ALMA is a partnership of ESO (representing its member states), NSF (USA) and NINS (Japan), together with NRC (Canada), MOST and ASIAA (Taiwan), and KASI (Republic of Korea), in cooperation with the Republic of Chile.

---

[1] http://www.astropy.org

Bibliography

ALMA Partnership et al., 2015, The Astrophysical Journal Letters, 808, L3

Agol E., Jansen T., Lacy B., Robinson T. D., Meadows V., 2015, The Astrophysical Journal, 812, 5

Aizawa M., Uehara S., Masuda K., Kawahara H., Suto Y., 2017, The Astronomical Journal, 153, 193

Akinsanmi B., Oshagh M., Santos N. C., Barros S. C. C., 2018, Astronomy & Astrophysics, 609, A21

Akiyama K., et al., 2017a, The Astronomical Journal, 153, 159

Akiyama K., et al., 2017b, The Astrophysical Journal, 838, 1

Andrews S. M., Williams J. P., 2007, The Astrophysical Journal, 659, 705

Andrews S. M., Wilner D. J., Hughes A. M., Qi C., Dullemond C. P., 2010, The Astrophysical Journal, 723, 1241

Ansdell M., et al., 2016, The Astrophysical Journal, 828, 46

Ansdell M., et al., 2018, The Astrophysical Journal, 859, 21

Arnold L., Schneider J., 2004, Astronomy & Astrophysics, 420, 1153

Astropy Collaboration et al., 2013, Astronomy & Astrophysics, 558, A33

Astropy Collaboration et al., 2018, The Astronomical Journal, 156, 123

Bally J., O'Dell C. R., McCaughrean M. J., 2000, The Astronomical Journal, 119, 2919

Barenfeld S. A., Carpenter J. M., Ricci L., Isella A., 2016, The Astrophysical Journal, 827, 142

Barenfeld S. A., Carpenter J. M., Sargent A. I., Isella A., Ricci L., 2017, The Astrophysical Journal, 851, 85

Barnes J. W., Fortney J. J., 2004, The Astrophysical Journal, 616, 1193

Barnes J. W., Linscott E., Shporer A., 2011, The Astrophysical Journal Supplement Series, 197, 10

Bate M. R., Lodato G., Pringle J. E., 2010, Monthly Notices of the Royal Astronomical Society, 401, 1505

Beck A., Teboulle M., 2009a, SIAM journal on imaging sciences, 2, 183

Beck A., Teboulle M., 2009b, IEEE transactions on image processing, 18, 2419

Belloche A., 2013, in Hennebelle P., Charbonnel C., eds, EAS Publications Series Vol. 62, EAS Publications Series. pp 25–66 (`arXiv:1305.0627`), doi:10.1051/eas/1362002

Benedettini M., et al., 2015, Monthly Notices of the Royal Astronomical Society, 453, 2036

Bennett D. P., et al., 2014, The Astrophysical Journal, 785, 155

Briggs D. S., 1995, PhD thesis, New Mexico Institute of Mining and Technology

Brown T. M., Charbonneau D., Gilliland R. L., Noyes R. W., Burrows A., 2001, The Astrophysical Journal, 552, 699

Burkert A., Bodenheimer P., 2000, The Astrophysical Journal, 543, 822

Bussmann R. S., Wong T. W., Hedden A. S., Kulesa C. A., Walker C. K., 2007, The Astrophysical Journal Letters, 657, L33

Carpenter J. M., Mamajek E. E., Hillenbrand L. A., Meyer M. R., 2006, The Astrophysical Journal Letters, 651, L49

Carter J. A., Winn J. N., 2010, The Astrophysical Journal, 709, 1219

Carter J. A., et al., 2012, Science, 337, 556

Caselli P., Benson P. J., Myers P. C., Tafalla M., 2002, The Astrophysical Journal, 572, 238

Chandrasekhar S., Fermi E., 1953, The Astrophysical Journal, 118, 113

Chen C.-Y., Ostriker E. C., 2015, The Astrophysical Journal, 810, 126

Chen C.-Y., Ostriker E. C., 2018, The Astrophysical Journal, 865, 34

Chen X., Launhardt R., Henning T., 2007, The Astrophysical Journal, 669, 1058

Chen H. H.-H., et al., 2019, The Astrophysical Journal, 886, 119

Cieza L. A., et al., 2019, Monthly Notices of the Royal Astronomical Society, 482, 698

Comerón F., 2008, The Lupus Clouds. p. 295

Corsaro E., et al., 2017, Nature Astronomy, 1, 0064

Cossou C., Raymond S. N., Hersant F., Pierens A., 2014, Astronomy & Astrophysics, 569, A56

Cowan N. B., et al., 2009, The Astrophysical Journal, 700, 915

Cowan N. B., et al., 2011, The Astrophysical Journal, 731, 76

Cox E. G., et al., 2017, The Astrophysical Journal, 851, 83

Curran R. L., Chrysostomou A., 2007, Monthly Notices of the Royal Astronomical Society, 382, 699

Davies C. L., 2019, Monthly Notices of the Royal Astronomical Society, 484, 1926

Dawson R. I., Chiang E., 2014, Science, 346, 212

Dawson R. I., Johnson J. A., 2018, Annual Review of Astronomy and Astrophysics, 56, 175

Dawson R. I., Murray-Clay R. A., Johnson J. A., 2015, The Astrophysical Journal, 798, 66

Dib S., Hennebelle P., Pineda J. E., Csengeri T., Bontemps S., Audit E., Goodman A. A., 2010, The Astrophysical Journal, 723, 425

Duchêne G., Kraus A., 2013, Annual Review of Astronomy and Astrophysics, 51, 269

Dyudina U. A., Sackett P. D., Bayliss D. D. R., Seager S., Porco C. C., Throop H. B., Dones L., 2005, The Astrophysical Journal, 618, 973

Eisner J. A., et al., 2018, The Astrophysical Journal, 860, 77

Evans Neal J. I., et al., 2003, Publications of the Astronomical Society of the Pacific, 115, 965

Evans Neal J. I., et al., 2009, The Astrophysical Journal Supplement Series, 181, 321

Event Horizon Telescope Collaboration et al., 2019, The Astrophysical Journal Letters, 875, L4

Fan S., Li C., Li J.-Z., Bartlett S., Jiang J. H., Natraj V., Crisp D., Yung Y. L., 2019, The Astrophysical Journal Letters, 882, L1

Farr B., Farr W. M., Cowan N. B., Haggard H. M., Robinson T., 2018, The Astronomical Journal, 156, 146

Fleck R. C. J., Clark F. O., 1981, The Astrophysical Journal, 245, 898

Ford E. B., Seager S., Turner E. L., 2001, Nature, 412, 885

Foreman-Mackey D., Morton T. D., Hogg D. W., Agol E., Schölkopf B., 2016, The Astronomical Journal, 152, 206

Fujii Y., Kawahara H., 2012, The Astrophysical Journal, 755, 101

Fujii Y., Kawahara H., Suto Y., Taruya A., Fukuda S., Nakajima T., Turner E. L., 2010, The Astrophysical Journal, 715, 866

Fujii Y., Kawahara H., Suto Y., Fukuda S., Nakajima T., Livengood T. A., Turner E. L., 2011, The Astrophysical Journal, 738, 184

Fujii Y., Lustig-Yaeger J., Cowan N. B., 2017, The Astronomical Journal, 154, 189

Gaia Collaboration et al., 2018, Astronomy & Astrophysics, 616, A1

Gaudi B. S., et al., 2008, Science, 319, 927

Goodman A. A., Benson P. J., Fuller G. A., Myers P. C., 1993, The Astrophysical Journal, 406, 528

Górski K. M., Hivon E., Banday A. J., Wand elt B. D., Hansen F. K., Reinecke M., Bartelmann M., 2005, The Astrophysical Journal, 622, 759

Guilloteau S., Dutrey A., Piétu V., Boehler Y., 2011, Astronomy & Astrophysics, 529, A105

Hansen P. C., 2010, Discrete inverse problems: insight and algorithms. Siam

Hedman M. M., 2015, The Astrophysical Journal Letters, 801, L33

Heising M. Z., Marcy G. W., Schlichting H. E., 2015, The Astrophysical Journal, 814, 81

Heller R., Rodenbeck K., Bruno G., 2019, Astronomy & Astrophysics, 624, A95

Heyer M. H., Brunt C. M., 2004, The Astrophysical Journal Letters, 615, L45

Honma M., Akiyama K., Uemura M., Ikeda S., 2014, Publications of the Astronomical Society of Japan, 66, 95

Hsu D. C., Ford E. B., Ragozzine D., Ashby K., 2019, The Astronomical Journal, 158, 109

Huber D., et al., 2013, Science, 342, 331

Hughes J., Hartigan P., Krautter J., Kelemen J., 1994, The Astronomical Journal, 108, 1071

Hull C. L. H., et al., 2013, The Astrophysical Journal, 768, 159

Hull C. L. H., et al., 2017, The Astrophysical Journal Letters, 842, L9

Ikeda S., Tazaki F., Akiyama K., Hada K., Honma M., 2016, Publications of the Astronomical Society of Japan, 68, 45

Isella A., Carpenter J. M., Sargent A. I., 2009, The Astrophysical Journal, 701, 260

Jackson R. J., Jeffries R. D., 2010, Monthly Notices of the Royal Astronomical Society, 402, 1380

Jackson R. J., Deliyannis C. P., Jeffries R. D., 2018, Monthly Notices of the Royal Astronomical Society, 476, 3245

Jenkins J. M., et al., 2015, The Astronomical Journal, 150, 56

Jiang J. H., et al., 2018, The Astronomical Journal, 156, 26

Kamiaka S., Benomar O., Suto Y., 2018, Monthly Notices of the Royal Astronomical Society, 479, 391

Kamiaka S., Benomar O., Suto Y., Dai F., Masuda K., Winn J. N., 2019, The Astronomical Journal, 157, 137

Kawahara H., 2016, The Astrophysical Journal, 822, 112

Kawahara H., Fujii Y., 2010, The Astrophysical Journal, 720, 1333

Kawahara H., Fujii Y., 2011, The Astrophysical Journal Letters, 739, L62

Kawahara H., Masuda K., 2019, The Astronomical Journal, 157, 218

Kenyon S. J., Gómez M., Whitney B. A., 2008, Low Mass Star Formation in the Taurus-Auriga Clouds. p. 405

King R. R., Goodwin S. P., Parker R. J., Patience J., 2012, Monthly Notices of the Royal Astronomical Society, 427, 2636

Kipping D. M., 2009a, Monthly Notices of the Royal Astronomical Society, 392, 181

Kipping D. M., 2009b, Monthly Notices of the Royal Astronomical Society, 396, 1797

Kipping D. M., 2013, Monthly Notices of the Royal Astronomical Society, 435, 2152

Kipping D. M., Bakos G. Á., Buchhave L., Nesvorný D., Schmitt A., 2012, The Astrophysical Journal, 750, 115

Kitamura Y., Momose M., Yokogawa S., Kawabe R., Tamura M., Ida S., 2002, The Astrophysical Journal, 581, 357

Kolmogorov A., 1941a, Akademiia Nauk SSSR Doklady, 30, 301

Kolmogorov A. N., 1941b, Akademiia Nauk SSSR Doklady, 32, 16

Kong S., Arce H. G., Maureira M. J., Caselli P., Tan J. C., Fontani F., 2019, The Astrophysical Journal, 874, 104

Kovacs G., 2018, Astronomy & Astrophysics, 612, L2

Kreidberg L., Luger R., Bedell M., 2019, The Astrophysical Journal Letters, 877, L15

Krumholz M. R., 2014, Physics Reports, 539, 49

Kuffmeier M., Haugbølle T., Nordlund Å., 2017, The Astrophysical Journal, 846, 7

Kuiper N. H., 1960, Nederl. Akad. Wetensch. Proc. Ser. A, 63, 38

Kuramochi K., Akiyama K., Ikeda S., Tazaki F., Fish V. L., Pu H.-Y., Asada K., Honma M., 2018, The Astrophysical Journal, 858, 56

Kuznetsova A., Hartmann L., Heitsch F., 2019, The Astrophysical Journal, 876, 33

Lada C. J., Lada E. A., 2003, Annual Review of Astronomy and Astrophysics, 41, 57

Larson R. B., 1981, Monthly Notices of the Royal Astronomical Society, 194, 809

Lecavelier des Etangs A., et al., 2017, Astronomy & Astrophysics, 603, A115

Lee E. J., Chiang E., 2016, The Astrophysical Journal, 817, 90

Lee E. J., Chiang E., Ormel C. W., 2014, The Astrophysical Journal, 797, 95

Li P. S., Norman M. L., Mac Low M.-M., Heitsch F., 2004, The Astrophysical Journal, 605, 800

Lissauer J. J., et al., 2011, Nature, 470, 53

Luhman K. L., Mamajek E. E., 2012, The Astrophysical Journal, 758, 31

Lustig-Yaeger J., Robinson T., Arney G., 2019, The Journal of Open Source Software, 4, 1387

Macintosh B., et al., 2014, Proceedings of the National Academy of Science, 111, 12661

Mandel K., Agol E., 2002, The Astrophysical Journal Letters, 580, L171

Mardia K. V., Jupp P. E., 2009, Directional statistics. John Wiley & Sons

Markwardt C. B., 2009, Non-linear Least-squares Fitting in IDL with MPFIT. p. 251

Masuda K., 2014, The Astrophysical Journal, 783, 53

Masuda K., 2015, The Astrophysical Journal, 805, 28

Mayor M., Queloz D., 1995, Nature, 378, 355

McMullin J. P., Waters B., Schiebel D., Young W., Golap K., 2007, CASA Architecture and Applications. p. 127

Ménard F., Duchêne G., 2004, Astronomy & Astrophysics, 425, 973

Merín B., et al., 2008, The Astrophysical Journal Supplement Series, 177, 551

Mocz P., Burkhart B., Hernquist L., McKee C. F., Springel V., 2017, The Astrophysical Journal, 838, 40

Mortier A., Oliveira I., van Dishoeck E. F., 2011, Monthly Notices of the Royal Astronomical Society, 418, 1194

Mosser B., Gehan C., Belkacem K., Samadi R., Michel E., Goupil M. J., 2018, Astronomy & Astrophysics, 618, A109

Mróz P., et al., 2017, Nature, 548, 183

Mullally F., Thompson S. E., Coughlin J. L., Burke C. J., Rowe J. F., 2018, The Astronomical Journal, 155, 210

Nakajima Y., Tamura M., Oasa Y., Nakajima T., 2000, The Astronomical Journal, 119, 873

Nakazato T., Ikeda S., Akiyama K., ; Kosugi G., Yamaguchi M., Honma M., 2019, Astronomical Data Analysis Software and Systems XXVIII, 523, 143

Niemczura E., et al., 2015, Monthly Notices of the Royal Astronomical Society, 450, 2764

Oakley P. H. H., Cash W., 2009, The Astrophysical Journal, 700, 1428

Ohashi N., Hayashi M., Ho P. T. P., Momose M., Tamura M., Hirano N., Sargent A. I., 1997, The Astrophysical Journal, 488, 317

Ohta Y., Taruya A., Suto Y., 2005, The Astrophysical Journal, 622, 1118

Ohta Y., Taruya A., Suto Y., 2009, The Astrophysical Journal, 690, 1

Ortiz-León G. N., et al., 2017, The Astrophysical Journal, 834, 141

Osborn H. P., et al., 2016, Monthly Notices of the Royal Astronomical Society, 457, 2273

Pallé E., Ford E. B., Seager S., Montañés-Rodríguez P., Vazquez M., 2008, The Astrophysical Journal, 676, 1319

Paltani S., 2004, Astronomy & Astrophysics, 420, 789

Parviainen H., 2015, Monthly Notices of the Royal Astronomical Society, 450, 3233

Pecaut M. J., Mamajek E. E., Bubar E. J., 2012, The Astrophysical Journal, 746, 154

Pérez L. M., et al., 2016, Science, 353, 1519

Pérez L. M., et al., 2018, The Astrophysical Journal Letters, 869, L50

Perryman M., Hartman J., Bakos G. Á., Lindegren L., 2014, The Astrophysical Journal, 797, 14

Pineda J. E., Zhao B., Schmiedeke A., Segura-Cox D. M., Caselli P., Myers P. C., Tobin J. J., Dunham M., 2019, The Astrophysical Journal, 882, 103

Piro A. L., Vissapragada S., 2019, arXiv e-prints, p. arXiv:1911.09673

Pirogov L., Zinchenko I., Caselli P., Johansson L. E. B., Myers P. C., 2003, Astronomy & Astrophysics, 405, 639

Planck Collaboration et al., 2016a, Astronomy & Astrophysics, 586, A138

Planck Collaboration et al., 2016b, Astronomy & Astrophysics, 596, A109

Preibisch T., Brown A. G. A., Bridges T., Guenther E., Zinnecker H., 2002, The Astronomical Journal, 124, 404

Protassov R., van Dyk D. A., Connors A., Kashyap V. L., Siemiginowska A., 2002, The Astrophysical Journal, 571, 545

Rafikov R. R., 2017, The Astrophysical Journal, 837, 163

Rappaport S., et al., 2012, The Astrophysical Journal, 752, 1

Raymond S. N., Cossou C., 2014, Monthly Notices of the Royal Astronomical Society, 440, L11

Reggiani M., Robberto M., Da Rio N., Meyer M. R., Soderblom D. R., Ricci L., 2011, Astronomy & Astrophysics, 534, A83

Rey-Raposo R., Read J. I., 2018, Monthly Notices of the Royal Astronomical Society, 481, L16

Robinson T. D., Meadows V. S., Crisp D., 2010, The Astrophysical Journal Letters, 721, L67

Robinson T. D., Stapelfeldt K. R., Marley M. S., 2016, Publications of the Astronomical Society of the Pacific, 128, 025003

Sakai N., Hanawa T., Zhang Y., Higuchi A. E., Ohashi S., Oya Y., Yamamoto S., 2019, Nature, 565, 206

Sanchis-Ojeda R., Winn J. N., 2011, The Astrophysical Journal, 743, 61

Sanchis-Ojeda R., et al., 2013, The Astrophysical Journal, 775, 54

Santerne A., et al., 2019, arXiv e-prints, p. arXiv:1911.07355

Santos N. C., et al., 2015, Astronomy & Astrophysics, 583, A50

Schlichting H. E., Chang P., 2011, The Astrophysical Journal, 734, 117

Schmitt J. R., et al., 2014, The Astrophysical Journal, 795, 167

Schmitt J. R., Jenkins J. M., Fischer D. A., 2017, The Astronomical Journal, 153, 180

Schwartz J. C., Sekowski C., Haggard H. M., Pallé E., Cowan N. B., 2016, Monthly Notices of the Royal Astronomical Society, 457, 926

Simbulan C., Tamayo D., Petrovich C., Rein H., Murray N., 2017, Monthly Notices of the Royal Astronomical Society, 469, 3337

Simon M., Dutrey A., Guilloteau S., 2000, The Astrophysical Journal, 545, 1034

Stephens M., 1965, Biometrika, 52, 309

Stephens I. W., et al., 2017, The Astrophysical Journal, 846, 16

Sumi T., et al., 2011, Nature, 473, 349

Sumi T., et al., 2016, The Astrophysical Journal, 825, 112

Suto Y., Kamiaka S., Benomar O., 2019, The Astronomical Journal, 157, 172

Suzuki D., et al., 2016, The Astrophysical Journal, 833, 145

Targon C. G., Rodrigues C. V., Cerqueira A. H., Hickel G. R., 2011, The Astrophysical Journal, 743, 54

Tatematsu K., Kandori R., Umemoto T., Sekimoto Y., 2008, Publications of the Astronomical Society of Japan, 60, 407

Tatematsu K., Ohashi S., Sanhueza P., Nguyen Luong Q., Umemoto T., Mizuno N., 2016, Publications of the Astronomical Society of Japan, 68, 24

Tazzari M., et al., 2017, Astronomy & Astrophysics, 606, A88

Teachey A., Kipping D. M., 2018, Science Advances, 4, eaav1784

Teachey A., Kipping D. M., Schmitt A. R., 2018, The Astronomical Journal, 155, 36

Thompson S. E., et al., 2018, The Astrophysical Journal Supplement Series, 235, 38

Tobin J. J., et al., 2011, The Astrophysical Journal, 740, 45

Uehara S., Kawahara H., Masuda K., Yamada S., Aizawa M., 2016, The Astrophysical Journal, 822, 2

Walker G. A. H., et al., 2007, The Astrophysical Journal, 659, 1611

Wang J., et al., 2015, The Astrophysical Journal, 815, 127

Weiss L. M., et al., 2013, The Astrophysical Journal, 768, 14

Wilking B. A., Gagné M., Allen L. E., 2008, Star Formation in the ρ Ophiuchi Molecular Cloud. p. 351

Williams J. P., Cieza L. A., 2011, Annual Review of Astronomy and Astrophysics, 49, 67

Winn J. N., Fabrycky D. C., 2015, Annual Review of Astronomy and Astrophysics, 53, 409

Wittenmyer R. A., Butler R. P., Wang L., Bergmann C., Salter G. S., Tinney C. G., Johnson J. A., 2016, Monthly Notices of the Royal Astronomical Society, 455, 1398

Wolszczan A., Frail D. A., 1992, Nature, 355, 145

Yen H.-W., Koch P. M., Manara C. F., Miotello A., Testi L., 2018, Astronomy & Astrophysics, 616, A100

Zhu W., Petrovich C., Wu Y., Dong S., Xie J., 2018, The Astrophysical Journal, 860, 101

Zuluaga J. I., Kipping D. M., Sucerquia M., Alvarado J. A., 2015, The Astrophysical Journal Letters, 803, L14